



저작자표시-비영리-변경금지 2.0 대한민국

이용자는 아래의 조건을 따르는 경우에 한하여 자유롭게

- 이 저작물을 복제, 배포, 전송, 전시, 공연 및 방송할 수 있습니다.

다음과 같은 조건을 따라야 합니다:



저작자표시. 귀하는 원저작자를 표시하여야 합니다.



비영리. 귀하는 이 저작물을 영리 목적으로 이용할 수 없습니다.



변경금지. 귀하는 이 저작물을 개작, 변형 또는 가공할 수 없습니다.

- 귀하는, 이 저작물의 재이용이나 배포의 경우, 이 저작물에 적용된 이용허락조건을 명확하게 나타내어야 합니다.
- 저작권자로부터 별도의 허가를 받으면 이러한 조건들은 적용되지 않습니다.

저작권법에 따른 이용자의 권리는 위의 내용에 의하여 영향을 받지 않습니다.

이것은 [이용허락규약\(Legal Code\)](#)을 이해하기 쉽게 요약한 것입니다.

[Disclaimer](#)

공학박사학위논문

**분산형 통신 및 구동부족 로봇시스템
을 위한 분할기법 기반의 반자율
원격제어 프레임워크 개발**

**Decomposition-based Semi-Autonomous Teleoperation
Frameworks for Robotic Systems with Distributed
Communication and Under-actuation**

2018 년 2 월

서울대학교 대학원

기계항공공학부

하 창 수

**분산형 통신 및 구동부족 로봇시스템
을 위한 분할기법 기반의 반자율
원격제어 프레임워크 개발**

**Decomposition-based Semi-Autonomous Teleoperation
Frameworks for Robotic Systems with Distributed
Communication and Under-actuation**

지도교수 이 동 준

이 논문을 공학박사 학위논문으로 제출함

2017 년 10 월

서울대학교 대학원

기계항공공학부

하 창 수

하창수의 공학박사 학위논문을 인준함

2017 년 12 월

위 원 장 : 박 종 우

부위원장 : 이 동 준

위 원 : 김 경 수

위 원 : 신 호 철

위 원 : 조 규 진

Abstract

Decomposition-Based Semi-Autonomous Teleoperation Frameworks for Robotic Systems with Distributed Communication and Under-actuation

by Changsu Ha

Department of Aerospace and Mechanical Engineering

College of Engineering

Seoul National University

The framework of stable bilateral teleoperation has been well established during decades. However, the standard bilateral teleoperation framework could be a baseline for a successful telerobotics but not sufficient for real-application because they usually concentrate on only the bilateral stability. The least considered in the previous research is how to apply a complex robot systems such as multiple mobile robots or a large degree of freedom mobile manipulators for real applications. The main challenges of teleoperation of complex robotic systems in real-world are to achieve two different control objectives (i.e., follow the human command and the coordination/stabilization of the internal movement) of the slave robots simultaneously, while providing intuitive information about the complicated features of the system.

In this thesis, we develop decomposition-based semi-autonomous teleoperation framework for robotic systems which have distributed communication and under-actuation property, consisting of three steps: 1) decomposition step, where the human command is defined, and the robotic system is split into the command tracking space and its orthogonal complement (i.e., internal motion); 2) control design of the slave robot, in which we design the slave controller for human command tracking and stabilization/coordination of internal motion space; and 3) feedback interface design, through which we propose a multi-modal feedback interface (for example, visual and haptic) designed with the consideration of the task and the characteristics of the system.

Among numerous types of robots, in this thesis, we focus on two types of robotic systems: 1) multiple nonholonomic wheeled mobile robots (WMRs) with distributed

communication requirement and 2) manipulator-stage over vertical flexible beam which is under-actuated system. The proposed framework is applied to both case step by step and perform experiments and human subject study to verify/demonstrate the proposed framework for both cases.

For distributed WMRs, we consider the scenario that a single user remotely operates a platoon of nonholonomic WMRs that distributively communicate each other in unknown environment. For this, in decomposition step, we utilize nonholonomic passive decomposition to split the platoon kinematics into that of the formation-keeping aspect and the collective tele-driving aspect. Next, in control design step, we design the controls for these two aspects individually and distribute them into each WMR while fully incorporating their nonholonomic constraint and distribution requirement. Finally, in the step of feedback interface design, we also propose a novel predictive display, which, by providing the user with the estimated current and predicted future pose informations of the platoon and future possibility of collision while fully incorporating the uncertainty inherent to the distribution, can significantly enhance the tele-driving performance and easiness of the platoon.

The second part is the manipulator-stage over vertical flexible beam which is under-actuated system. Here, the human command defines the desired motion of the end-effector (or the manipulator), and the vibration of the beam should be subdued at the same time. Thus, at the first step, we utilize the passive decomposition to split the dynamics into manipulator motion space and its orthogonal complement, in which we design the control for the suppression of the vibration. For human command tracking, we design the passivity-based control, and, for the suppression of the vibration, we propose two controls: LQR-based control and nonlinear control based on Lyapunov function analysis. Finally, visuo-haptic feedback interface is preliminarily designed for successful peg-in-hole tasks.

Keywords: Semi-autonomous teleoperation, distributed systems, underactuated systems, decomposition-based control

Contents

1	Introduction	1
1.1	Background and Contribution	1
1.2	Related Works	4
1.2.1	Related Works on Distributed Systems	5
1.2.2	Related Works on Manipulator-Stage System	6
1.3	Outline	6
2	Preliminary	7
2.1	Passive Decomposition	7
2.1.1	Basic Notations and Properties of Standard Passive Decomposition	7
2.1.2	Nonholonomic Passive Decomposition	9
3	Semi-Autonomous Teleoperation of Nonholonomic Wheeled Mobile Robots with Distributed Communication	11
3.1	Distributed Control Design	11
3.1.1	Nonholonomic Passive Decomposition	11
3.1.2	Control Design and Distribution	19
3.2	Distributed Pose Estimation	25
3.2.1	EKF Pose Estimation of Leader WMR	25
3.2.2	EKF Pose Estimation of Follower WMRs	28
3.3	Predictive Display for Distributed Robots Teleoperation	29
3.3.1	Estimation Propagation	31

3.3.2	Prediction Propagation	34
3.4	Experiments	38
3.4.1	Test Setup	38
3.4.2	Performance Experiment	39
3.4.3	Teleoperation Experiment with Predictive Display	40
3.4.4	Human Subject Study	44
4	Semi-Autonomous Teleoperatoin of Stage-Manipulator System on Flexible Vertical Beam	49
4.1	System Modeling	49
4.1.1	System Description	49
4.1.2	Assumed Mode Shapes	51
4.1.3	Exact Solution under Given Boundary Conditions	51
4.1.4	Euler-Lagrangian Equation	61
4.2	LQR-based Control Design	62
4.2.1	Passive Decomposition	63
4.2.2	Vibration Suppression Control Design	64
4.2.3	Joint Tracking Control Design	66
4.3	Lyapunov-based Control Design	68
4.3.1	Twice Passive Decomposition for Input Coupling	69
4.3.2	Interconnected System Description	70
4.3.3	Passivity-based Manipulator Motion Control	74
4.3.4	Dissipative Control for Vibration Suppression	74
4.4	Experiments	78
4.4.1	Test Setup	78
4.4.2	Joint Tracking and Vibration Suppression Experiment	81
4.4.3	Comparison Experiment between the LQR and the Nonlinear Control	82
5	Conclusion	83
5.1	Summary	83

5.2	Future Works	83
A	Appendix	85
A.1	Internal Wrench Representation	85

List of Figures

1-1	Overview of a telerobotic system consisting of master, slave, and communication channel	2
3-1	Platoon of distributed nonholonomic WMRs: one “smart” leader WMR (with LiDAR, IMU and FPV camera) and three “simple” follower WMRs (with monocular camera and IMU) (top). Peer-to-peer communication architecture among the WMRs and the information flowing through it (bottom).	12
3-2	Platoon of distributed WMRs navigating in a large-hall with array of plant pots (top); and predictive display view with LiDAR-SLAM map, current and future pose estimates of the WMRs with uncertainty (i.e., size ellipsoids and direction cone) (bottom). Possible collision of a WMR will be indicated by white circular shade, if its future pose estimate collides with non-traversable scanned regions of the SLAM map (see bottom middle two pictures of Fig. 3-11.	13
3-3	Geometry of platoon of the distributed nonholonomic WMRs, when they collectively behave as the n -trailer system under the virtual constraint $h(q_{j,j+1}) = 0$, that is, each following WMR maintains the distance L_j from, and also faces toward the axle-center of, their respective fore-running WMR.	16

3-4	Simulation result of the platoon of 30 WMRs making a triangular formation under the distributed control (3.12)-(3.13) and the modified formation map (3.18) with the camera-heading offset angle α_j to slant the two branches of the formation from each other.	22
3-5	Predictive display consists of the two propagation stages: 1) estimation propagation stage to estimate the pose of each WMR at the current time from its reception with the transmission delay; and 2) prediction propagation stage to predict the future course of platoon motion over prediction time horizon via forward propagation.	32
3-6	Predictive display with estimated current and predicted future poses of WMRs. Uncertainty of pose estimate is denoted by enlarged size of the WMR and the heading angle cone, with their nominal size and center angle determined by the means: 1) uncertainty is the largest for the last WMR (left); and 2) uncertainty still substantial even with fairly precise sensors if the WMRs are many (right).	36
3-7	Circular and s-shape trajectories of the three WMRs during the performance experiments: dotted lines are the ground truth position measured by MOCAP and solid lines the estimated position computed by the distributed estimation of Sec. 3.2.	40
3-8	Inter-WMR coordination error $ h_{j,j+1} $ among the three WMRs during the performance experiments with the circular and s-shape trajectories.	41
3-9	The environment map for the teleoperation experiment and human subject study test: yellow boxes indicate four markers that the user should check; the green boxes are obstacles, with the dotted green box a short obstacle that cannot be detected by the LiDAR but should be noticed by the FPV camera. The blue dotted path presents the trajectory of the leader WMR of a successful trial.	42
3-10	Teleoperation master interface consisting of predictive display with LiDAR-SLAM map and FPV camera video-feed, and haptic device (used only as positioning device without haptic feedback).	43

3-11	Snapshots of the office-corridor teleoperation experiment: (Top row) External camera third person view of the environment with scattered box obstacles and the table in the middle of the office room; (Bottom row) Predictive display with LiDAR-SLAM map, showing the current (solid) and future (opaque) pose estimate of the WMRs and possible collision (white circular shade) along with the FPV camera video-feed.	44
3-12	Number of successful/failed trials and average completion time across the subjects of each Task for the experimental group (eight subjects) and control group (five subjects).	45
3-13	NASA TLX questionnaire result and the user disfavor (i.e., 1- preference) rating with and without the predictive display for the human subject study experiments.	47
4-1	Test-bed model of slave robot of telerobotics project.	50
4-2	Lumped masses boundary conditions at the end of the boom	52
4-3	Solutions (β_1 , β_2 , and β_3) of the determinant \mathcal{D} with different parameters: the first determinant \mathcal{D}_1 is calculated very large total inertia I_0 which is 10^6 times of real inertia. In this case, the determinant has the first local minimum around the origin so that the first mode is also closed to the zero.	58
4-4	Three mode shapes	60
4-5	Experiment setup consists of three DOF manipulator, one DOF linear stage, and the flexible beam. Each actuator is torque-controllable	78
4-6	The snapshots of the joint tracking experiment: (a) the manipulator starts with the large initial error; (b) the manipulator converges to the desired configuration; (c) the system is stabilized due to the vibration suppression control or the structural damping (in the case of without the vibration suppression control); (d) the external disturbance (human force) is applied; and (e) again, the system is stabilized.	79

4-7	The linear stage and the deflection of the flexible beam: the beam deflection is measured at the tip of the beam. At 15 sec. and 30 sec., we push the system to show the performance of the suppression control against the unmodeled external disturbance.	79
4-8	Performance comparison between the LQR controller in Sec. 4.2 and nonlinear control in Sec. 4.3 against external disturbance	80
4-9	Snapshots of the comparison experiment: the upper row is the experiment with the LQR control where the large deflection due to the external disturbance cause the the system instability. On the other hands, in the second row, the deflection of the system with nonlinear control is still bounded.	81

Chapter 1

Introduction

1.1 Background and Contribution

Telerobotics has enjoyed enriching results for decades because the area is one of the earliest and most important fields of research in robotics. It is still inevitable to use a remote control (i.e., teleoperation) to use robotic systems in dangerous environments or where people can not remain despite recent significant advances in systems, algorithms, and techniques for autonomous robots. In other words, it is still challenging, and often impossible, to perform the task in a complete autonomous fashion, particularly when the task takes places in unstructured, uncertain and dynamic environments. For such real-world tasks in unstructured/dynamic environments, teleoperation is often the only viable solution, where human can solve many crucial tasks (e.g., remote manipulation even with fairly limited information, navigation/operation in unstructured/unmapped environment with dynamic obstacles, etc.), which are typically very difficult or even impossible to be addressed by fully-autonomous robots.

Many researchers in telerobotics attack two main goals in control theoretic view: stability and transparency [1,2]. Particularly, one of major issue in telerobotics have been the the interaction stability problem of bilateral teleoperation with or without communication imperfectness (e.g., [3–10]). Although the bilateral stability problem is fundamental for the long-distance application between the master and the slave, such as space-robotics, the solution for the stability problem is not sufficient for tasks

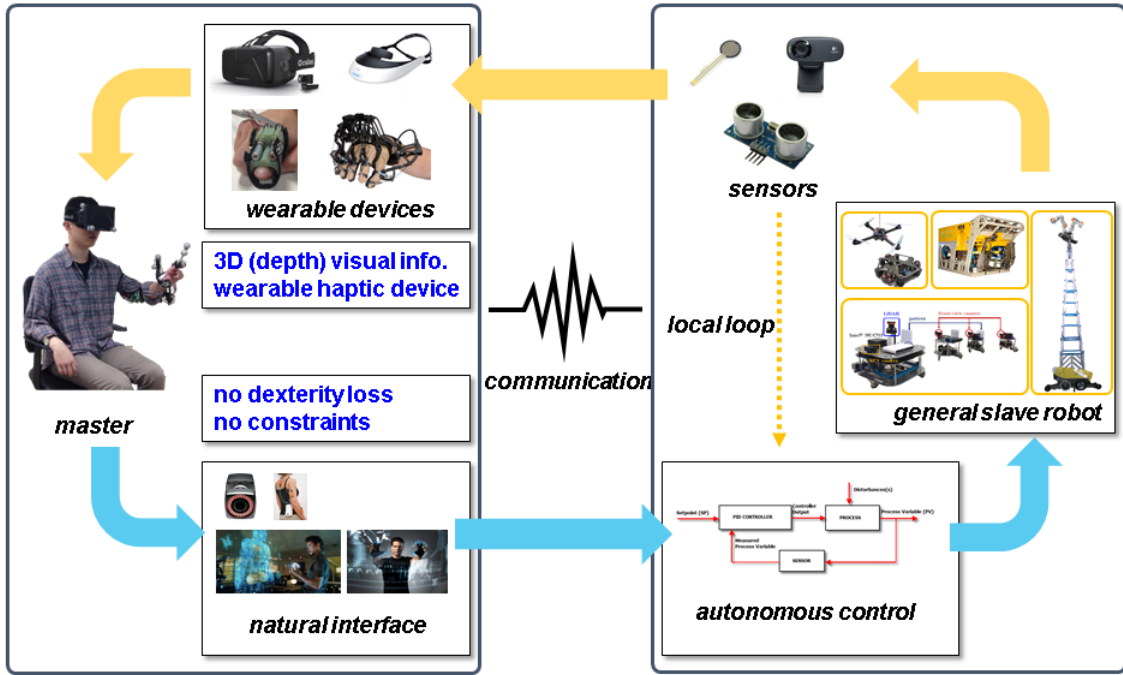


Figure 1-1: Overview of a telerobotic system consisting of master, slave, and communication channel

in the real world for which the slave robotics should have more functionalities or degree-of-freedom (DoF). Since complex robotic systems have many DoFs and complicated kinematics/dynamics, standard teleoperation framework in which the master and the slave are simple cannot be applicable for these systems.

For complex robotic systems, we believe that several areas, from slave control design to feedback design, should be seamlessly incorporated into the adoption of advanced telerobotic systems for such complex slave robots in real-world applications. In other words, since it is difficult for a user to manipulate each DoF of the system, the user must be able to operate the slave robots at a high level and the human should intuitively recognize rich information including the state of the environment and the system such as singularity or joint limits. Therefore, the decomposition of the space of the slave robot is necessary for the separation between the human command space and the space of the remaining DoFs (i.e., internal movement). In addition, another important factors for effortless human operation is the rich feedback information provided in a way that does not confuse the user.

The main contribution of this thesis is to develop a novel framework of decomposition-based semi-autonomous teleoperation for robotic systems with distributed communication and under-actuation. The framework consists of three steps: 1) decomposition step, where the human command is defined, and the robotic system is split into the command tracking space and its orthogonal complement (i.e., internal motion); 2) control design of the slave robot, in which we design the slave controller for human command tracking and stabilization/coordination of internal motion space; and 3) feedback interface design, through which we propose a multi-modal feedback interface (for example, visual and haptic) designed with the consideration of the task and the characteristics of the system.

We apply this framework to the distributed WMRs and manipulator-stage over vertical flexible beam due to the following usefulness of these systems due to their usefulness and potential for real applications. For instance, multiple mobile robots are suitable for exploration and reconnaissance in an unknown environment. In particular, distributed robotics have advantages for many applications such as transport of materials and goods; 2) search, exploration and sensor network; and 3) collective manipulation and assembly. In addition, the manipulator with an extendable structure or an aerial manipulator system is ideal for working in a high place. However, aerial manipulator systems are hard to perform a task which needs a large torque capability in complicated environment, for example, nuclear power plant. Thus, the manipulator-stage on the flexible vertical beam could be a promising solution for the tasks which needs large torque task in a high place, such as nuclear power plant or warehouse.

In the decomposition step, although we deploy the previous results [11], *passive decomposition*, this technique has not been applied to the distributed and underactuated system. Furthermore, by applying the passive decomposition to two systems, we can greatly simplify the uncertainty propagation computation for the predictive display in Sec. 3.3 and reveal the dynamic relation between the stage and the vibrational motion, which facilitates the control design. In control step, we design the two explicitly distinct controls for two different control objectives, i.e., human com-

mand tracking and stabilize/coordinate the internal motion. In particular, in Chap. 3, we design the distributed and cascade form of the controls that guarantees the desired internal motion and command tracking of the collective motion of the platoon of the WMRs. In Chap. 4, we design the vibration suppression control whose closed loop is exponentially stable so that it is robust to the external disturbance, for example, dynamic effect of the movement of the manipulator. Finally, we propose a novel predictive display in Sec. 3.3 which, by providing the user with the estimated current and predicted future pose informations of the platoon and future possibility of collision while fully incorporating the uncertainty inherent to the distribution, can significantly enhance the tele-driving performance and easiness of the platoon. We also perform a peg-in-hole experiment with the manipulator-stage system by using properly designed haptic feedback. We believe that the proposed seamless framework for the robotic systems with distributed communication and underactuation can push the boundary of the telerobotic research field.

1.2 Related Works

As far as we know, research on systematic framework of teleoperation of complex robotic systems has not studied much, compared to the results of the stability problem. A semi-autonomous teleoperation for multiple mobile robots is studied in [12], in which only the control aspect is studied. Another research on semi-autonomous teleoperation are [13–15] However, these results do not clearly distinguish the system in two subspaces, so a user teleoperates one or some of the agents directly and the other agents simply follow the ordered agents. These frameworks are applicable for multi mobile robot systems but not clear for a single large-DoFs system such as mobile manipulator or manipulator-stage with extendible structure as shown in Chap. 4. The authors also assume availability of some reasonably good trajectory tracking control law for each mobile robot, which then allow to abstract the first order system (directly driven by the input). This framework is not applicable distributed/nonholonomic systems as presented in Chap. 3 and underactuated systems as presented in

Chap. 4. Furthermore, the results do not systematically consider the feedback interface but typically assume haptic force feedback with the assumption that global view is possible. In such case, the feedback is not so crucial because visual information is rich enough for the user to recognize both the robot status and the environment. However, in real applications, the global scene is usually not available so that other forms of feedback are necessary for successful teleoperation.

Meanwhile, multi-modal interface is studied in [16], which has been recently evolved into the teleoperation system of the humanoid robot [17]. Another related multi-modal teleoperation systems were proposed in [18, 19]. However, all these studies are limited to anthropomorphic slave robots (exact mapping of the human motion into the slave robot’s motion) and the issue of control aspect is not considered therein. Furthermore, the results do not consider the abstracted command scenario so that seem not applicable for general and complex robotic systems.

1.2.1 Related Works on Distributed Systems

Numerous techniques have been proposed for the formation control of multiple distributed nonholonomic WMRs, some experimentally demonstrated with onboard sensing and estimation (e.g., [20–23]). On the other hand, many results have been reported for the teleoperation of multiple mobile robots (e.g., centralized [12, 24, 25], distributed [14, 15]) and also for the teleoperation with predictive display (e.g., [26–29]). Yet, to our knowledge, there has been no result so far, which systematically utilizes the predictive display for the teleoperation of multiple distributed mobile robots to allow the user to better handle with the complex kinematics of their collective while fully taking into account the uncertainty inherently arising from their sensing, computation and communication being distributed. In fact, we believe our framework proposed here is the very first predictive display teleoperation result of distributed mobile robots with the distribution-induced uncertainty fully incorporated and its efficacy fully manifested by human subject study. The holistic framework for the distributed robot teleoperation, encompassing the behavior decomposition, the control design distribution, the distributed estimation and the predictive display, to our knowledge, is also

proposed in this thesis for the first time.

1.2.2 Related Works on Manipulator-Stage System

As for the passive decomposition, authors in [30, 31] use the passive decomposition for the fully-actuated and rigid-body systems in, yet, none of them has been demonstrated for underactuated and flexible systems. Many studies have dealt with the control problem of manipulators on flexible supports from mid of 90's. Macro/micro-manipulators can be considered as one of these types of problems due to the flexibility of the macro manipulator [32–34]. Another researches consider the compliant base problem in [35–37]. However, most of the above use the mixed control method that are put the two different control inputs into one control channel by assuming that the time scale of vibration and tracking is different. To avoid this one-channel control approach, redundant systems are utilized in [38]. In [38], the vibration suppression is first designed, and null-space motion is used for tracking control. However, this control is also capable of either tracking or vibration suppression. Also, whereas we model the flexibility as rigorous as possible, in most cases the flexible base is simplified to model as a single DOF, such as a spring and damper system.

1.3 Outline

The outline of this thesis is as follows. Chapter 1, provides an introduction and statement of the contributions with review of some related works. In chapter 2, we briefly review the passive decomposition which plays an important role in this thesis. Chapter 3 is devoted to the semi-autonomous teleoperation of distributed nonholonomic WMRs including distributed control design based on nonholonomic passive decomposition, distributed estimation, and the design of the predictive display. In chapter 4, we present the framework applied to the manipulator-stage on vertical flexible beam from the derivation of the dynamics to the control and interface design. In chapter 5, we make concluding remarks and state possible directions of future research.

Chapter 2

Preliminary

2.1 Passive Decomposition

Passive decomposition plays a crucial role in this thesis by dividing the original systems into subsystems according to the given control objectives. The following subsection is brief review of [11] and [39].

2.1.1 Basic Notations and Properties of Standard Passive Decomposition

Let us start with the dynamics of mechanical systems

$$M(q)\ddot{q} + C(q, \dot{q})\dot{q} + g(q) = \tau$$

where $q, \dot{q}, \tau \in \mathfrak{R}^n$ are the configuration, velocity, and control, $M, C \in \mathfrak{R}^{n \times n}$ are the inertia and Coriolis matrices with $\dot{M} - 2C$ being skew symmetric. Suppose that the motion coordination or formation requirements can be represented by the mapped point of a (holonomic) map

$$h : \mathfrak{R}^n \rightarrow \mathfrak{R}^n, \quad m \leq n$$

Following the latter application of h , we call this map h *coordination map* and its range space $\mathcal{N} \approx \mathfrak{R}^m$ *formation manifold*. We further assume that this formation map h is a smooth submersion (i.e., its Jacobian is full rank). Then, the level set of h is defined by

$$\mathcal{H}_{h(q)} := \{q \in \mathfrak{R}^n | h(q) = c, c \in \mathfrak{R}^m\} \quad (8) \quad (2.1)$$

Then, we can split the tangent space of the system s.t.,

$$\begin{aligned} \Delta^\top &:= \{\dot{q} \in \mathfrak{R}^n | \mathcal{L}_{\dot{q}}h(q) = \mathcal{L}_{\dot{q}}q_f = 0\} = \text{null}(\partial q_f / \partial q) \\ \Delta^\perp &:= \{v \in \mathfrak{R}^n | v^T M(q) \xi = 0, \forall \xi \in \Delta^\top\} \end{aligned}$$

where $\mathcal{L}_{\dot{q}}$ is the Lie derivative of $h(q)$ along \dot{q} . This then implies that the tangent space of the system splits s.t.,

$$T_q \mathcal{M} = \Delta^\top \oplus \Delta^\perp$$

where \oplus is the direct sum, 1) Δ^\top is called tangent distribution (i.e., parallel to the level set of $h(q)$), and 2) Δ^\perp is called normal distribution (i.e., orthogonal complement of Δ^\top w.r.t. the inertia matrix $M(q)$). We call the dynamics projected on the tangent distribution *locked system* and the system on Δ^\perp *shape system*.

Then, we can write \dot{q} by

$$\dot{q} = \underbrace{\begin{bmatrix} \Delta_\top & \Delta_\perp \end{bmatrix}}_{:=\Delta(q)} \underbrace{\begin{bmatrix} v_L \\ v_E \end{bmatrix}}_{:=\nu}$$

where the matrices $\Delta_\top \in \mathfrak{R}^{n \times (n-m)}$ and $\Delta_\perp \in \mathfrak{R}^{n \times m}$ identify their respective spaces.

Using $\Delta_\top^T M \Delta_\perp = 0$, $\dot{q} = \Delta \nu$, and $\ddot{q} = \Delta \dot{\nu} + \dot{\Delta} \nu$, we can then decompose the

original dynamics into

$$\begin{bmatrix} M_L & 0 \\ 0 & M_E \end{bmatrix} \begin{bmatrix} \dot{v}_L \\ \dot{v}_E \end{bmatrix} + \begin{bmatrix} C_L & C_{LE} \\ C_{LE} & C_E \end{bmatrix} \begin{bmatrix} v_L \\ v_E \end{bmatrix} + \begin{bmatrix} g_L \\ g_E \end{bmatrix} = \begin{bmatrix} \tau_L \\ \tau_E \end{bmatrix} \quad (2.2)$$

where $M_L = \Delta_\top^T M \Delta_\top$, $M_E = \Delta_\perp^T M \Delta_\perp$, and

$$\begin{bmatrix} C_L & C_{LE} \\ C_{LE} & C_E \end{bmatrix} = \Delta^T (M\dot{\Delta} + C\Delta)$$

The decomposed dynamics (2.2) satisfies the following.

- M_L and M_E are symmetric and positive definite.
- $\dot{M}_L - 2C_L$ and $\dot{M}_E - 2C_E$ are skew symmetric.
- $C_{LE} = -C_{EL}^T$
- Kinetic energy and power are decomposed s.t.

$$\kappa(t) = \kappa_L(t) + \kappa_E(t), \quad \tau^T \dot{q} = \tau_L^T v_L + \tau_E^T v_E$$

where $\kappa_L = \frac{1}{2} v_L^T M_L v_L$ and $\kappa_E = \frac{1}{2} v_E^T M_E v_E$ and

2.1.2 Nonholonomic Passive Decomposition

In our scenario, multiple nonholonomic WMRs are under the mixed constraint, i.e., the physical/nonholonomic constraint (i.e., unconstrained distribution \mathcal{D}^\top) and the artificial/holonomic requirement (i.e., tangential and normal distributions $\Delta^\top, \Delta^\perp$). The unconstrained distribution \mathcal{D}^\top characterizes the sub-space of velocity respecting the nonholonomic Pfaffian constraint given by

$$A(q)\dot{q} = 0$$

To facilitate the analysis and control synthesis for the two WMRs under this mixed constraint, we utilize the kinematic version of the nonholonomic passive decomposition [11, 40]. We also refer readers to [11, 40] for more details and explanations of the nonholonomic passive decomposition.

The nonholonomic passive decomposition of general robotic systems is given by [11, 40]:

$$\mathcal{D}^\top = (\mathcal{D}^\top \cap \Delta^\top) \oplus (\mathcal{D}^\top \cap \Delta^\perp) \oplus \mathcal{D}^c \quad (2.3)$$

where $(\mathcal{D}^\top \cap \Delta^\top)$ and $(\mathcal{D}^\top \cap \Delta^\perp)$ are called (unconstrained) *locked and shape distributions*, respectively representing the tangential (i.e., $h(q)$ locked) and normal (i.e., $h(q)$ changing) components to the level set $\mathcal{H}_{h(q)}$ (2.1) among the permissible robot motion in \mathcal{D}^\top (i.e., satisfying nonholonomic constraint). The distribution \mathcal{D}^c is called *quotient distribution*, which is still permissible, yet, contains both the tangential and normal components to the level set $\mathcal{H}_{h(q)}$ and cannot be split either into tangential or normal direction only. As to be shown below, for the cooperative WMRs, $\mathcal{D}^c \neq \emptyset$, implying weak decomposability [11].

Chapter 3

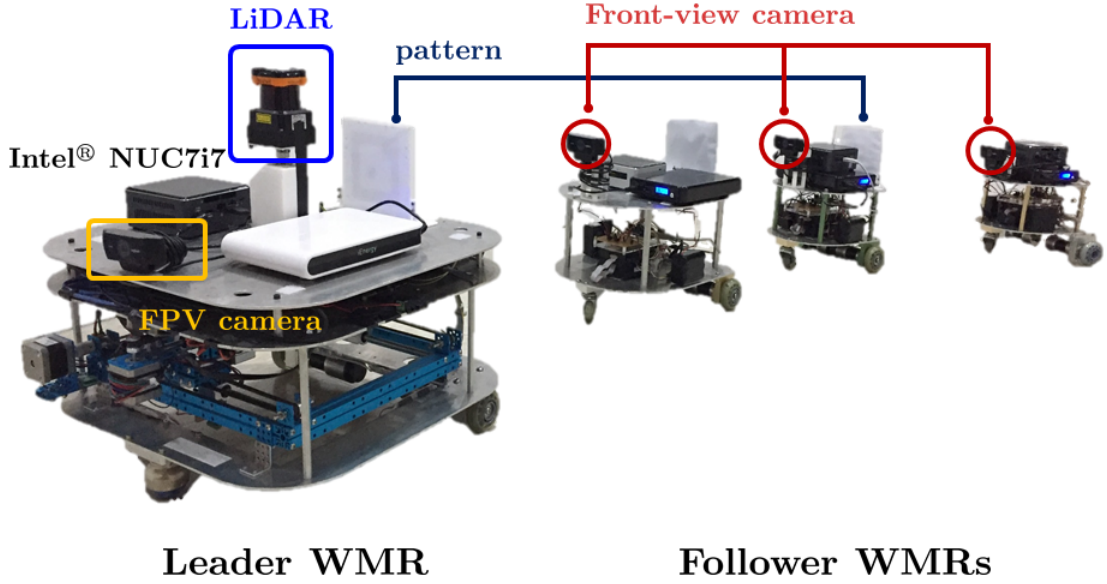
Semi-Autonomous Teleoperation of Nonholonomic Wheeled Mobile Robots with Distributed Communication

3.1 Distributed Control Design

3.1.1 Nonholonomic Passive Decomposition

Here, our goal is to design the control action for each WMR in such a way that the platoon can maintain the n -trailer formation (i.e., line graph topology) regardless of (arbitrary) user command while fully respecting the nonholonomic constraint and the distribution requirement. For this, we consider the kinematic equation of the n -WMRs, which we find adequate as shown in Sec. 3.4, as the WMR operation speed in this thesis is not so fast with both the dynamics effect and the wheel-ground slip/drift effect rather negligible.

Let us denote the inertial frame by $\{\mathcal{O}\}$ and the body-fixed frame of the j -th WMR by $\{\mathcal{G}_j\}$ with $j = 1$ being the “smart” leader WMR and $j = 2, \dots, n$ for the “simple” follower WMRs. Here, we attach the origin of $\{\mathcal{G}_j\}$ at the axle-center each



communication for control and estimation

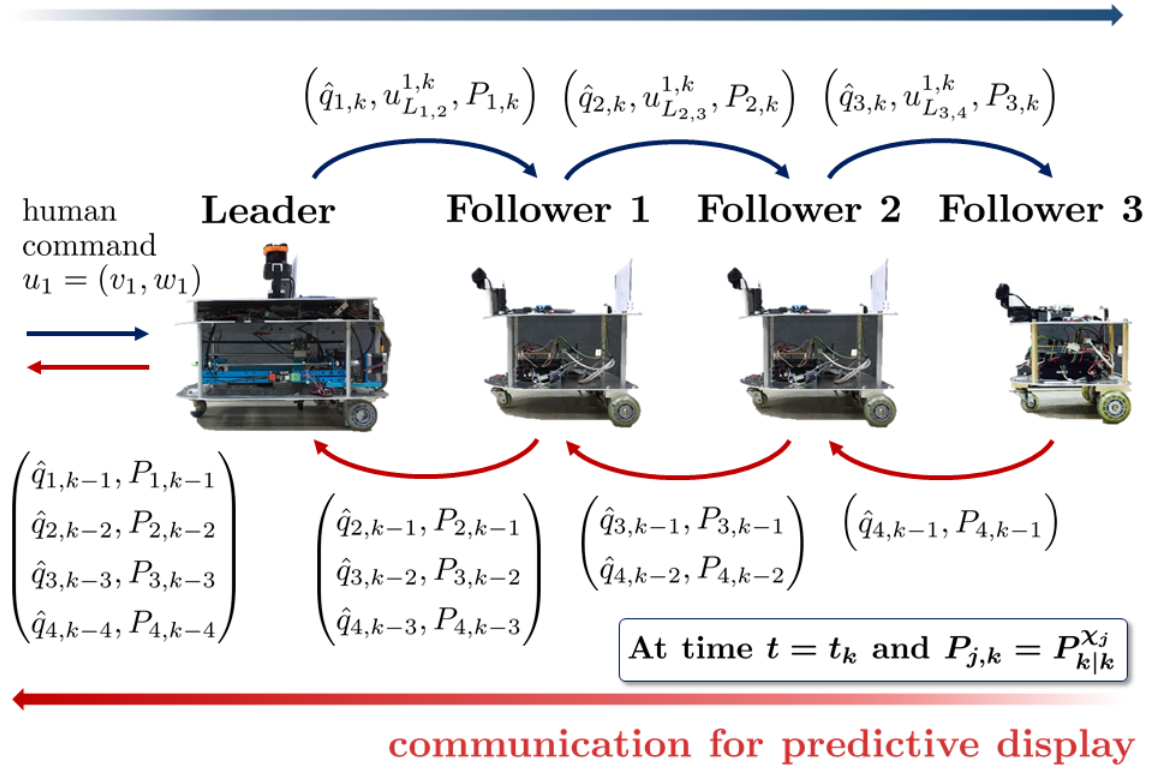


Figure 3-1: Platoon of distributed nonholonomic WMRs: one “smart” leader WMR (with LiDAR, IMU and FPV camera) and three “simple” follower WMRs (with monocular camera and IMU) (top). Peer-to-peer communication architecture among the WMRs and the information flowing through it (bottom).

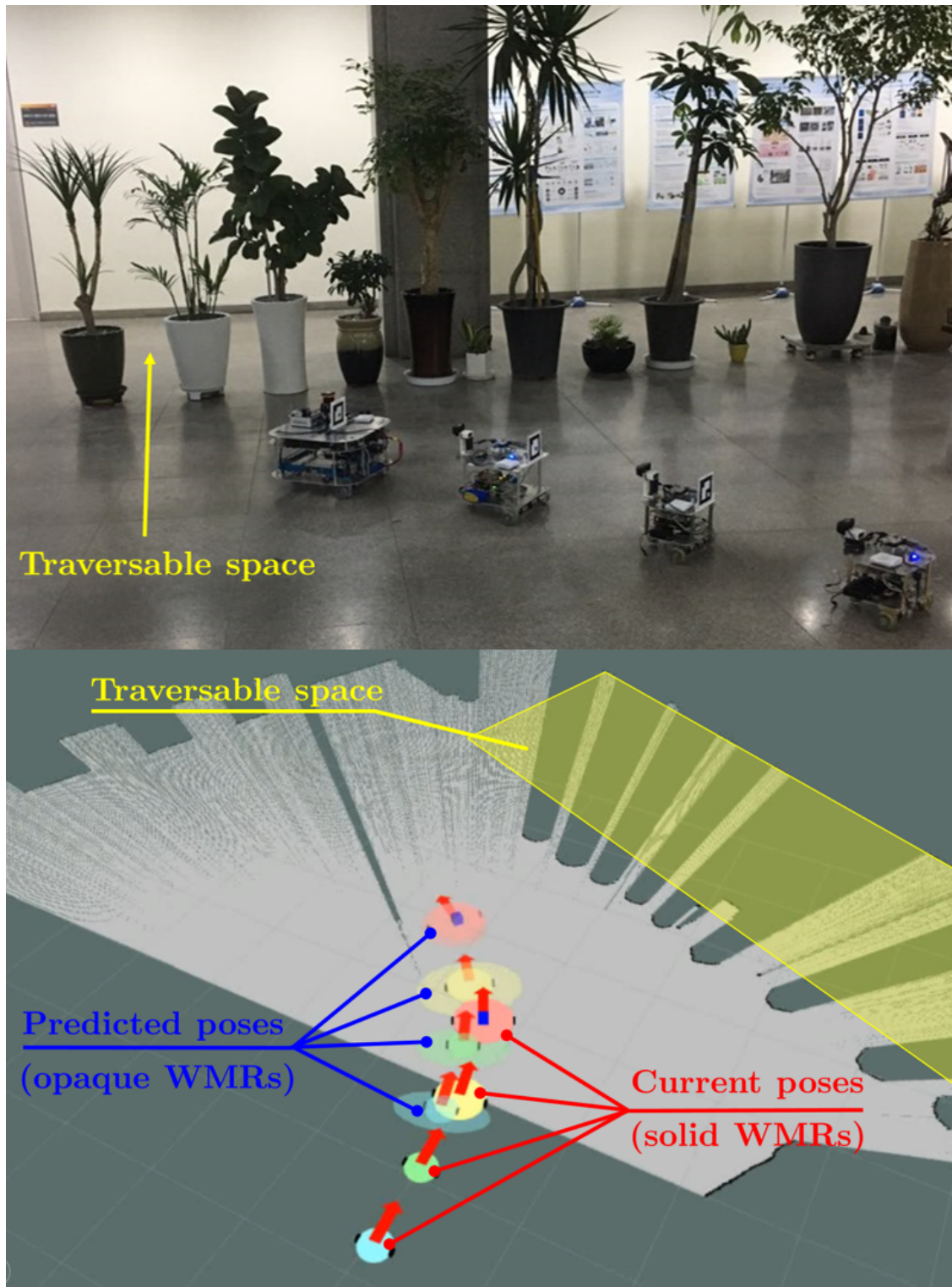


Figure 3-2: Platoon of distributed WMRs navigating in a large-hall with array of plant pots (top); and predictive display view with LiDAR-SLAM map, current and future pose estimates of the WMRs with uncertainty (i.e., size ellipsoids and direction cone) (bottom). Possible collision of a WMR will be indicated by white circular shade, if its future pose estimate collides with non-traversable scanned regions of the SLAM map (see bottom middle two pictures of Fig. 3-11).

j -th WMR. See Fig. 3-3. The pose of each WMR in $\text{SE}(2)$ can then be parameterized by its axle-center position $p_j := (x_j, y_j) \in \mathbb{R}^2$ and heading angle $\phi_j \in \mathbb{S}$ of $\{\mathcal{G}_j\}$ w.r.t. $\{\mathcal{O}\}$. Define the configuration of the j -th WMR by $q_j = [x_j; y_j; \phi_j] \in \mathbb{R}^3$. It is then well-known that the no-slip/drift condition can be written by the following Pfaffian constraint:

$$A_j(q_j)\dot{q}_j = 0$$

with $A_j(q_j) := \begin{bmatrix} \sin \phi_j & -\cos \phi_j & 0 \end{bmatrix} \in \mathbb{R}^{1 \times 3}$, which is well-known to be completely nonholonomic [41].

Here, we aim to design the formation control to be distributed to each pair of two fore-running and following WMRs. For this, let us define the configuration of the pair of the j -th and $(j+1)$ -th WMRs by

$$q_{j,j+1} := \begin{bmatrix} q_j; & q_{j+1} \end{bmatrix} = \begin{bmatrix} x_j; & y_j; & \phi_j; & x_{j+1}; & y_{j+1}; & \phi_{j+1} \end{bmatrix} \in \mathbb{R}^6$$

with their no-slip/drift conditions given by

$$A_{j,j+1}\dot{q}_{j,j+1} = 0 \tag{3.1}$$

with $A_{j,j+1}(q_{j,j+1}) := \text{diag}[A_j(q_j), A_{j+1}(q_{j+1})] \in \mathbb{R}^{2 \times 6}$. The unconstrained distribution $\mathcal{D}_{j,j+1}^\top(q)$ [11], which characterizes the sub-space of the velocity respecting the nonholonomic constraint (3.1), can then be identified by

$$\mathcal{D}_{j,j+1}^\top := \begin{bmatrix} c\phi_j & s\phi_j & 0 & 0 & 0 & 0 \\ 0 & 0 & 1 & 0 & 0 & 0 \\ 0 & 0 & 0 & c\phi_{j+1} & s\phi_{j+1} & 0 \\ 0 & 0 & 0 & 0 & 0 & 1 \end{bmatrix}^T \in \mathbb{R}^{6 \times 4}$$

where $c\phi_j := \cos \phi_j$ and $s\phi_j := \sin \phi_j$. Here, note that $\mathcal{D}_{j,j+1}^\top$ identifies the null-space of $A_{j,j+1} \in \mathbb{R}^{2 \times 6}$ in (3.1). Evolution of the two WMRs under the nonholonomic con-

straint (3.1) can then be written by the following drift-less nonlinear control equation:

$$\dot{q}_{j,j+1} = \mathcal{D}_{j,j+1}^\top u_{j,j+1} \quad (3.2)$$

where $u_{j,j+1} := [v_j; w_j; v_{j+1}; w_{j+1}] \in \mathbb{R}^4$ is the control input, with $v_j, w_j \in \mathbb{R}$ being the forward and angular velocity commands of the j -th WMR. The constraint (3.1) is also completely nonholonomic [41].

The control objective to render the n -WMRs as a n -trailer system (i.e., line graph topology) can be written by the following pairwise/distributed virtual constraint:

$$h_{j,j+1} := \begin{pmatrix} x_j - x_{j+1} - L_j \text{c} \phi_{j+1} \\ y_j - y_{j+1} - L_j \text{s} \phi_{j+1} \end{pmatrix} = 0 \quad (3.3)$$

where $L_j > 0$ is the desired distance between the j -th WMR and the $(j+1)$ -th WMR. This constraint (3.3) implies that the distance between the two WMRs' axle-centers is maintained to be L_j with the camera of the ensuing WMR always pointing to the axle-center of the fore-running WMR. This then means that, if $h_{j,j+1} = 0$, the axle-center of the fore-running WMR will always be within the limited FOV (field-of-view) of the following WMR's camera *regardless* of the platoon formation shape and curvature. This further implies that, if $h_{j,j+1} = 0$, with the omni-directional fiducial markers (e.g., cube with tags on each side) attached at those axle-centers, each following WMR can always measure the relative distance and bearing from its fore-running WMR with their onboard camera, while the platoon moves/undulates as a n -trailer system. See Fig. 3-3. This $h(q)$ is called *formation map* [11]. The control objective $h_{j,j+1} = 0$ needs to be attained while respecting the distribution requirement.

For this, following [39], we define *tangential distribution* $\Delta_{j,j+1}^\top$ of $h_{j,j+1}$ to be the

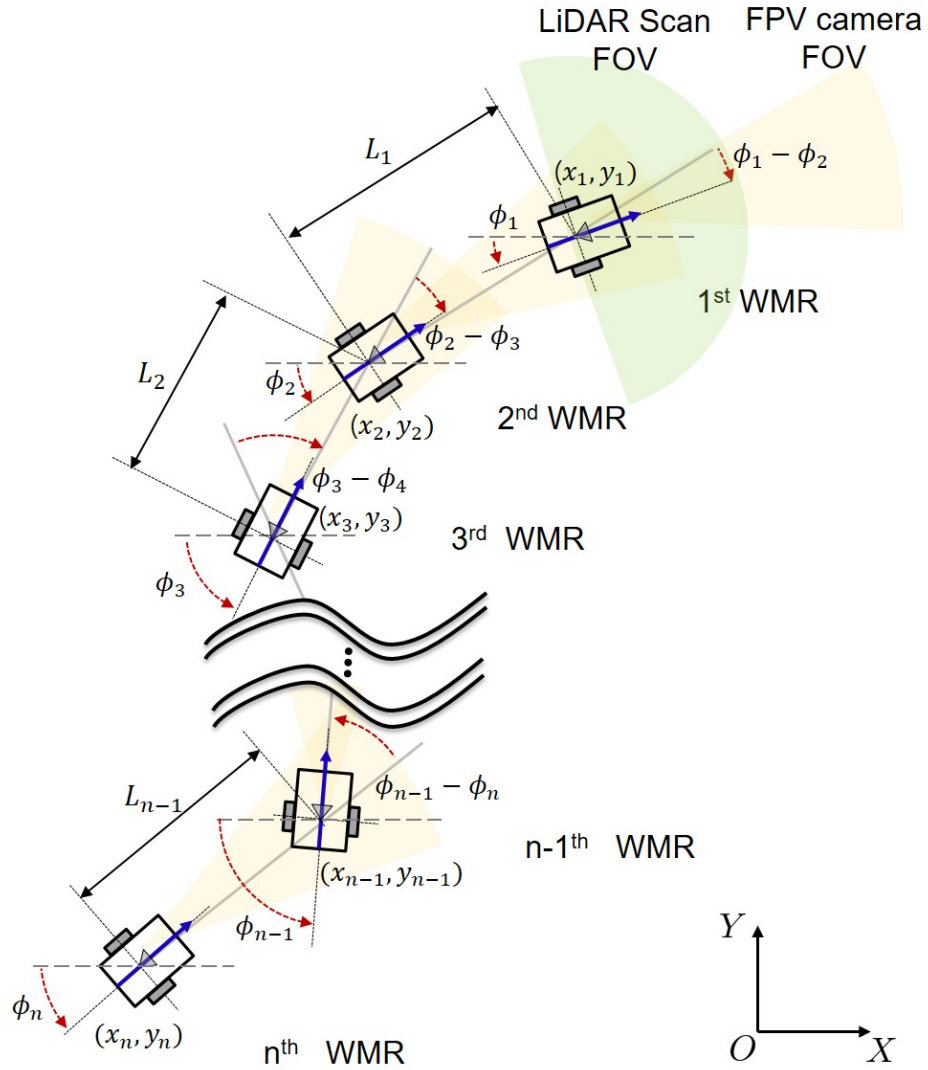


Figure 3-3: Geometry of platoon of the distributed nonholonomic WMRs, when they collectively behave as the n -trailer system under the virtual constraint $h(q_{j,j+1}) = 0$, that is, each following WMR maintains the distance L_j from, and also faces toward the axle-center of, their respective fore-running WMR.

null-space of the one-form $\frac{\partial h_{j,j+1}}{\partial q_{j,j+1}} \in \mathbb{R}^{2 \times 6}$ as identified by the following matrix:

$$\Delta_{j,j+1}^\top := \begin{bmatrix} L_j s \phi_{j+1} & -L_j c \phi_{j+1} & 0 & 0 & 0 & -1 \\ 1 & 0 & 0 & 1 & 0 & 0 \\ 0 & 1 & 0 & 0 & 1 & 0 \\ 0 & 0 & 1 & 0 & 0 & 0 \end{bmatrix}^T \in \mathbb{R}^{6 \times 4}$$

and *normal distribution* $\Delta_{j,j+1}^\perp(q_{j,j+1})$, which is the orthogonal complement of $\Delta_{j,j+1}^\top$ w.r.t. the Euclidean metric s.t.,

$$\Delta_{j,j+1}^\perp := \begin{bmatrix} 1 & 0 & 0 & -1 & 0 & L_j s \phi_{j+1} \\ 0 & 1 & 0 & 0 & -1 & -L_j c \phi_{j+1} \end{bmatrix}^T \in \mathbb{R}^{6 \times 2}$$

with $\Delta_{j,j+1}^\perp = \left(\frac{\partial h_{j,j+1}}{\partial q_{j,j+1}} \right)^T$. As explained in [39], the velocity component in $\Delta_{j,j+1}^\top$ characterizes the motion of the two WMRs tangential to the (current) level set:

$$\mathcal{H}_{h_{j,j+1}}(q_{j,j+1}) := \{q' \in \mathbb{R}^6 \mid h(q') = h(q_{j,j+1})\} \quad (3.4)$$

(i.e., collective motion of the two WMRs with $h_{j,j+1}$ kept intact); whereas that in $\Delta_{j,j+1}^\perp$ the motion normal to the level set $\mathcal{H}_{h_{j,j+1}}$ w.r.t. the Euclidean metric (i.e., internal motion of the two WMRs changing the inter-WMR coordination $h_{j,j+1}$).

Following [42], we can then achieve the nonholonomic passive decomposition of the two WMRs under the physical nonholonomic constraint (3.1) and the virtual holonomic constraint (3.3) s.t.,

$$\dot{q}_{j,j+1} = \underbrace{\begin{bmatrix} (\mathcal{D}_{j,j+1}^\top \cap \Delta_{j,j+1}^\top) & \mathcal{D}_{j,j+1}^c \end{bmatrix}}_{=: S_{j,j+1}(q_{j,j+1}) \in \mathbb{R}^{6 \times 4}} \begin{pmatrix} u_{L_{j,j+1}} \\ u_{C_{j,j+1}} \end{pmatrix} \quad (3.5)$$

where

$$(\mathcal{D}_{j,j+1}^\top \cap \Delta_{j,j+1}^\top) = \begin{bmatrix} \text{c} \phi_j & 0 \\ \text{s} \phi_j & 0 \\ 0 & 1 \\ \text{c}(\phi_j - \phi_{j+1}) \text{c} \phi_{j+1} & 0 \\ \text{c}(\phi_j - \phi_{j+1}) \text{s} \phi_{j+1} & 0 \\ \frac{1}{L_j} \text{s}(\phi_j - \phi_{j+1}) & 0 \end{bmatrix} \in \mathbb{R}^{6 \times 2} \quad (3.6)$$

is the (unconstrained) *locked distribution*, representing the motion tangential to the level set $\mathcal{H}_{h_{j,j+1}}$ (3.4) (i.e., collective motion with $h_{j,j+1}$ locked) among the permissible motion in $\mathcal{D}_{j,j+1}^\top$ (i.e., satisfying the nonholonomic constraint (3.1)); and

$$\begin{aligned} \mathcal{D}_{j,j+1}^c &= \mathcal{D}_{j,j+1}^\top \setminus (\mathcal{D}_{j,j+1}^\top \cap \Delta_{j,j+1}^\top) = \\ &= \begin{bmatrix} \text{c} \phi_j & 0 \\ \text{s} \phi_j & 0 \\ 0 & 0 \\ -\text{c}(\phi_j - \phi_{j+1}) \text{c} \phi_{j+1} & \text{s}(\phi_j - \phi_{j+1}) \text{c} \phi_{j+1} \\ -\text{c}(\phi_j - \phi_{j+1}) \text{s} \phi_{j+1} & \text{s}(\phi_j - \phi_{j+1}) \text{s} \phi_{j+1} \\ -L_j \text{s}(\phi_j - \phi_{j+1}) & -L_j \text{c}(\phi_j - \phi_{j+1}) \end{bmatrix} \end{aligned} \quad (3.7)$$

is the *quotient distribution* with $\mathcal{D}_{j,j+1}^c \notin \Delta_{j,j+1}^\top$ and $\mathcal{D}_{j,j+1}^c \notin \Delta_{j,j+1}^\perp$ (i.e., weakly decomposable [11]) and also $(\mathcal{D}_{j,j+1}^\top \cap \Delta_{j,j+1}^\perp) \subset \mathcal{D}_{j,j+1}^c$ (see [42]). This then means that, for the two WMRs under the control objective (3.3): 1) we can ensure the inter-WMR coordination $h_{j,j+1} = 0$ simply by stabilizing the motion of the WMRs in this $\mathcal{D}_{j,j+1}^c$; yet, 2) it is not possible to adjust the inter-WMR coordination $h_{j,j+1}$ without affecting the collective motion (i.e., tele-driving) aspect, since $\mathcal{D}_{j,j+1}^c$ contains both the normal and tangential components. Complete decoupling between these two aspects can be attained only if strong decomposability is granted [11], which is not the case here.

3.1.2 Control Design and Distribution

The matrix $S_{j,j+1}$ in (3.5) is called the decomposition matrix. In (3.5), $u_{C_{j,j+1}} = [u_{C_{j,j+1}}^1; u_{C_{j,j+1}}^2] \in \mathbb{R}^2$ and $u_{L_{j,j+1}} = [u_{L_{j,j+1}}^1; u_{L_{j,j+1}}^2] \in \mathbb{R}^2$ are respectively the control inputs of the quotient and locked systems, with the former to be utilized to regulate the inter-WMR coordination (i.e., $h_{j,j+1} \rightarrow 0$) while the latter to tele-drive the two WMRs while not perturbing the inter-WMR coordination aspect $h_{j,j+1}$. These controls $(u_{L_{j,j+1}}, u_{C_{j,j+1}}) \in \mathbb{R}^4$ should also be distributable to each WMR according to their sensing, computing and communication architecture (see Fig. 3-1).

The fact that $\mathcal{D}_{j,j+1}^c$ contains some components in $\Delta_{j,j+1}^\perp$ implies that, by using $u_{C_{j,j+1}}$, we can affect/regulate the inter-WMR coordination $h_{j,j+1}$. For this, we design $u_{C_{j,j+1}} \in \mathbb{R}^2$ s.t.,

$$u_{C_{j,j+1}} = -\mathcal{D}_{j,j+1}^{cT}(q_{j,j+1}) \cdot \left[\frac{\partial h_{j,j+1}}{\partial q_{j,j+1}} \right]^T \left[\frac{\partial \varphi_{h_{j,j+1}}}{\partial h_{j,j+1}} \right]^T \quad (3.8)$$

where $\varphi_{h_{j,j+1}}(h_{j,j+1}) \geq 0$ is a suitably defined positive-definite potential function to enforce $h_{j,j+1} = 0$ (i.e., $\varphi_{h_{j,j+1}} = 0$ iff $h = 0$ and positively quadratic around $h = 0$ with $\frac{\partial \varphi_{h_{j,j+1}}}{\partial h_{j,j+1}} = 0$ iff $\varphi_{h_{j,j+1}} = 0$ in a neighborhood of $h_{j,j+1} = 0$). We then have:

$$\begin{aligned} \frac{d\varphi_{h_{j,j+1}}}{dt} &= \frac{\partial \varphi_{h_{j,j+1}}}{\partial h_{j,j+1}} \frac{\partial h_{j,j+1}}{\partial q_{j,j+1}} \dot{q}_{j,j+1} \\ &= \frac{\partial \varphi_{h_{j,j+1}}}{\partial h_{j,j+1}} \frac{\partial h_{j,j+1}}{\partial q_{j,j+1}} \mathcal{D}_{c_{j,j+1}} u_{C_{j,j+1}} \\ &= -\|u_{C_{j,j+1}}\|^2 \leq 0 \end{aligned} \quad (3.9)$$

where we use the fact that $\frac{\partial h_{j,j+1}}{\partial q_{j,j+1}} \cdot [\mathcal{D}_{j,j+1}^\top \cap \Delta_{j,j+1}^\top] \cdot u_{L_{j,j+1}} = 0 \ \forall u_{L_{j,j+1}}$ from the geometric construction of (3.5). This then means that $\varphi_{h_{j,j+1}}(t) \leq \varphi_{h_{j,j+1}}(0), \forall t \geq 0$, that is, if the inter-WMR coordination error starts small (i.e., $\|h_{j,j+1}(0)\| \approx 0$), it will stay small (i.e., $\|h_{j,j+1}(t)\| \approx 0, \forall t \geq 0$). Further, this error $\varphi_{h_{j,j+1}}$ will be strictly decreasing as long as $u_{C_{j,j+1}} \neq 0$. This also implies that, if we start with small enough $h_{j,j+1}(0)$ with $|\phi_j(0) - \phi_{j+1}(0)| < \pi, |\phi_j(t) - \phi_{j+1}(t)| < \pi \ \forall t \geq 0$ (i.e., heading angle ϕ_j in Fig. 3-3 will not flip around), since, if not, $\varphi_{h_{j,j+1}}(t)$ should increase, contradictory

to $\varphi_{h_{j,j+1}}(t) \leq \varphi_{h_{j,j+1}}(0)$, $\forall t \geq 0$. Here, note that the control $u_{C_{j,j+1}}$ is distributed, as it is a function of only $q_{j,j+1}$.

With the inter-WMR coordination $\|h_{j,j+1}\| \rightarrow 0$ for each pair among the n -WMRs attained by $u_{C_{j,j+1}}$ in (3.8), the remaining task is then to tele-drive the collective of those pairs without perturbing $h_{j,j+1} \rightarrow 0$ in a distributed fashion. This can be done if (and only if) by driving them via the locked system control $u_{L_{j,j+1}}$ as can be seen from the nonholonomic passive decomposition (3.5). Here, note that, if $h_{j,j+1} \rightarrow 0$, $u_{C_{j,j+1}} \rightarrow 0$ from the construction of $\varphi_{h_{j,j+1}}$; and, if $u_{C_{j,j+1}} \rightarrow 0$, $u_{L_{j,j+1}} \rightarrow (v_j, w_j)$ from (3.5) with (3.6). To design $u_{L_{j,j+1}}$, let us start with the leader WMR with $j = 1$. This leader WMR serves as the “eyes” of the remote user and will be directly tele-controlled by them. This means that (v_1, w_1) is given. From (3.5) with (3.6)-(3.7), we then have

$$\begin{aligned} v_1 &= u_{L_{1,2}}^1 + u_{C_{1,2}}^1 \\ w_1 &= u_{L_{1,2}}^2 \end{aligned}$$

from which we can define $u_{L_{j,j+1}}$ s.t.,

$$\begin{pmatrix} u_{L_{1,2}}^1 \\ u_{L_{1,2}}^2 \end{pmatrix} = \begin{pmatrix} v_1 - u_{C_{1,2}}^1 \\ w_1 \end{pmatrix} \quad (3.10)$$

where recall that $u_{C_{j,j+1}}$ is already specified by (3.8) as a function of only $q_{j,j+1}$.

Now, suppose that the control input (v_j, w_j) of the j -th WMR is given. Then, from (3.5) with (3.6)-(3.7), similar to (3.10), the locked system control $u_{L_{j,j+1}}$ can be obtained by

$$\begin{pmatrix} u_{L_{j,j+1}}^1 \\ u_{L_{j,j+1}}^2 \end{pmatrix} = \begin{pmatrix} v_j - u_{C_{j,j+1}}^1 \\ w_j \end{pmatrix} \quad (3.11)$$

where again $u_{C_{j,j+1}}$ is fully specified by (3.8) as a function of only $q_{j,j+1}$. With $(u_{L_{j,j+1}}, u_{C_{j,j+1}})$ now both determined, again from (3.5) with (3.6)-(3.7), we can com-

pute the forward and angular velocity inputs of the $(j + 1)$ -th WMR by

$$v_{j+1} = u_{L_{j,j+1}}^1 c(\phi_j - \phi_{j+1}) - \begin{bmatrix} c(\phi_j - \phi_{j+1}) & -s(\phi_j - \phi_{j+1}) \end{bmatrix} u_{C_{j,j+1}} \quad (3.12)$$

$$w_{j+1} = \frac{1}{L_j} u_{L_{j,j+1}}^1 s(\phi_j - \phi_{j+1}) - L_j \begin{bmatrix} s(\phi_j - \phi_{j+1}) & c(\phi_j - \phi_{j+1}) \end{bmatrix} u_{C_{j,j+1}} \quad (3.13)$$

Given (v_{j+1}, w_{j+1}) of the $(j + 1)$ -th WMR, we can also compute $u_{L_{j+1,j+2}}$ for the pair of the $(j + 1)$ -th WMR and $(j + 2)$ -th WMR similar to (3.11) by

$$\begin{pmatrix} u_{L_{j+1,j+2}}^1 \\ u_{L_{j+1,j+2}}^2 \end{pmatrix} = \begin{pmatrix} v_{j+1} - u_{C_{j+1,j+2}}^1 \\ w_{j+1} \end{pmatrix} \quad (3.14)$$

where, again, $u_{C_{j+1,j+2}}$ is already specified by (3.8) as a function of only $q_{j+1,j+2}$. By repeating this process down to the n -th WMR, we can specify the control input (v_j, w_j) for all the WMRs, $j = 1, \dots, n$, which will ensure the $(j + 1)$ -th WMR to follow the j -th WMR (moving with (v_j, w_j)) while enforcing the inter-WMR coordination requirement (i.e., $h_{j,j+1} \rightarrow 0$) *regardless* of the user command (v_1, w_1) of the leader WMR.

Here, note that the control (3.12)-(3.13) of the $(j + 1)$ -th WMR is only a function of $q_{j,j+1} = [q_j; q_{j+1}]$ and $u_{L_{j,j+1}}^1$, where q_j and $u_{L_{j,j+1}}^1$ are already known by the j -th WMR (with (3.11)), thus, can be transmitted to the $(j + 1)$ -th WMR via the peer-to-peer communication, and q_{j+1} can be estimated by using the onboard sensor of the $(j + 1)$ -th WMR with q_j received from the j -th WMR via the communication. This then shows that the control (3.12)-(3.13) is indeed distributed, requiring only onboard sensing and peer-to-peer communication. Here, we also assume the transmission delay between two WMRs via their peer-to-peer communication (with the data loss also included) be negligible as compared to the operation speed of the WMRs. This is necessary for the properly working of the distributed control (3.12)-(3.13), and granted for our experimental setup as well (i.e., WMR speed slower than 0.5m/s with 250Hz communication rate and near zero data loss - see Sec. 3.4). This transmission delay effect will be substantial though for the predictive display, when the number of the WMRs is large - see Sec. 3.3.

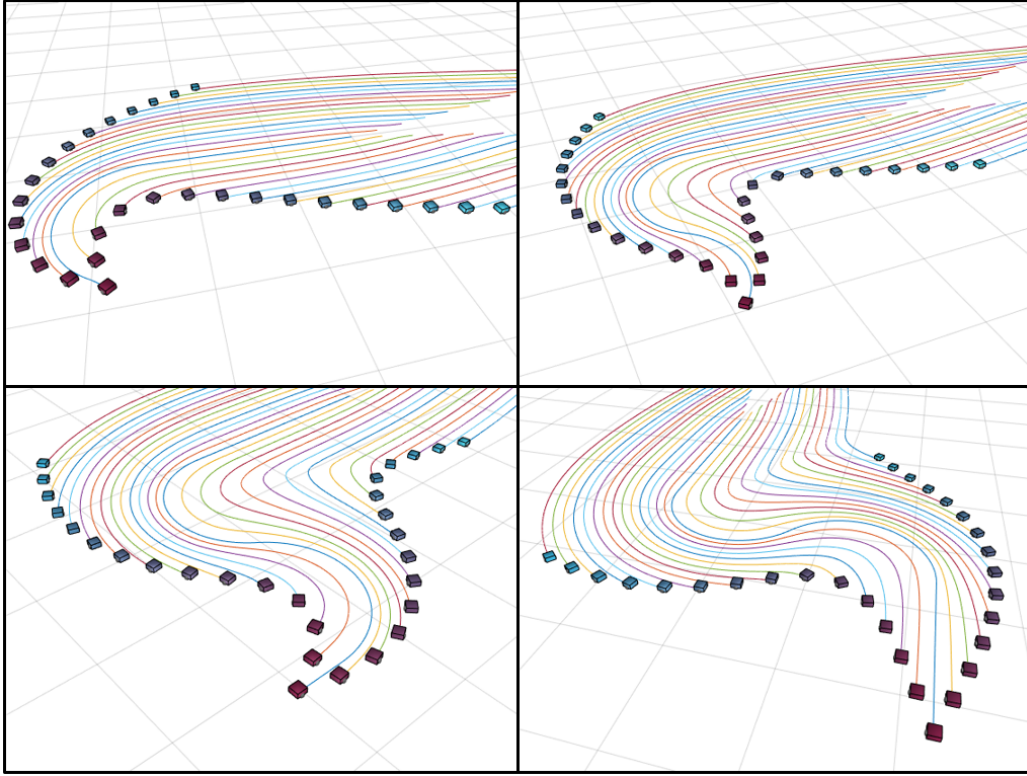


Figure 3-4: Simulation result of the platoon of 30 WMRs making a triangular formation under the distributed control (3.12)-(3.13) and the modified formation map (3.18) with the camera-heading offset angle α_j to slant the two branches of the formation from each other.

Now, suppose that we start with $||h_{j,j+1}(0)|| \approx 0$ for all $j = 1, \dots, n-1$. Then, as stated before (3.11), $u_{C_{j,j+1}} \approx 0$ as well, $\forall j = 1, 2, \dots, n-1$. This then implies from (3.5) with (3.6)-(3.7) that

$$u_{L_{j,j+1}}^1 \approx v_j, \quad u_{L_{j,j+1}}^2 \approx w_j$$

which, from (3.12), further implies that

$$v_{j+1} \approx v_j c(\phi_j - \phi_{j+1}), \quad w_{j+1} \approx \frac{v_j}{L_j} s(\phi_j - \phi_{j+1}) \quad (3.15)$$

or, equivalently,

$$v_{j+1} \approx v_1 \cdot \prod_{p=1}^j c(\phi_p - \phi_{p+1}) \quad (3.16)$$

$$w_{j+1} \approx \frac{v_1}{L_j} s(\phi_j - \phi_{j+1}) \cdot \prod_{p=1}^{j-1} c(\phi_p - \phi_{p+1}) \quad (3.17)$$

Here, note that if all the WMRs are aligned (i.e., $\phi_j = \phi_{j+1}$), $v_j \rightarrow v_1$ with $w_j = 0$ $\forall j = 1, 2, \dots, n$, i.e., pulling the straight-line platoon by its leader WMR. On the other hand, if $\phi_j - \phi_{j+1} = \pi/2$, $w_{j+1} = \frac{v_j}{L}$ with $v_{j+1} = 0$, i.e., pulling the upright stem of the reversed “L”-shape normal to its bottom horizontal line with only the $(j+1)$ -th WMR (i.e., horizontal line end) instantaneously rotating to keep its heading directed to the axle-center of the j -th WMR (i.e., stem end). This is in a stark contrast with the work of [42], where a pair of two WMRs is “pushed” by the follower WMR in a centralized manner with external MOCAP (motion capture system).

Although developed here only for the line graph topology for simplicity, our framework can also incorporate any directed tree graph topology among the WMRs, by attaching line branch to its preceding stem branch with the leader WMR as the globally reachable root of the whole tree graph [43, 44]. For this, separation among the branches can easily be achieved by using the same formation map $h_{j,j+1}$ (3.3), yet, with some offset between the onboard camera direction and the heading direction of

the WMR, i.e.,

$$h_{j,j+1} := \begin{pmatrix} x_j - x_{j+1} - L_j \text{c}(\phi_{j+1} + \alpha_{j+1}) \\ y_j - y_{j+1} - L_j \text{s}(\phi_{j+1} + \alpha_{j+1}) \end{pmatrix} = 0 \quad (3.18)$$

where $\alpha_{j+1} \in \mathfrak{R}$ is the constant offset angle. If $h_{j,j+1} = 0$, the branch will then be “slanting” by the angle of α_{j+1} from its stem branch. See Fig. 3-4, where this slanting is used to attain a triangular formation among the WMRs. Note also that, since the sensing, computation and communication are all distributed and also the control (3.12)-(3.13) is uni-directional, any tree sub-graph can be removed or added from the downstream of the platoon without influencing at all the performance of its upstream WMRs. This implies scalability of our proposed framework.

The nonholonomic passive decomposition and its behavior decomposition (e.g., (3.12)-(3.13)) turns out to greatly simplify the uncertainty propagation computation for the predictive display in Sec. 3.3, as it allows us to consider only the collective driving aspect (i.e., with $u_{L,j,j+1}$), not the inter-WMR coordination aspect, which is regulated locally by $u_{C,j,j+1}$. This is in a stark contrast to [20], where the same control objective (3.3) is attained for distributed nonholonomic WMRs, yet, without such a behavior decomposition. Thus, for the uncertainty propagation computation, the full kinematics both with the collective and coordination aspects should be used, which can substantially increase computation complexity as the closed-loop kinematics contains many nonlinearity therein. The passive decomposition was also used in [24] (centralized holonomic robots), [30] (partially-distributed holonomic robots), [31] (distributed holonomic robots), [12] (nonholonomic, yet, centralized), and in [42] (nonholonomic, yet, only two WMRs and centralized). However, its application to distributed nonholonomic WMRs is done for the first time in this thesis.

3.2 Distributed Pose Estimation

3.2.1 EKF Pose Estimation of Leader WMR

The leader WMR runs the SLAM algorithm of [45, 46] with the LiDAR sensor. This LiDAR-SLAM is running at 40Hz with the LiDAR scanning period. For smoother and more accurate pose estimation, we fuse this LiDAR-SLAM pose information with the IMU data via extended Kalman filtering (EKF). For this, following [47, 48], we utilize the IMU data (only (x, y) -accelerometer and yaw gyroscope used) for the EKF propagation step (with 250Hz), while the LiDAR-SLAM data for the EKF measurement update (with 40Hz). We also adopt the technique of error-state EKF for faster and more robust estimation performance.

More precisely, we define the state for this LiDAR-IMU sensor fusion s.t.,

$$\chi_1 := \begin{bmatrix} p_1; & \xi_1; & \phi_1; & b_{a_1}; & b_{g_1} \end{bmatrix} \in \mathbb{R}^8 \quad (3.19)$$

where $p_1 := [x_1; y_1] \in \mathbb{R}^2$, $\xi_1 := [\dot{x}_1; \dot{y}_1] \in \mathbb{R}^2$, and $b_{a_1} = [b_{a_1,x}; b_{a_1,y}] \in \mathbb{R}^2$ and $b_{g_1} \in \mathbb{R}$ are the biases of the accelerometer and gyroscope measurements, each modeled as random-walk processes driven by zero-mean white Gaussian noise $n_{wa_1} \in \mathbb{R}^2$ and $n_{wg_1} \in \mathbb{R}$, respectively. The continuous-time state equation is then given by

$$\begin{aligned} \dot{p}_1(t) &= \xi_1(t), & \dot{\xi}_1(t) &= a_1(t), & \dot{\phi}_1(t) &= \omega_1(t) \\ \dot{b}_{a_1}(t) &= n_{wa_1}(t), & \dot{b}_{g_1}(t) &= n_{wg_1}(t) \end{aligned} \quad (3.20)$$

where $a_1(t) \in \mathbb{R}^2$ is the acceleration of the leader WMR expressed in $\{\mathcal{O}\}$. The accelerometer and gyroscope sensor models are also given by

$$\begin{aligned} a_{m_1}(t) &= R_{\mathcal{O}}^{\mathcal{G}_1}(\phi_1(t))a_1(t) + b_{a_1}(t) + n_{a_1}(t) \\ \omega_{m_1}(t) &= \omega_1(t) + b_{g_1}(t) + n_{g_1}(t) \end{aligned} \quad (3.21)$$

where $n_{a_1}(t) \in \mathbb{R}^2$ and $n_{g_1}(t) \in \mathbb{R}$ are the zero mean, white Gaussian measurement noise of the accelerometer and gyroscope sensing, and $R_{\mathcal{O}}^{\mathcal{G}_1} \in \text{SO}(2)$ is the rotation

matrix from the inertial frame $\{\mathcal{O}\}$ to the body-fixed frame of leader WMR $\{\mathcal{G}_1\}$.

Let us define the error state for the EKF s.t.,

$$\tilde{\chi}_1 := \begin{bmatrix} \tilde{p}_1; & \tilde{\xi}_1; & \tilde{\phi}_1; & \tilde{b}_{a_1}; & \tilde{b}_{g_1} \end{bmatrix} \in \mathbb{R}^8$$

where $(\tilde{\cdot}) = (\cdot) - (\hat{\cdot})$ is the difference between the true state (3.19) and the estimated state (obtained by applying the expectation to (3.20)). Then, the linearized continuous-time error state equation is given by

$$\dot{\tilde{\chi}}_1 = F_1(t)\tilde{\chi}_1 + G_1(t)n_1 \quad (3.22)$$

where $n_1 = \begin{bmatrix} n_{a_1}; & n_{wa_1}; & n_{g_1}; & n_{wg_1} \end{bmatrix} \in \mathbb{R}^6$ is the system noise vector, and

$$F_1(t) := \begin{bmatrix} 0_{2 \times 2} & I_2 & 0_{2 \times 1} & 0_{2 \times 2} & 0_{2 \times 1} \\ 0_{2 \times 2} & 0_{2 \times 2} & S\hat{a}_1(t) & -R_{\mathcal{G}_1}^{\mathcal{O}}(\hat{\phi}_1(t)) & 0_{2 \times 1} \\ 0_{1 \times 2} & 0_{1 \times 2} & 0 & 0_{1 \times 2} & -1 \\ 0_{2 \times 2} & 0_{2 \times 2} & 0_{2 \times 1} & 0_{2 \times 2} & 0_{2 \times 1} \\ 0_{1 \times 2} & 0_{1 \times 2} & 0 & 0_{1 \times 2} & 0 \end{bmatrix} \in \mathbb{R}^{8 \times 8}$$

$$G_1(t) := \begin{bmatrix} 0_{2 \times 2} & 0_{2 \times 2} & 0_{2 \times 1} & 0_{2 \times 1} \\ -R_{\mathcal{G}_1}^{\mathcal{O}}(\hat{\phi}_1(t)) & 0_{2 \times 2} & 0_{2 \times 1} & 0_{2 \times 1} \\ 0_{1 \times 2} & 0_{1 \times 2} & -1 & 0 \\ 0_{2 \times 2} & I_2 & 0_{2 \times 1} & 0_{2 \times 1} \\ 0_{1 \times 2} & 0_{1 \times 2} & 0 & 1 \end{bmatrix} \in \mathbb{R}^{8 \times 6}$$

with $\hat{a}_1(t) := R_{\mathcal{G}_1}^{\mathcal{O}}(\hat{\phi}_1(t))(a_{m_1}(t) - \hat{b}_{a_1}(t))$ and $S := [0, -1; 1, 0] \in \mathbb{R}^{2 \times 2}$. This continuous-time equation (3.22) can then be discretized at time t_k by using $\frac{\tilde{\chi}_{1,k+1} - \tilde{\chi}_{1,k}}{dt} = \dot{\tilde{\chi}}_{1,k}$, $dt = t_{k+1} - t_k$, with the IMU information (3.21) as done in [47, 48]. From this discretized equation, we can further obtain the error state covariance propagation equation

tion s.t.,

$$P_{k+1|k}^{X_1} \simeq (I_8 + F_{1,k}dt)P_{k|k}^{X_1}(I_8 + F_{1,k}dt)^T + (G_{1,k}dt)Q_1(G_{1,k}^Tdt)$$

where $F_{1,k} := F_1(t_k)$ and $G_{1,k} := G_1(t_k)$ are the matrices at the time t_k , $P_{k|k}^{X_1}$ is the priori covariance of the leader WMR at k , $P_{k+1|k}^{X_1}$ is its posteriori covariance at k , and $Q_1 := E[n_1n_1^T]$ is the covariance of the noise vector n_1 . As a measurement for EKF, we use the pose measurement obtained by the LiDAR-SLAM, i.e.,

$$z_{\text{SLAM}} = \begin{pmatrix} p_1 \\ \phi_1 \end{pmatrix} + \begin{pmatrix} n_{p_1} \\ n_{\phi_1} \end{pmatrix}$$

where (n_{p_1}, n_{ϕ_1}) are the zero mean, white Gaussian noise of the LiDAR-SLAM pose measurement. Then, the measurement model of the error state is given by

$$\tilde{z}_{\text{SLAM}} = \begin{pmatrix} \tilde{p}_1 \\ \tilde{\phi}_1 \end{pmatrix} + \begin{pmatrix} n_{p_1} \\ n_{\phi_1} \end{pmatrix} = \underbrace{\begin{bmatrix} I_2 & 0_{2 \times 2} & 0_{2 \times 1} & 0_{2 \times 3} \\ 0_{1 \times 2} & 0_{1 \times 2} & 1 & 0_{1 \times 3} \end{bmatrix}}_{=:H_1} \tilde{\chi}_1 + \begin{pmatrix} n_{p_1} \\ n_{\phi_1} \end{pmatrix}$$

which defines the update equation for (3.22). To correct the error state $\tilde{\chi}_1$ with this measurement z_{SLAM} received at $k+1$, the Kalman gain K_{k+1} is computed s.t.,

$$K_{k+1} = P_{k+1|k}^{X_1} H_1^T S_{k+1}^{-1} \quad (3.23)$$

where $S_{k+1} = H_1 P_{k+1|k}^{X_1} H_1^T + R_1$ is the covariance of the residual, and R_1 is the covariance of the measurement. We then update the propagated error state and its covariance s.t.,

$$\begin{aligned} \hat{\chi}_{1,k+1|k+1} &= \hat{\chi}_{1,k+1|k} + K_{k+1} \tilde{z}_{\text{SLAM},k+1} \\ P_{k+1|k+1}^{X_1} &= P_{k+1|k}^{X_1} - P_{k+1|k}^{X_1} H_1^T S_{k+1}^{-1} H_1 P_{k+1|k}^{X_1} \end{aligned} \quad (3.24)$$

3.2.2 EKF Pose Estimation of Follower WMRs

For the pose estimation of the “simple” follower WMRs, we use only low-cost sensors (e.g., monocular camera and IMU). Each follower WMR obtains relative position and bearing measurement from the fore-running WMR by using the monocular camera and fiducial markers similar to [49] attached on the fore-running WMR. This camera information is then fused with IMU via the error-state EKF as done for the leader WMR in Sec. 3.2.1. For this, similar to (3.19), define the sensor fusion state of the j -th follower WMR s.t.,

$$\chi_j := \begin{bmatrix} p_j; & \xi_j; & \phi_j; & b_{a_j}; & b_{g_j} \end{bmatrix} \in \mathbb{R}^8$$

The propagation step of the error-state EKF is then the same as that of the leader WMR. Only the difference is the update step, where the measurement of the camera and the pose estimate of the $(j - 1)$ -th WMR received from the communication are used.

First, the camera measurement model is given by

$$z_{j,\text{camera}} = \begin{pmatrix} z_p \\ z_\phi \end{pmatrix} + \begin{pmatrix} n_{p_j} \\ n_{\phi_j} \end{pmatrix}$$

where $z_p := R_{\mathcal{O}}^{\mathcal{G}_j}(\phi_j) (p_{j-1} - p_j) \in \mathbb{R}^2$ and $z_\phi := (\phi_{j-1} - \phi_j) \in \mathbb{R}$ are the relative position and bearing of the $(j - 1)$ -th WMR from the j -th WMR expressed in the j -th WMR frame $\{\mathcal{G}_j\}$, and $n_{p_j} \in \mathbb{R}^2$ and $n_{\phi_j} \in \mathbb{R}$ are the zero mean, white Gaussian noise of the camera measurement. Then the pose measurement of the j -th WMR expressed in $\{\mathcal{O}\}$ is given by

$$z_{j,\text{pose}} = \begin{pmatrix} p_{j-1} \\ \phi_{j-1} \end{pmatrix} - \begin{pmatrix} R_{\mathcal{G}_j}^{\mathcal{O}}(\hat{\phi}_j)(z_p + n_{p_j}) \\ z_\phi + n_{\phi_j} \end{pmatrix}$$

where (p_{j-1}, ϕ_{j-1}) is the pose of the fore-running WMR (to be received from the communication). The measurement output can then be rewritten for the error state

s.t.,

$$\tilde{z}_{j,\text{pose}} = \begin{pmatrix} \tilde{p}_{j-1} \\ \tilde{\phi}_{j-1} \end{pmatrix} - \begin{pmatrix} R_{\mathcal{G}_j}^{\mathcal{O}}(\hat{\phi}_j)n_{p_j} \\ n_{\phi_j} \end{pmatrix} = \underbrace{\begin{bmatrix} I_2 & 0_{2 \times 2} & 0_{2 \times 1} & 0_{2 \times 3} \\ 0_{1 \times 2} & 0_{1 \times 2} & 1 & 0_{1 \times 3} \end{bmatrix}}_{=:H_j} \tilde{\chi}_j - \begin{pmatrix} R_{\mathcal{G}_j}^{\mathcal{O}}(\hat{\phi}_j(t))n_{p_j} \\ n_{\phi_j} \end{pmatrix}$$

with its measurement covariance given by

$$R_j := E[\tilde{z}_{j,\text{pose}}\tilde{z}_{j,\text{pose}}^T] = \begin{bmatrix} P_{pp}^{\chi_{j-1}} + R_{\mathcal{G}_j}^{\mathcal{O}}(\hat{\phi}_j)R_{p_j}(R_{\mathcal{G}_j}^{\mathcal{O}}(\hat{\phi}_j))^T & P_{p\phi}^{\chi_{j-1}} \\ P_{\phi p}^{\chi_{j-1}} & P_{\phi\phi}^{\chi_{j-1}} + R_{\phi_j} \end{bmatrix}$$

where $(P_{pp}^{\chi_{j-1}}, P_{p\phi}^{\chi_{j-1}}, P_{\phi p}^{\chi_{j-1}}, P_{\phi\phi}^{\chi_{j-1}})$ are the covariance of the $(j-1)$ -th WMR pose estimate (received from the communication), and $R_{p_j} := E[n_{p_j}n_{p_j}^T]$ and $R_{\phi_j} := E[n_{\phi_j}n_{\phi_j}^T]$ are the covariance of the relative position and bearing measurements obtained from the monocular camera, respectively. When the measurement is received, we can then update the state and covariance of the error state EKF of the j -th WMR as done in (3.23) and (3.24). The covariance $P_{k+1|k+1}^{\chi_j}$ plays a crucial role for the predictive display developed in Sec. 3.3 via its propagation through the kinematics of the WMR and their communication.

3.3 Predictive Display for Distributed Robots Teleoperation

Even if the n -WMRs is reduced to the (familiar) n -trailer platoon by the distributed control of Sec. 3.1, it is still difficult for typical users to tele-navigate this platoon to wiggle through an obstacle-laden environment, as this platoon can exhibit complex internal serpentine articulation, particularly when it experiences a large curvature change. See Fig. 3-4. To assist a remote user to overcome this difficulty, here, we propose a novel *predictive display*, which, by providing the user with the estimated current and predicted future pose information of each WMR along with the possibility of collision, can significantly enhance the user tele-driving performance while

substantially reducing their cognitive loads as manifested by the human subject study in Sec. 3.4.4. Into this predictive display, we also fully incorporate the uncertainty inherent to the distributed robots with the sensing, computation and communication distribution, that is, 1) local pose estimation uncertainty of each WMR starting from that of the leader WMR with the relative pose measurement uncertainty accumulated downstream to the last WMR; and 2) current pose estimation uncertainty of each WMR stemming from the uncertainty of their motions during the transmission delay accumulated upstream to the leader WMR.

To address this complex platoon motion and the distribution-inherent uncertainty, here, we design our predictive display to be composed of the following two stages: 1) *estimation propagation stage*, where the (old) pose estimate of each WMR, received at the current time t_k , is propagated through their transmission delay, so that we can probabilistically estimate its pose at the current time t_k with the associated uncertainty; and 2) *prediction propagation stage*, where the estimated current pose of each WMR at t_k , obtained via the above estimation propagation, is forward-propagated with the current user command so that we can predict the future course of the platoon motion over the prediction time horizon. See Fig. 3-5.

For this, we assume that all the delays (e.g., processing, data conversion, etc.) are lumped into the transmission delay, which is still small enough as compared to the WMR speed (for the distributed control (3.12)-(3.13) to properly work) and also can be made constant with some suitable buffering algorithm. Note that this assumption can easily be granted, at least approximately, if the communication rate is much faster than the WMR speed with negligible data loss rate. This is in fact true for our experimental setup in Sec. 3.4, where all the estimation, control and communication run at 250Hz with near-zero data loss, which is much faster than the WMR operation speed ($\leq 0.5\text{m/s}$). Thus, below, we assume the transmission delay and the computation time be the same (i.e., $t_{k+1} - t_k = 4\text{ms}$ for the setup in Sec. 3.4). Of course, the below derivation can be easily extended when the transmission delay is constant, yet, longer than the computation time. We also assume the LiDAR-SLAM map uncertainty be much less than that of the pose estimation of each WMR,

implying that, for collision detection, we should consider the uncertainty only of the pose estimate of the WMRs.

3.3.1 Estimation Propagation

Note that the pose information of the j -th WMR received at the current time t_k by the MCS (main control station) is given by

$$\hat{q}_{j,k-j} \approx \mathcal{N}(\bar{q}_{j,k-j}, P_{j,k-j})$$

i.e., the estimated state $\hat{q}_j(t_{k-j})$ computed via the EKF-sensor fusion by the j -th WMR and transmitted via the j -hops peer-to-peer communication, first to the $(j-1)$ -th WMR and all the way to the leader WMR and the MCS. Following the EKF sensor fusion of Sec. 3.2, this estimated state $\hat{q}_{j,k-j}$ is characterized by Gaussian distribution with the mean $\bar{q}_{j,k-j}$ and the covariance $P_{j,k-j}$. Given this “delayed” information, we then attempt to estimate the pose of the WMRs at the current time t_k by using the unscented transformation as follows.

Let us start with the leader WMR, from which, at the time k , the MCS receives its estimated pose

$$\hat{q}_{1,k-1} \approx \mathcal{N}(\bar{q}_{1,k-1}, P_{1,k-1})$$

which is assumed to be Gaussian as above. During the interval $[t_{k-1}, t_k)$, the control input for the leader WMR is simply given by $(v_{1,k-1}, w_{1,k-1})$, which is directly received from the MCS. We then use the following equation to estimate $\hat{q}_{1,k}$:

$$\hat{q}_{1,k} = \hat{q}_{1,k-1} + dt \cdot \underbrace{\begin{bmatrix} c \hat{\phi}_{1,k-1} & 0 \\ s \hat{\phi}_{1,k-1} & 0 \\ 0 & 1 \end{bmatrix}}_{=: A(\hat{q}_{1,k-1})} \begin{pmatrix} v_{1,k-1} \\ w_{1,k-1} \end{pmatrix} \quad (3.25)$$

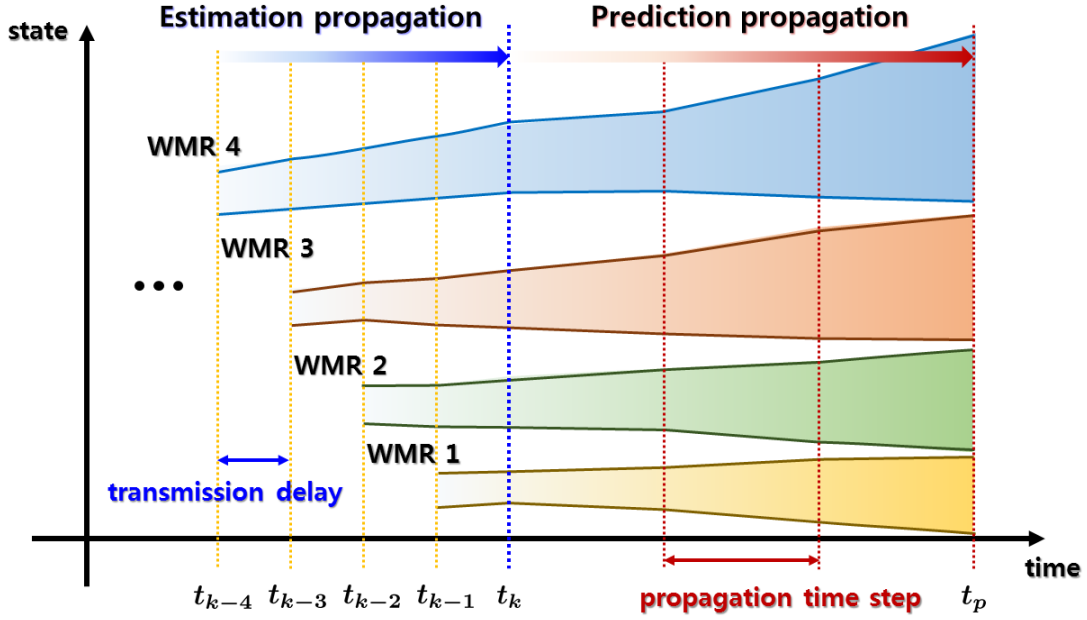


Figure 3-5: Predictive display consists of the two propagation stages: 1) estimation propagation stage to estimate the pose of each WMR at the current time from its reception with the transmission delay; and 2) prediction propagation stage to predict the future course of platoon motion over prediction time horizon via forward propagation.

which can be written by the following nonlinear map

$$\hat{q}_{1,k} = g(\hat{q}_{1,k-1}, v_{1,k-1}, w_{1,k-1})$$

Here, note that, via this nonlinear map, the random variable $\hat{q}_{1,k-1}$ propagates to another random variable $\hat{q}_{1,k}$. This can in fact be computed by using unscented transformation (UT) s.t.,

$$\hat{q}_{1,k}^{ut} := \text{UT}_{g,v_{1,k-1},w_{1,k-1}}(\hat{q}_{1,k-1}) \approx \mathcal{N}(\bar{q}_{1,k}^{ut}, P_{1,k}^{ut})$$

where $\text{UT}_{g,\star}$ is the unscented transformation via the nonlinear map $g(\cdot, \star)$.

Let us then move on to the second WMR, for which the MCS receives its estimated pose s.t.,

$$\hat{q}_{2,k-2} \approx \mathcal{N}(\bar{q}_{2,k-2}, P_{2,k-2})$$

at the time instance t_k . We then first propagate the kinematics of this second WMR from t_{k-2} to t_{k-1} using (3.25). For this, from (3.15), we have

$$\hat{q}_{2,k-1} = \hat{q}_{2,k-2} + dt \cdot A(\hat{q}_{2,k-2}) \begin{pmatrix} v_{1,k-2} \text{c}(\bar{\phi}_{1,k-2} - \bar{\phi}_{2,k-2}) \\ \frac{v_{1,k-2}}{L} \text{s}(\bar{\phi}_{1,k-2} - \bar{\phi}_{2,k-2}) \end{pmatrix}$$

where $\bar{\phi}_{1,k-2}$ is available at the MCS, since it is received from the leader WMR at the (past) time instance t_{k-1} . Then, we can do the “estimation propagation” via the unscented transformation s.t.,

$$\hat{q}_{2,k-1}^{ut} := \text{UT}_{g,v_{1,k-2},\bar{\phi}_{1,2}^{k-2}}(\hat{q}_{2,k-2})$$

where $\bar{\phi}_{1,2}^{k-2} := \bar{\phi}_{1,k-2} - \bar{\phi}_{2,k-2}$. To estimate-propagate from $k-1$ to k , we also use:

$$\hat{q}_{2,k} = \hat{q}_{2,k-1}^{ut} + dt \cdot A(\hat{q}_{2,k-1}^{ut}) \begin{pmatrix} v_{1,k-1} \text{c}(\bar{\phi}_{1,k-1} - \bar{\phi}_{2,k-1}^{ut}) \\ \frac{v_{1,k-1}}{L} \text{s}(\bar{\phi}_{1,k-1} - \bar{\phi}_{2,k-1}^{ut}) \end{pmatrix}$$

from which we estimate $\hat{q}_{2,k}^{ut}$ via the unscented transformation s.t.,

$$\hat{q}_{2,k}^{ut} := \text{UT}_{g,v_{1,k-1},\bar{\phi}_{1,2}^{ut',k-1}}(\hat{q}_{2,k-1}^{ut})$$

where $\bar{\phi}_{1,2}^{ut',k-1} := \bar{\phi}_{1,k-1} - \bar{\phi}_{2,k-1}^{ut}$ with $\bar{\phi}_{1,k-1}$ and $v_{1,k-1}$ available via the communication from the leader WMR to the MCS at t_k .

We can then generalize this for the j -th WMR as the following sequential estimation-propagation procedure: with (3.15),

$$\begin{aligned} \hat{q}_{j,k-j+1}^{ut} &:= \text{UT}_{g,v_{1,k-j},\bar{\phi}_{1,2}^{k-j},\dots,\bar{\phi}_{j-2,j-1}^{k-j},\bar{\phi}_{j-1,j}^{k-j}}(\hat{q}_{j,k-j}^{ut}) \\ \hat{q}_{j,k-j+2}^{ut} &:= \text{UT}_{g,v_{1,k-j+1},\bar{\phi}_{1,2}^{k-j+1},\dots,\bar{\phi}_{j-2,j-1}^{k-j+1},\bar{\phi}_{j-1,j}^{ut',k-j+1}}(\hat{q}_{j,k-j+1}^{ut}) \\ \hat{q}_{j,k-j+3}^{ut} &:= \text{UT}_{g,v_{1,k-j+2},\bar{\phi}_{1,2}^{k-j+2},\dots,\bar{\phi}_{j-2,j-1}^{ut',k-j+2},\bar{\phi}_{j-1,j}^{ut,k-j+2}}(\hat{q}_{j,k-j+2}^{ut}) \\ &\vdots \\ \hat{q}_{j,k}^{ut} &:= \text{UT}_{g,v_{1,k-1},\bar{\phi}_{1,2}^{ut',k-1},\dots,\bar{\phi}_{j-2,j-1}^{ut,k-1},\bar{\phi}_{j-1,j}^{ut,k-1}}(\hat{q}_{j,k-1}^{ut}) \end{aligned} \quad (3.26)$$

where $\bar{\phi}_{j,j+1}^{ut',k} := \bar{\phi}_{j,k}^{ut} - \bar{\phi}_{j+1,k}^{ut}$, and all the terms are available at the time k with the same procedure already done from the leader WMR to the $(j-1)$ -th WMR. Here, note that the nonholonomic passive decomposition and its behavior decomposition (i.e., (3.15)) greatly simplifies this estimation-propagation computation, as it allows us to consider only the collective motion behavior. This computation will be more complex if we use the scheme of [20], which require us to consider both the collective motion and the inter-WMR coordination behaviors.

3.3.2 Prediction Propagation

Once we obtain the current pose estimate $(\hat{q}_{1,k}^{ut}, \hat{q}_{2,k}^{ut}, \dots, \hat{q}_{n,k}^{ut})$ of all the n -WMRs via the estimation propagation, we then perform the “prediction propagation”, that is, predict the pose of each WMR when the same current human command $(v_{1,k}, w_{1,k})$ is kept being applied during the prediction horizon $[t_k, t_{k_p})$. For this, similar as above, we also perform the forward propagation sequentially from the leader WMR to the

n -th WMR and from $[t_k, t_{k+1})$ to $[t_{k_p-1}, t_{k_p})$ using the unscented transformation. More precisely, first, for the leader WMR, we have: using (3.15) with $u_{C_{1,2}} \approx 0$ as assumed above,

$$\begin{aligned}\hat{q}_{1,k+1}^{ut} &:= \text{UT}_{g,v_{1,k},w_{1,k}}(\hat{q}_{1,k}^{ut}) \\ \hat{q}_{1,k+2}^{ut} &:= \text{UT}_{g,v_{1,k},w_{1,k}}(\hat{q}_{1,k+1}^{ut}) \\ &\vdots \\ \hat{q}_{1,k_p}^{ut} &:= \text{UT}_{g,v_{1,k},w_{1,k}}(\hat{q}_{1,k_p-1}^{ut})\end{aligned}$$

On the other hand, for the second WMR, we have: again, with $u_{C_{1,2}} \approx 0$ and (3.16)-(3.17),

$$\begin{aligned}\hat{q}_{2,k+1}^{ut} &:= \text{UT}_{g,v_{1,k},\bar{\phi}_{1,2}^{ut,k}}(\hat{q}_{2,k}^{ut}) \\ \hat{q}_{2,k+2}^{ut} &:= \text{UT}_{g,v_{1,k},\bar{\phi}_{1,2}^{ut,k+1}}(\hat{q}_{2,k+1}^{ut}) \\ &\vdots \\ \hat{q}_{2,k_p}^{ut} &:= \text{UT}_{g,v_{1,k},\bar{\phi}_{1,2}^{ut,k_p-1}}(\hat{q}_{2,k_p-1}^{ut})\end{aligned}$$

and, similarly, for the j -th WMRs,

$$\begin{aligned}\hat{q}_{j,k+1}^{ut} &:= \text{UT}_{g,v_{1,k},\bar{\phi}_{1,2}^{ut,k}, \dots, \bar{\phi}_{j-2,j-1}^{ut,k}, \bar{\phi}_{j-1,j}^{ut,k}}(\hat{q}_{2,k}^{ut}) \\ &\vdots \\ \hat{q}_{j,k_p}^{ut} &:= \text{UT}_{g,v_{1,k},\bar{\phi}_{1,2}^{ut,k_p-1}, \dots, \bar{\phi}_{j-2,j-1}^{ut,k_p-1}, \bar{\phi}_{j-1,j}^{ut,k_p-1}}(\hat{q}_{2,k_p-1}^{ut})\end{aligned}$$

where $\bar{\phi}_{p-1,p}^{ut,k'} := \bar{\phi}_{k',p-1}^{ut} - \bar{\phi}_{k',p}^{ut}$ with $\bar{\phi}_{k',p}^{ut}$ known $\forall k' \in \{k, k+1, \dots, k_p\}$ and $\forall p \in \{1, 2, \dots, j-1\}$ from performing this prediction-propagation sequentially from the leader WMR to the $(j-1)$ -th WMR each for $[t_k, t_{k_p})$. Similar as above, the nonholonomic passive decomposition (i.e., (3.15)) greatly simplifies this prediction-propagation computation as well, which will be more complex if we use the result of [20], as it requires to include the full kinematics with both the collective motion and the inter-

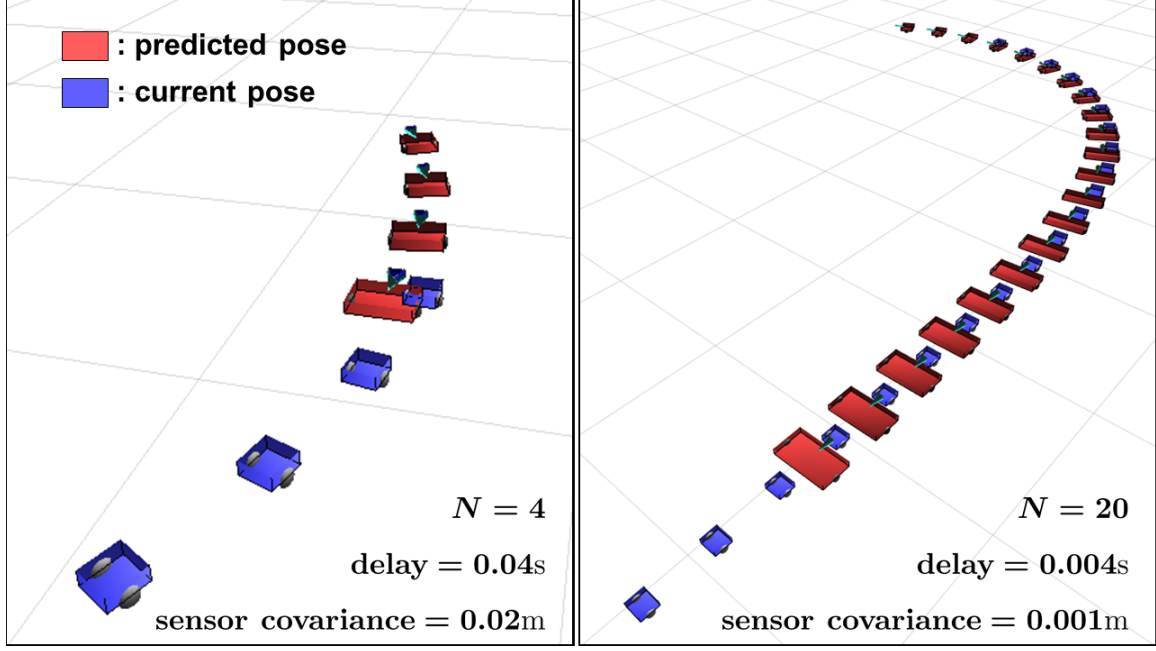


Figure 3-6: Predictive display with estimated current and predicted future poses of WMRs. Uncertainty of pose estimate is denoted by enlarged size of the WMR and the heading angle cone, with their nominal size and center angle determined by the means: 1) uncertainty is the largest for the last WMR (left); and 2) uncertainty still substantial even with fairly precise sensors if the WMRs are many (right).

WMR coordination behaviors.

We then present these estimated current pose $\hat{q}_{j,k}^{ut} \approx \mathcal{N}(\hat{q}_{j,k}^{ut}, P_{j,k}^{ut})$ and the predicted future pose $\hat{q}_{j,k_p}^{ut} \approx \mathcal{N}(\hat{q}_{j,k_p}^{ut}, P_{j,k_p}^{ut})$ to the user by overlaying them on the LiDAR-SLAM map. We also render their position and orientation estimation uncertainties by enlarging the size and the heading angle cone of each WMR, with their center position and angle corresponding to the estimation means and the sweeping size and angle to their covariances. See Fig. 3-2. By seeing this predictive display, human users can predict the procession of the distributed n -WMRs in the obstacle-cluttered environment, examine the likelihood and location of collisions, and adjust their tele-driving command if, e.g., collision is likely to occur. This predictive display turns out crucial here: if it were not for, it is fairly difficult for human users to predict and properly control the motion of the platoon with complex internal serpentine articulation throughout obstacles while avoiding collisions, even if their number is only four - see Sec. 3.4.

Here, note that the uncertainty in both the current and future pose estimation is the largest for the last WMR. This is because the pose estimation uncertainty of the leader WMR is propagated through the platoon with the uncertainty of the relative pose measurements of each WMR all added up on that downstream to the very last WMR. This uncertainty of the last (and each) WMR further increases through the estimation propagation (over the transmission delay) and the prediction propagation (over the prediction time horizon). If this pose uncertainty (e.g., 3σ -value) of the last WMR becomes larger than the minimum inter-obstacle distance on the course of operation, the user cannot rely on the predictive display to tele-drive the platoon any more. Note that this limitation of our predictive display would be severer with 1) less precise onboard sensors; 2) longer transmission delay; 3) larger number of the WMRs; 4) larger size of the WMRs; and 5) narrower gap among the obstacles. Theoretical analysis to elucidate analytical relations among these factors of our predictive display is a topic for future research. See also Fig. 3-6, where some of these relations are shown.

Our proposed predictive display can be applied to general distributed robot systems as well, as it fully incorporates the uncertainty inherently arising from any systems with distributed sensing, computation and communication. Our predictive display framework may also be useful for the problem of driving a platoon of autonomous vehicles with a human driver sitting on the first vehicle while monitoring the state of the vehicles and environment. The idea of predictive display may also be expanded for the general problem of “teleoperation with uncertainty”, by indicating the best possible control direction (e.g., more precise pushing direction for peg-in-hole task) given the sensor uncertainty, parameter estimation error, actuation inaccuracy, etc. All of these constitute interesting topics for ensuing research of our framework presented here.

3.4 Experiments

3.4.1 Test Setup

We implement one “smart” leader WMR and three “simple” follower WMRs as shown in Fig. 3-1. All of them are based on unicycle-type nonholonomic platforms, each with one passive front caster to prevent tipping-over and two rear differential-drive wheels. The wheels are driven by Maxon[®] BLDC motors under velocity control mode with the command received from Arduino Uno MCU (micro-controller unit). The leader WMR has a LiDAR sensor (Hokuyo UTM-30LX-EW, scan rate 40Hz) and an IMU sensor (PhidgetSpatial Precision 3/3/3 IMU, 250Hz, only (x, y) -accelerometer and yaw gyroscope used). The LiDAR-SLAM and all the other computations (i.e, EKF sensor fusion, control computation, predictive display propagation) are run on Intel-NUCi7 on this leader WMR respectively with 40Hz and 250Hz. The three follower WMRs have a front-view monocular web-cam (Logitech C922, 640×480, 30Hz) and the same IMU sensor as the leader WMR. Known patterns similar to [49] are also attached at the rear of each WMR for the relative pose sensing via the monocular camera. The follower WMRs run this relative pose measurement with 30Hz and all the other computations with 250Hz on its Intel-NUCi7.

Robot Operating System (ROS) is deployed as OS of all the WMRs and OpenCV is used for the pattern recognition. We also use RVIZ (3D visualization tool of ROS) to render the LiDAR-SLAM map with 1Hz. On this map, we also render the current and future pose estimates of the WMRs at 50Hz. This predictive display and the LiDAR-SLAM map are rendered on intel-NUCi7 of the leader WMR, which is then remotely accessed by the master PC. Peer-to-peer communication among the WMRs and with the MCS is implemented in UDP protocol with 250Hz. We also attach a CONNEX ProSight HD to the leader WMR as the FPV camera. We also use the Omega3 haptic device as the commanding device with the following position-velocity

mapping:

$$\begin{pmatrix} v_1 \\ w_1 \end{pmatrix} = \begin{pmatrix} \eta_1 \cdot y_h \\ \eta_2 \cdot x_h \end{pmatrix}$$

where $\eta_1, \eta_2 > 0$ are the scaling factors and x_h, y_h are the device position. The desired inter-WMR distance is also set to be: $(L_1, L_2, L_3) = (1, 0.8, 0.8)\text{m}$ - see Fig. 3-2. Haptic feedback of the device is turned off during the experiment - it is used as a commanding device.

3.4.2 Performance Experiment

We first evaluate the performance of our distributed estimation and control with MOCAP (VICON, 240Hz). Due to the limited size of the MOCAP environment, we conduct this experiment only one leader WMR and two follower WMRs. Total ten experiments are performed, five with the circular trajectory and five with the s-shape curve. The results of one trial of those five experiments are shown in Fig. 3-7 and Fig. 3-8.

First, as shown in Fig. 3-7, the RMSE (root mean square error) between the MOCAP data and our estimation data of the leader WMR and the two follower WMRs (for all the ten experiments) are found to be 2.11cm, 2.19cm and 2.56cm for the circular trajectory and 1.86cm, 2.18cm, and 3.32cm for the s-curve trajectory. This level of estimation performance is precise enough for our experiments given the size of the platoon formation (i.e., $(L_1, L_2, L_3) = (1, 0.8, 0.8)\text{m}$). Here, note the effect of downward accumulation of uncertainty as stated in Sec. 3.3.

To evaluate the combined performance of our distributed estimation and control, we also measure the inter-WMR coordination error $\|h_{j,j+1}(t)\|$ as shown in Fig. 3-8. We have similar trend for all the ten experiments as this Fig. 3-8. We then observe that the maximum of this coordination error is less than 4cm, which is again deemed precise enough given the size of the platoon and the environment. This also shows that, thanks to the (distributed) quotient control $u_{C_{j,j+1}}$ (3.8), the inter-WMR coordination

aspect can be maintained fairly well regardless of the collective platoon motion (e.g., tele-driving).

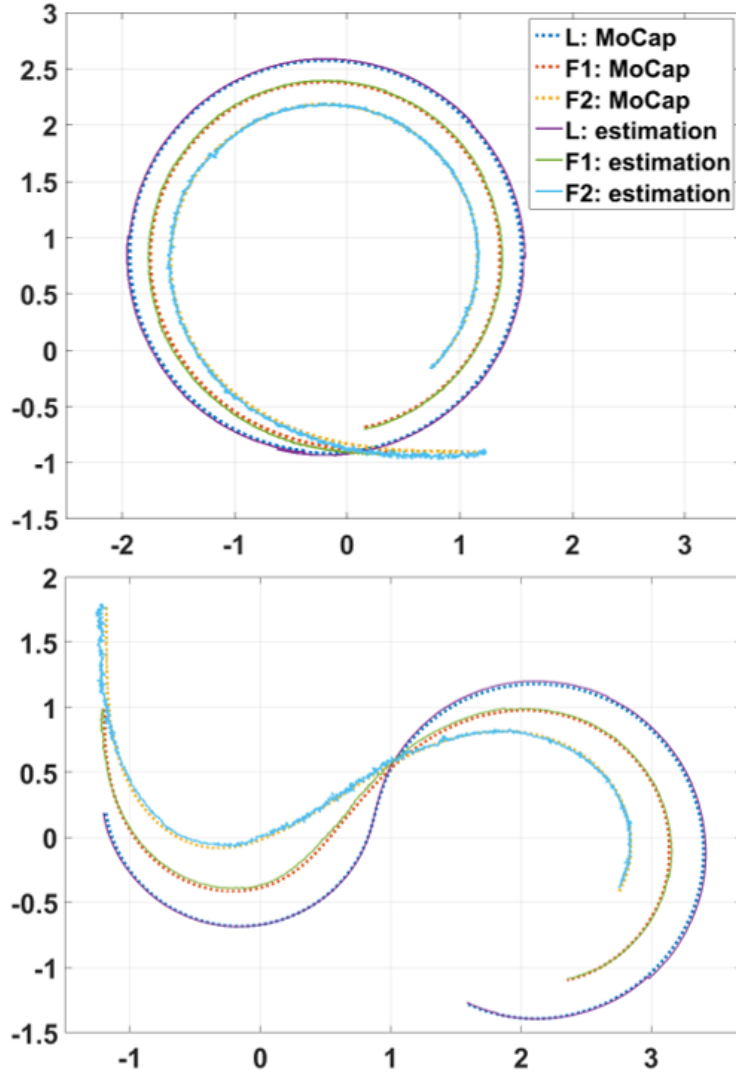


Figure 3-7: Circular and s-shape trajectories of the three WMRs during the performance experiments: dotted lines are the ground truth position measured by MOCAP and solid lines the estimated position computed by the distributed estimation of Sec. 3.2.

3.4.3 Teleoperation Experiment with Predictive Display

We conduct teleoperation experiment with the predictive display and the FPV in a real office environment with no MOCAP. The four WMRs as shown in Fig. 3-1 are used. The environment is shown in Fig. 3-9, consisting of the hall, the office room,

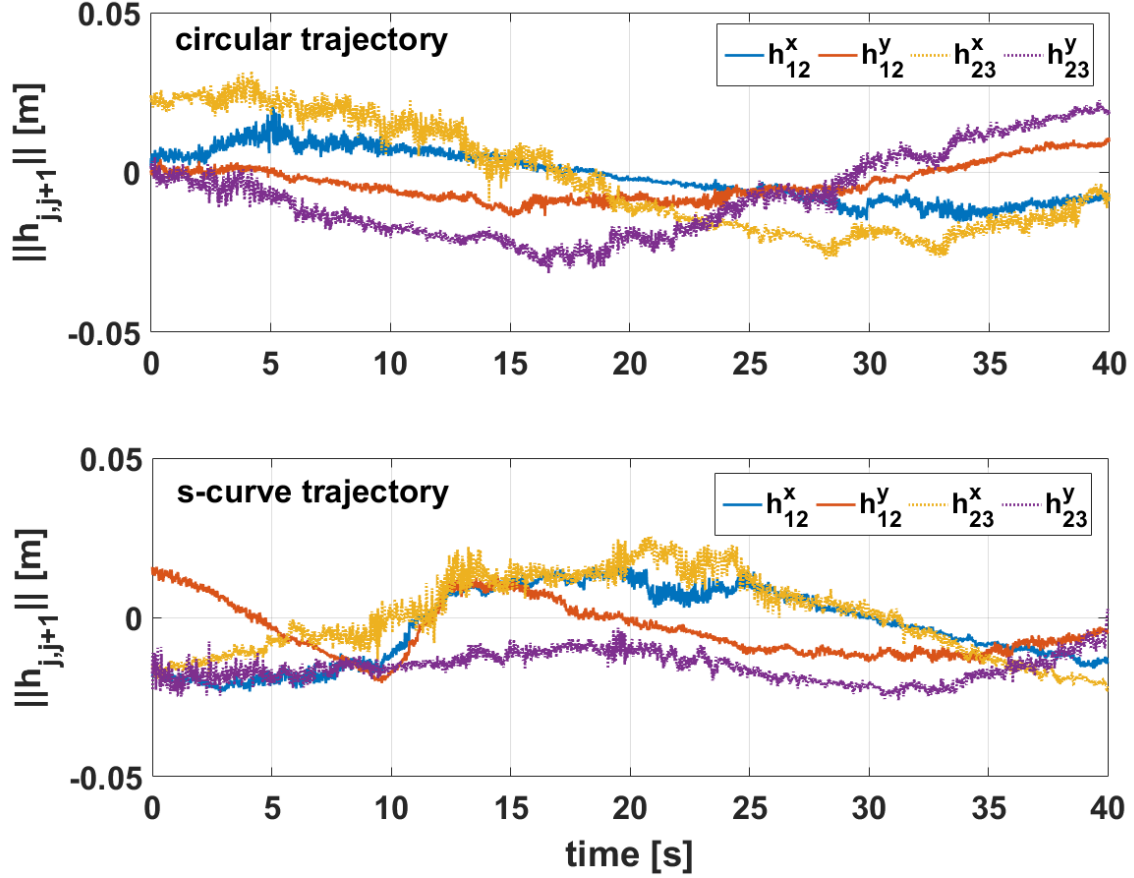


Figure 3-8: Inter-WMR coordination error $\|h_{j,j+1}\|$ among the three WMRs during the performance experiments with the circular and s-shape trajectories.

and the corridor connecting them. The task goal is to check the four markers via the FPV camera: one on the corridor wall and three in the office. For this, a human user tele-drives the platoon starting from the hall, passing the corridor with three obstacles, going around the office room while avoiding a table in the middle of it, and returning to the start point. One obstacle in the corridor is too short for the LiDAR to detect - the user must rely on the FPV camera for this. Collision is prohibited throughout this teleoperation experiment.

The master interface consists of one monitor and one haptic device as depicted in Fig. 3-10. The monitor displays the FPV camera view and the LiDAR-SLAM map. The haptic device is used only as a pointing device with haptic feedback turned off. The predictive display shows the current pose and future pose estimates of all the WMRs as explained in Sec. 3.3. The orientation of these predictive display and

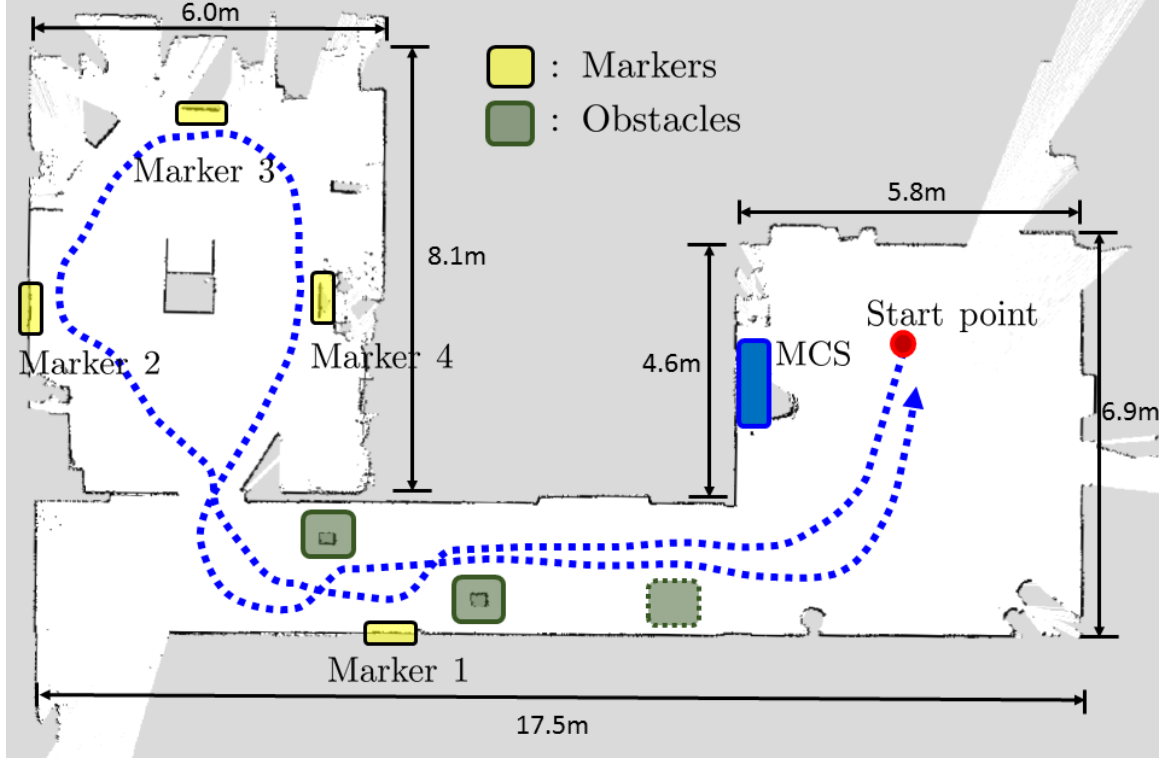


Figure 3-9: The environment map for the teleoperation experiment and human subject study test: yellow boxes indicate four markers that the user should check; the green boxes are obstacles, with the dotted green box a short obstacle that cannot be detected by the LiDAR but should be noticed by the FPV camera. The blue dotted path presents the trajectory of the leader WMR of a successful trial.

LiDAR-SLAM map are also rotated to be consistent with that of the FPV camera view to avoid the user confusion. We scale-up the size of these WMRs in the predictive display according to their uncertainty obtained as explained in Sec. 3.3. For this, we use the 3σ -value of the covariance, which is corresponding to the 99.7% probability. We measure the distance between these “future sized-up” WMRs to the LiDAR-SLAM map, and notify the user of possible (future) collision when any of these distances becomes less than a certain threshold. We do this by overlaying a white circular shade on top of the colliding WMRs. This collision notification is not provided when the future/sized-up WMR hits the regions missing the LiDAR scans, as they may still be traversable. To decide if these “blank” regions are traversable or not, the user instead needs to rely on the FPV camera information. We choose the prediction horizon to be 15 seconds, which is corresponding to 2m distance from the “current” WMRs given

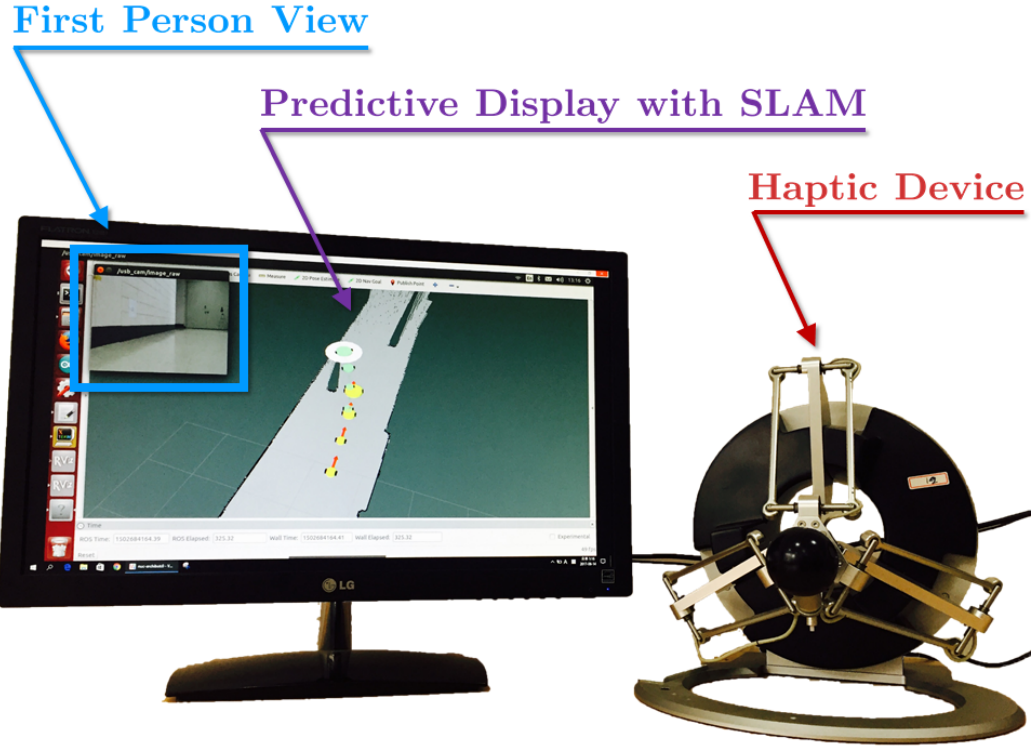


Figure 3-10: Teleoperation master interface consisting of predictive display with LiDAR-SLAM map and FPV camera video-feed, and haptic device (used only as positioning device without haptic feedback).

the average operation speed of about 0.15m/s. This level of prediction horizon turns out to be adequate for our teleoperation. Of course, depending on the complexity of the environment and the driving speed, this value should be adjusted.

The results of this teleoperation experiment are shown in Fig. 3-11. Throughout this teleoperation experiment, we observe that: 1) both the FPV camera and the predictive display with the LiDAR-SLAM information are necessary to successfully complete the teleoperation task, as they provide complementary information (e.g., detecting the short obstacle in the corridor); 2) the predictive display is crucial to complete this teleoperation task, particularly for such challenging operation as navigating through the (narrow) door of the office room from the corridor, which requires a large change of the platoon curvature so that the platoon serpentine motions become difficult to understand and control for the human user; and 3) the platoon of the four nonholonomic WMRs keeps behaving as a 4-trailer system throughout

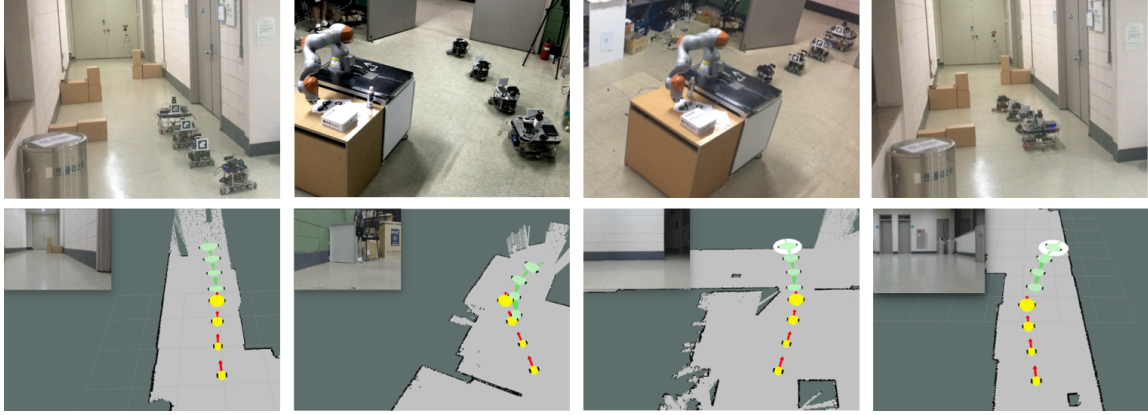


Figure 3-11: Snapshots of the office-corridor teleoperation experiment: (Top row) External camera third person view of the environment with scattered box obstacles and the table in the middle of the office room; (Bottom row) Predictive display with LiDAR-SLAM map, showing the current (solid) and future (opaque) pose estimate of the WMRs and possible collision (white circular shade) along with the FPV camera video-feed.

the teleoperation experiment, even if they are driven by arbitrary human command. For more rigorous justification on the importance of the predictive display, we then perform the human subject study as stated in the next Sec. 3.4.4.

3.4.4 Human Subject Study

To rigorously verify the efficacy of the predictive display, here, we perform human subject study. For this, we use the same setting as the teleoperation experiment of Sec. 3.4.3. Two groups of the subjects are formed: 1) experimental group, where the subjects perform the same teleoperation task twice, first with the predictive display and then without the predictive display; and 2) control group, where the subjects perform the same teleoperation task twice, yet, both with the predictive display. This is to nullify the learning effect, that is, if the performance improvement for the second trial of the experimental group is less than that of the control group, the efficacy of the predictive display can be concluded.

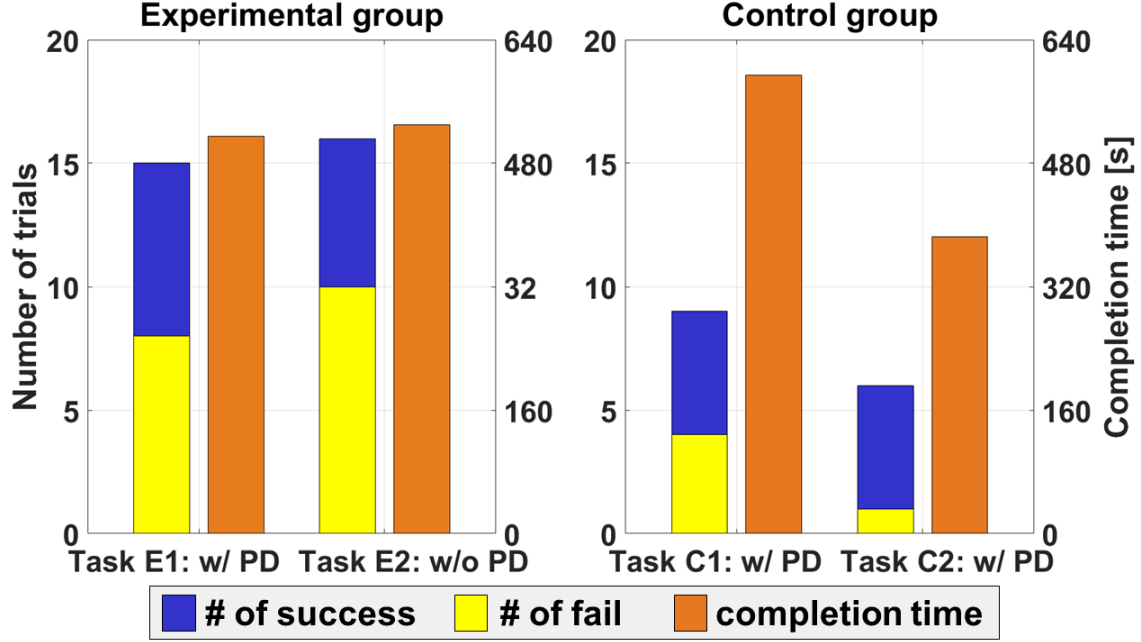


Figure 3-12: Number of successful/failed trials and average completion time across the subjects of each Task for the experimental group (eight subjects) and control group (five subjects).

Participants

Thirteen right-handed subjects (one female) with the age from 21 to 27 participate this study with no known neurological disorders. The experimental group is formed with eight subjects, whereas the control group with five subjects. None of them have contributed to the design or implementation of the experiment. The experiments are conducted in accordance with the requirements of the Helsinki Declaration.

Task

Motivated by the office or factory material transport scenario, we consider the same scenario as for the teleoperation experiment of Sec. 3.4.3. The subjects in the experimental group perform this task with the predictive display (Task E1: w/ PD) and then without predictive display (Task E2: w/o PD); whereas those in the control group perform the same task with the predictive display twice successively (i.e., Task C1: w/ PD, Task C2: w/ PD).

Procedure

First, the supervisor explains each subject of the purpose of the experiment and the system configuration. He also explains them about the behavior of the n -trailer system, i.e., their behavior under the condition of $h_{j,j+1} = 0$ in (3.3). Then, each subject is allowed to play with the test setup as much as they want before performing the actual trials. During this time, the predictive display is turned on. The WMRs are confined within the hall of Fig. 3-9 though. The supervisor also takes each subject briefly walking around the environment, since, without it, it is too difficult for the subjects to perform the task while also constructing the environment information at the same time. Although this provides partial information of the environment, we believe the human subject study here can still clearly manifest the efficacy of the predictive display for the teleoperation as stated below.

All the subjects start the trial with the predictive display (i.e., Task E1: w/ PD or Task C1: w/ PD). If any WMR collides with the obstacles or environment during this trial, the user stops the task, the operation time is recorded, and the subject starts the new trial of the same task all over again from the start point in Fig. 3-9. If one fails three successive trials, that task is aborted and moves to the next task or give the seat to the next subject. When the Task E1 or C1 is completed (or three-trail failed), the subject of the experimental group then moves on to the same task without the predictive display (i.e., Task E2: w/o PD), whereas those in the control group to the same task again with the predictive display (i.e., Task C2: w/ PD). For each Task, the number of failed trials is recorded with that of the successful trial, which is always one. During these experiments, each subject wears earplugs to further reduce the (already fairly small) sound from the experiment. After the two Tasks of each group are finished, each subject is asked to fill in the NASA TLX (Task Load index) type questionnaire.

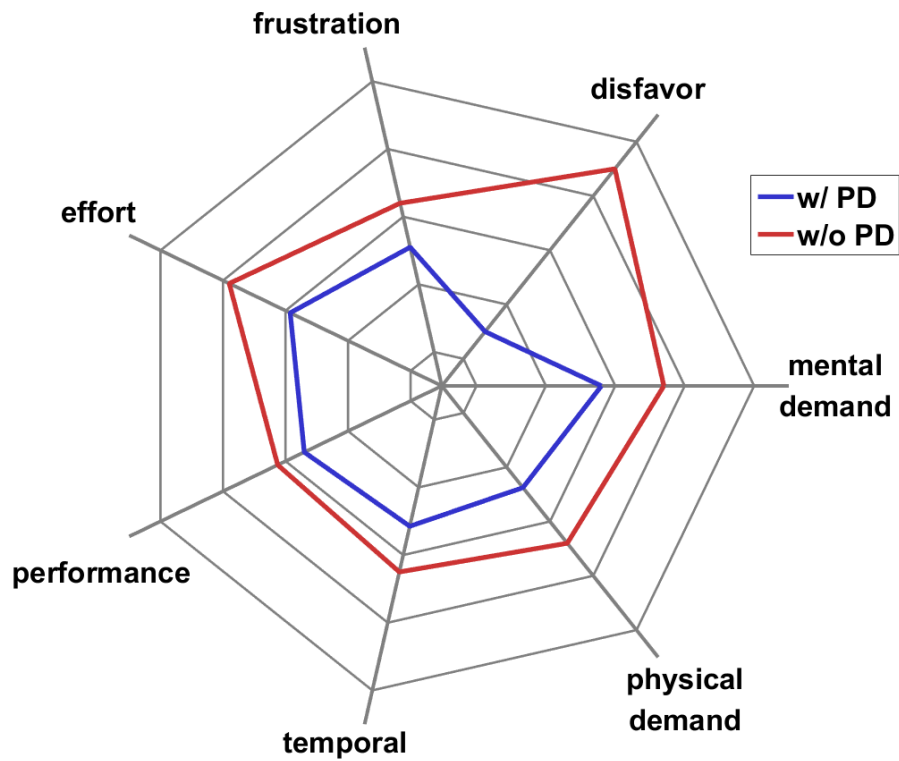


Figure 3-13: NASA TLX questionnaire result and the user disfavor (i.e., 1- preference) rating with and without the predictive display for the human subject study experiments.

Results and Discussion

The results of this human subject study are summarized in Fig. 3-12 and Fig. 3-13. First, note from Fig. 3-12 the substantial reduction of the failed trial ratio from Task E2 to Task C2. Note also from Fig. 3-12 the substantial reduction of the ratio of Task C2 complete time to Task C1 completion time as compared to that of Task E2 to Task E1. These all clearly manifest the importance and efficacy of the predictive display.

On the other hand, the NASA-TLX result of Fig. 3-13 shows that, on top of the objective performance improvement of Fig. 3-12, the predictive display also enhances the tele-driving system from the subjective “feeling” as well, while also substantially reducing cognitive loading of the human users. The predictive display is also advocated by nearly all the subjects (except one).

Chapter 4

Semi-Autonomous Teleoperation of Stage-Manipulator System on Flexible Vertical Beam

4.1 System Modeling

To model the flexible beam, we utilize Euler-Bernoulli theory with a modal approximation. Then, we rigorously consider the boundary condition of our system configuration to calculate the natural frequency of the assumed finite modes. The mode shapes are considered as eigenfunctions of the flexible beam so that the orthogonality condition between the mode shapes is enforced to specifically determine the mode shapes. Finally, we use Euler-Lagrange equations to derive the dynamics model of the whole system with the calculated mode shapes.

4.1.1 System Description

Let us define following six frames (See. Fig. 4-1): ground fixed frame $\{\mathcal{O}\}$ which is located in the bottom of the beam, the flexible moving frame $\{\mathcal{B}\}$ which is attached at the end of the beam, body frame of the linear stage $\{\mathcal{S}\}$, and body frame of each joint $\{1\}$, $\{2\}$, and $\{3\}$. The position of the end of the beam expressed in $\{\mathcal{O}\}$ are

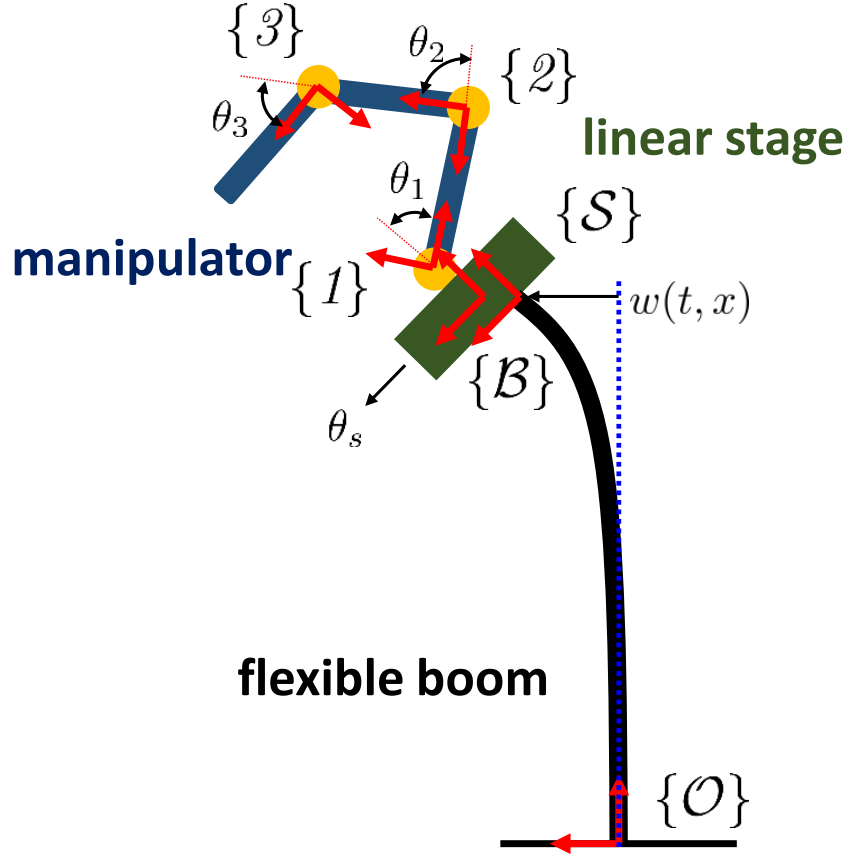


Figure 4-1: Test-bed model of slave robot of telerobotics project.

denoted by $p_{ob}^o \in \mathfrak{R}^2$.

Since the deflection of the beam is assumed to be small, the deflection and rotation of the beam can be written by

$$p_{ob}^o \approx \begin{bmatrix} l_b \\ w(l_b, t) \end{bmatrix} \in \mathfrak{R}^2, \quad \theta_b = \text{atan} \left(\frac{dw}{dx} \right) \approx \left(\frac{dw}{dx} \right) \in \mathfrak{R}$$

where $w(l_b, t)$ is the deflection at the position l_b along x -axis at time t and l_b is the length of the beam. Here, note that the x -axis is the upper direction to define the direction of the beam as x -axis. Among any two of these frames, we can then define p_{ab}^a is the position vector of the origin of $\{\mathcal{B}\}$ from the origin of $\{\mathcal{A}\}$ expressed in $\{\mathcal{A}\}$. If \mathcal{A} and \mathcal{B} are same, $p_{ab}^a = [0; 0]$.

4.1.2 Assumed Mode Shapes

Based on Euler-Bernoulli theory, govern equation of the lateral vibrational motion of beams and general solutions [50] are given by

$$\rho A \frac{\partial^2 w}{\partial t^2} + \frac{\partial^2}{\partial x^2} \left(EI(x) \frac{\partial^2 w}{\partial x^2} \right) = 0 \quad (4.1)$$

$$w(x, t) = \sum_{i=1}^{\infty} \phi_i(x) \approx \sum_{i=1}^{n_d} \phi_i(x) \delta_i(t) \delta_i(t) \quad (4.2)$$

where ρ is density, A is intersection area, E is Young's modulus, $I(x)$ is second moment of inertia of the beam, and n_d is the the number of the assumed modes. For simplicity, we assume that the beam has all parameters of the beam are constant. The second equation presents separated variable solution where $\phi_i(x)$ is i -th time-invariant mode shape and $\delta_i(t)$ is time-varying i -th mode's amplitude. In this thesis, we define $n_d = 3$ because we empirically find that the three modes are sufficient approximation of the deformation of our system because of the high-payload at the tip, i.e. the stage-manipulator system.

It is well-known the explicit form of i -th mode shape is

$$\phi_i = C_1 \sin \beta_i x + C_2 \cos \beta_i x + C_3 \sinh \beta_i x + C_4 \cosh \beta_i x$$

where $\beta_i^4 = \omega_{\delta_i}^2 \rho A / EI$, ω_{δ_i} is natural frequency of i -th mode, and each C_i is a coefficient. Note that the mode shapes are time-invariant and determined by boundary conditions, i.e. the structure and configurations of whole system. In order to obtain the coefficients of the mode shapes ϕ_i , we use the boundary conditions which are 1) clamped ground-end and 2) lumped mass/inertia tip-end conditions.

4.1.3 Exact Solution under Given Boundary Conditions

Reasonable boundary conditions for our system are 1) clamped ground and 2) point force/torque at end (i.e. lumped mass and inertia at the tip). 'Clamped' boundary condition is the assumption that there is fixed deflection and orientation (i.e. slope).

This condition can be represented by

$$w(0, t) = \phi(0)\delta(t) = 0 \rightarrow C_4 + C_6 = 0 \quad (4.3)$$

$$\theta_b|_{x=0} \approx \frac{dw}{dx}(0, t) = \phi(0)'\delta(t) = 0 \rightarrow C_3 + C_5 = 0 \quad (4.4)$$

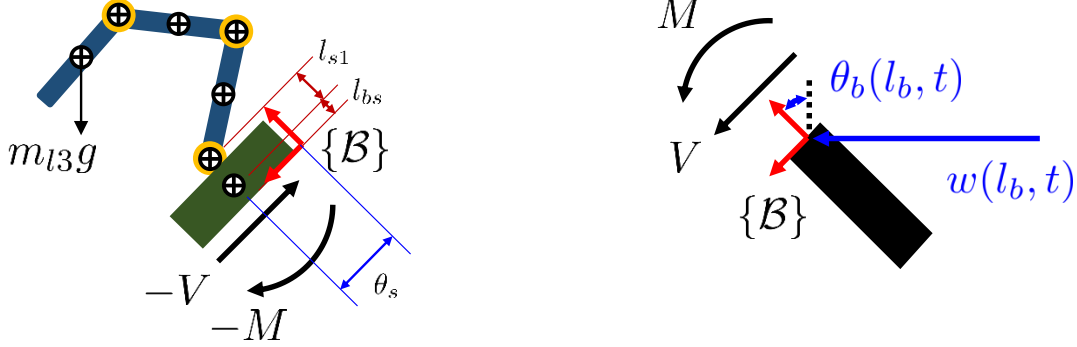


Figure 4-2: Lumped masses boundary conditions at the end of the boom

Lumped mass boundary condition represents the balance condition of force and torque at the tip of the boom. First of all, the moment balance equation can be expressed by

$$\begin{aligned} M(x = l_b) &= EI \frac{d^2 w}{dx^2} \\ &= - \underbrace{\left(I_s + \sum_{i=1}^3 (I_i + I_{l_i}) \right)}_{:=I_0} \ddot{\theta}_b \\ &\quad - \ddot{w} \left(m_s [p_{bs}^o]_1 + m_1 [p_{b1}^o]_1 + m_{l_1} [p_{bl_1}^o]_1 + m_2 [p_{b2}^o]_1 + m_{l_2} [p_{bl_2}^o]_1 + m_3 [p_{b3}^o]_1 + m_{l_3} [p_{bl_3}^o]_1 \right) \\ &\quad - g \left(m_s [p_{bs}^o]_2 + m_1 [p_{b1}^o]_2 + m_{l_1} [p_{bl_1}^o]_2 + m_2 [p_{b2}^o]_2 + m_{l_2} [p_{bl_2}^o]_2 + m_3 [p_{b3}^o]_2 + m_{l_3} [p_{bl_3}^o]_2 \right) \\ &= -I_0 \ddot{\theta}_b - M_d \ddot{w} - M_g g \end{aligned}$$

where $g = 9.81 \text{ m/s}^2$ is gravitational acceleration, $[\star]_2$ is the y -axis component of the vector $\star \in \mathfrak{R}^2$, $M_d = \sum_{i=s}^{l_3} m_i [p_{bi}^o]_1$, and $M_g = \sum_{i=s}^{l_3} m_i [p_{bi}^o]_2$

Next, the shear force (y -direction in $\{\mathcal{O}\}$) at the tip of the boom can be written

by

$$\begin{aligned}
V(x = l_b) &= -\frac{dM}{dx} = -EI \frac{d^3 w}{dx^3} \\
&= -\underbrace{\left(m_s + \sum_{i=1}^3 (m_i + m_{l_i}) \right)}_{:=m_0} \ddot{w} \\
&\quad - \ddot{\theta}_b \left(m_s [p_{bs}^o]_1 + m_1 [p_{b1}^o]_1 + m_{l_1} [p_{bl_1}^o]_1 + m_2 [p_{b2}^o]_1 + m_{l_2} [p_{bl_2}^o]_1 + m_3 [p_{b3}^o]_1 + m_{l_3} [p_{bl_3}^o]_1 \right) \\
&= -m_0 \ddot{w} - M_d \ddot{\theta}_b
\end{aligned}$$

where M_d accounts for the contributions of masses of distal links, i.e., noncollocated at the-end of the boom, weighted by the relative distance from y axis in $\{\mathcal{B}\}$, (shearing axis at the end of the boom). Incidentally, these contributions are often not included in mode shape analyses [51].

Therefore, we have two more boundary conditions: 1) moment balance condition; and 2) shear force balance condition. Furthermore, we can obtain two equations of spatial solutions by using the fact of $\ddot{\delta}(t) = -\omega^2 \delta(t)$.

$$EI \frac{\partial^2 w}{\partial x^2}(l_b, t) = -I_0 \ddot{\theta}_b - M_d \ddot{w}(l_b, t) - M_g g \quad (4.5)$$

$$\Rightarrow [EI \phi''(l_b) - \omega^2 (I_0 \phi'(l_b) + M_d \phi(l_b))] \delta(t) = -M_g g$$

$$EI \frac{\partial^3 w}{\partial x^3}(l_b, t) = m_0 \ddot{w}(l_b, t) + M_d \ddot{\theta}_b \quad (4.6)$$

$$\Rightarrow [EI \phi'''(l_b) + \omega^2 (m_0 \phi(l_b) + M_d \phi'(l_b))] \delta(t) = 0$$

Since the first boundary condition (4.5) is nonhomogeneous, we cannot use modal analysis for the response. In [50], the authors said that one way to solve the problem which consists of homogeneous dynamics, one homogeneous boundary condition, and the other nonhomogeneous boundary condition is to transforming it into a problem defined by a nonhomogeneous dynamics and homogeneous boundary conditions. This means that we can use the motion of *forced vibration* of the beam' to deal with the concentrated force or moment at the tip. Thus, from here, let me deploy the differential equations of forced vibration.

Forced Vibration of Beams

Even if the nonhomogeneity factor $M_g g$ is concentrated moment at the tip, let us consider the moment is distributed force over a very small segment of the boom given by $l_b^- < x < l_b$ where l_b^- denotes a point to the immediate left of $x = l_b$ [52] and then, we can express the moment as

$$f(x, t) = M_g(t)g\text{Dirac}(x - l_b), \quad 0 < x < l_b$$

where $\text{Dirac}(x)$ is the Dirac delta function. The moment of force caused by the gravity of the rigid system only acts on the boom regardless of the vibration. Other moment and shear force terms such as $I_0\ddot{\theta}_b$, $M_d\ddot{w}(l_b, t)$, $M_{gx}g\theta_b$, $m_0\ddot{w}(l_b, t)$, and $M_d\ddot{\theta}_b$ can be considered in the boundary conditions (4.5) and (4.6) because they do not violate the homogeneity property and act only in the vibration.

The differential equation of the vibration of forced beam is given by

$$\rho A \frac{\partial^2 w}{\partial t^2} + \frac{\partial^2}{\partial x^2} \left(EI(x) \frac{\partial^2 w}{\partial x^2} \right) = f(x, t) \quad (4.7)$$

with the boundary conditions

$$\text{at } x = 0, \quad w(0, t) = \phi(0)\delta(t) = 0 \quad \text{and} \quad \theta_b|_{x=0} = \phi(0)'\delta(t) = 0 \quad (4.8)$$

$$\text{at } x = l_b, \quad \begin{cases} EI \frac{\partial^2 w}{\partial x^2}(l_b, t) = -I_0\ddot{\theta}_b - M_d\ddot{w}(l_b, t) \\ EI \frac{\partial^3 w}{\partial x^3}(l_b, t) = m_0\ddot{w}(l_b, t) + M_d\ddot{\theta}_b \end{cases} \quad (4.9)$$

Since we assume that the external force is applied to the segment $l_b^- < x < l_b$, the vibration of the boom at $x = l_b$ is given by unforced vibration in (4.1). Therefore, when we find the natural frequencies we can just consider the free vibration in (4.1). Exactly, once we obtain the natural modes, we must solve the temporal solution $\delta(t)$ which is excited by the external force under the forced vibration dynamics (4.7) and given initial conditions [50]. However, in our case, we will determine the amplitude $\delta(t)$ in the complete dynamics which will be derived later. As a result, we ignore the

moment generated by the gravity of rigid system by deploying the forced vibration.

The above approach could be thought as an approximation of natural modes. To get exact natural modes, we need to consider complete dynamics which will be derived later and more exact boundary conditions with consideration of reactive force/moment of actuations $\tau_i(t)$ at the tip. In this thesis, we will derive the natural modes under the above consideration with non-zero M_d and a part of gravity effect $M_{gx}g\theta_b$ which depends on the motion of the boom.

Orthogonality and Normalization of Natural Modes

In this subsection, we will see the orthogonality property between each natural mode. We assume that the solution of the motion can be written by $w(x, t) = \sum_{i=1}^{\infty} \phi_i(x)\delta_i(t)$. Then, from the equation (4.2),

$$\frac{d^2}{dx^2} \left(EI(x) \frac{d^2 \phi_r}{dx^2}(x) \right) = \rho A \omega_r^2 \phi_r(x), \quad r = 1, 2, \dots$$

where E and I are constant. Next, we multiply $\phi_s(x)$ to the both side and integrate over the length of the boom.

$$\int_0^{l_b} \phi_s(x) \frac{d^2}{dx^2} \left(EI(x) \frac{d^2 \phi_r}{dx^2}(x) \right) dx = \omega_r^2 \int_0^{l_b} \rho A \phi_s(x) \phi_r(x) dx \quad (4.10)$$

By using integration by parts, the left hand side can be rewritten by

$$\begin{aligned} \text{RHS} &= \phi_s(x) \frac{d}{dx} \left(EI(x) \frac{d^2 \phi_r}{dx^2}(x) \right) \Big|_0^{l_b} - \int_0^{l_b} \frac{d\phi_s}{dx}(x) \frac{d}{dx} \left(EI(x) \frac{d^2 \phi_r}{dx^2}(x) \right) dx \\ &= \phi_s(x) \frac{d}{dx} \left(EI(x) \frac{d^2 \phi_r}{dx^2}(x) \right) \Big|_0^{l_b} - \frac{d\phi_s}{dx}(x) EI(x) \frac{d^2 \phi_r}{dx^2}(x) \Big|_0^{l_b} + \int_0^{l_b} \frac{d^2 \phi_s}{dx^2}(x) EI(x) \frac{d^2 \phi_r}{dx^2}(x) dx \end{aligned}$$

For simplicity, let us use the notation primes to denote the differentiation, i.e. $d\phi_r(x)/dx|_{x=l_b} = \phi'_r(l_b)$. In addition, if E and I are constant,

$$\text{RHS} = EI \left[\phi_s(l_b) \phi_r'''(l_b) - \phi_s'(l_b) \phi_r''(l_b) + \int_0^{l_b} \phi_s''(x) \phi_r''(x) dx \right]$$

Here, we use the boundary condition at the clamped end, thus $\phi_i(0) = d\phi_i(0)/dx = 0$. The first and second terms in the RHS in the above equation can be replaced with the boundary conditions of moment and shear force at the tip of the boom in (4.5) and (4.6).

$$\begin{aligned} EI\phi_r'''(l_b) &= -\omega_r^2 [m_0\phi_r(l_b) + M_d\phi_r'(l_b)] \triangleq -\omega_r^2\mathcal{H}_1 \\ EI\phi_r''(l_b) &= \omega_r^2 [I_0\phi_r'(l_b) + M_d\phi_r(l_b)] \triangleq \omega_r^2\mathcal{H}_2 \end{aligned}$$

Finally, we can rewrite the equation (4.10) as follow

$$\omega_r^2 \int_0^{l_b} \rho A \phi_s(x) \phi_r(x) dx = -\phi_s(l_b) (\omega_r^2 \mathcal{H}_1) - \phi_s'(l_b) (\omega_r^2 \mathcal{H}_2) + EI \int_0^{l_b} \phi_s''(x) \phi_r''(x) dx$$

Again, we can explicitly rewrite

$$\begin{aligned} \omega_r^2 \int_0^{l_b} \rho A \phi_s(x) \phi_r(x) dx &= -\omega_r^2 \phi_s(l_b) [m_0\phi_r(l_b) + M_d\phi_r'(l_b)] - \omega_r^2 \phi_s'(l_b) [I_0\phi_r'(l_b) + M_d\phi_r(l_b)] \\ &\quad + EI \int_0^{l_b} \phi_s''(x) \phi_r''(x) dx \end{aligned} \quad (4.11)$$

Through the same steps, we can easily change subscript r and s and obtain the following equation

$$\begin{aligned} \omega_s^2 \int_0^{l_b} \rho A \phi_r(x) \phi_s(x) dx &= -\omega_s^2 \phi_r(l_b) [m_0\phi_s(l_b) + M_d\phi_s'(l_b)] - \omega_s^2 \phi_r'(l_b) [I_0\phi_s'(l_b) + M_d\phi_s(l_b)] \\ &\quad + EI \int_0^{l_b} \phi_s''(x) \phi_r''(x) dx \end{aligned} \quad (4.12)$$

Since all terms are scalar, all multiplications are commutative. If we subtract (4.11) from (4.12), then the result equation is

$$\begin{aligned} (\omega_r^2 - \omega_s^2) \int_0^{l_b} \rho A \phi_s(x) \phi_r(x) dx &= \\ &\quad - (\omega_r^2 - \omega_s^2) \left[m_0\phi_s(l_b)\phi_r(l_b) + I_0\phi_s'(l_b)\phi_r'(l_b) + M_d \frac{d}{dx} (\phi_s(x)\phi_r(x)) \Big|_{x=l_b} \right] \end{aligned}$$

Thus, we can obtain one condition such that

$$\int_0^{l_b} \rho A \phi_s(x) \phi_r(x) dx + \left[m_0 \phi_s(l_b) \phi_r(l_b) + I_0 \phi'_s(l_b) \phi'_r(l_b) + M_d \frac{d}{dx} (\phi_s(x) \phi_r(x)) \right] \Big|_{x=l_b} = 0$$

Finally, once one apply the above condition to (4.11) or (4.12), the orthogonality condition of the natural modes is

$$\int_0^{l_b} \frac{d^2 \phi_r}{dx^2}(x) \frac{d^2 \phi_s}{dx^2}(x) dx = 0, \quad r \neq s \quad (4.13)$$

This term implies the effective stiffness, consequently, there is no coupled spring between each mode. This orthogonal property leads to a result of diagonal matrix of structural spring term in dynamics in (4.18). Furthermore, if there is no lumped mass and inertia, i.e. $m_0 = I_0 = M_d = 0$, then another orthogonal property turns up, that is $\int \rho A \phi_r(x) \phi_s(x) dx = 0$. This means that there is no coupling in inertia matrix because the integral terms of $\phi_i(x)$ appear in kinetic energy of the boom.

Furthermore, if $r = s$,

$$\omega_r^2 \underbrace{\left(\int_0^{l_b} \rho A \phi_r(x)^2 dx + m_0 \phi_r(l_b)^2 + I_0 \phi'_r(l_b)^2 + 2M_d \phi_r(l_b) \phi'_r(l_b) \right)}_{:=\mathcal{M}} = EI \int_0^{l_b} (\phi_r''(x))^2 dx$$

We have five unknowns (four coefficients of mode shape and natural frequency) but four boundary condition. This means that we can calculate the scaling factor rather than exact mode shape, thus, normalization is usually performed. We can normalize the natural mode to find $\phi_r(x)$ such that $\mathcal{M} = 1$, then

$$\int_0^{l_b} (\phi_r''(x))^2 dx = \omega_r^2 / EI \quad (4.14)$$

I checked the properties of orthogonality (4.13) and normalization (4.14). In my simulation, due to numerical error, the terms in (4.13) and difference between RHS and LHS in (4.14) are order of $10^{-12} \sim 10^{-15}$.

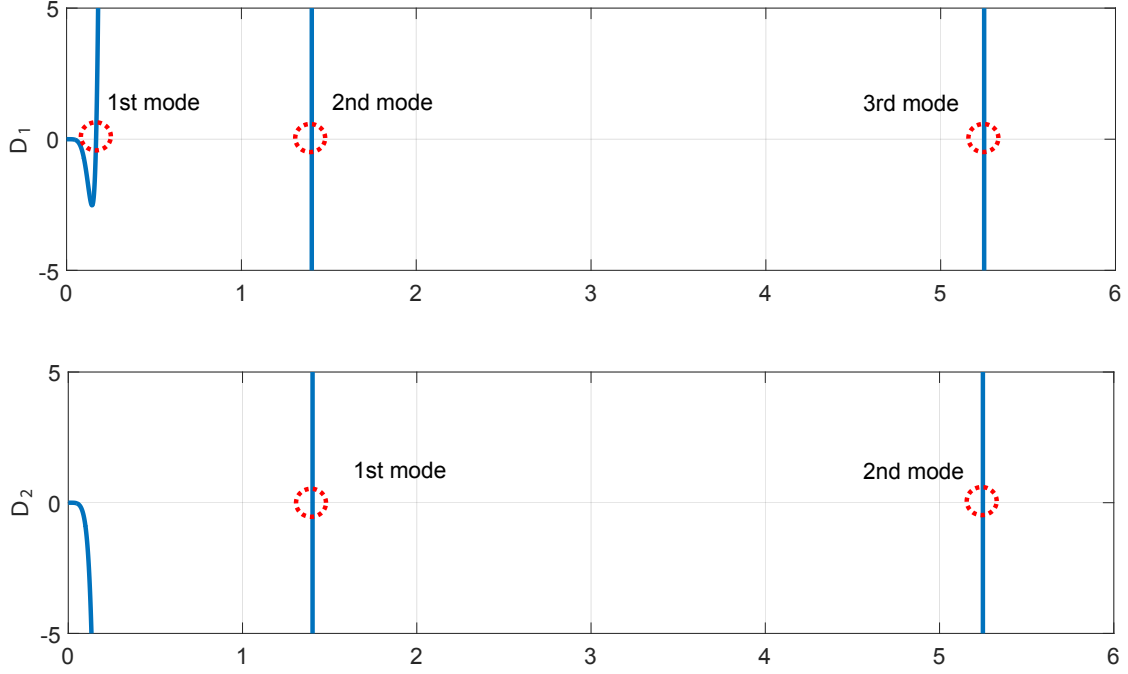


Figure 4-3: Solutions (β_1 , β_2 , and β_3) of the determinant \mathcal{D} with different parameters: the first determinant \mathcal{D}_1 is calculated very large total inertia I_0 which is 10^6 times of real inertia. In this case, the determinant has the first local minimum around the origin so that the first mode is also closed to the zero.

Frequency Equation and Coefficients

In this thesis, let us first derive the boundary conditions with non-zero M_d to see the structure of the equations. Once we put the spatial solution and its partial derivatives into the boundary conditions (4.8) and (4.9), then we can obtain a system of linear equations

$$[\mathcal{F}] \begin{bmatrix} C_3 \\ C_5 \end{bmatrix} = 0 \quad (4.15)$$

where $[\mathcal{F}]$ is 2 by 2 matrix. To exclude trivial solution, the determinant of $[\mathcal{F}]$ should be zero. The determinant is usually called frequency equation and we can obtain β_i

such that $\det(\mathcal{F}) = 0$ and

$$\begin{aligned}\mathcal{F}_{11} &= \left(-\beta^2 - \frac{M_d}{\rho A}\beta^4\right) \sin(\beta l_b) + \left(-\beta^2 + \frac{M_d}{\rho A}\beta^4\right) \sinh(\beta l_b) - \frac{I_0}{\rho A}\beta^5 \cos(\beta l_b) + \frac{I_0}{\rho A}\beta^5 \cosh(\beta l_b) \\ \mathcal{F}_{12} &= \frac{I_0}{\rho A}\beta^5 \sin(\beta l_b) + \frac{I_0}{\rho A}\beta^5 \sinh(\beta l_b) + \left(-\beta^2 - \frac{M_d}{\rho A}\beta^4\right) \cos(\beta l_b) + \left(-\beta^2 + \frac{M_d}{\rho A}\beta^4\right) \cosh(\beta l_b) \\ \mathcal{F}_{21} &= \frac{m_0}{\rho A}\beta^4 \sin(\beta l_b) - \frac{m_0}{\rho A}\beta^4 \sinh(\beta l_b) + \left(-\beta^3 + \frac{M_d}{\rho A}\beta^5\right) \cos(\beta l_b) + \left(-\beta^3 - \frac{M_d}{\rho A}\beta^5\right) \cosh(\beta l_b) \\ \mathcal{F}_{22} &= \left(\beta^3 - \frac{M_d}{\rho A}\beta^5\right) \sin(\beta l_b) + \left(-\beta^3 - \frac{M_d}{\rho A}\beta^5\right) \sinh(\beta l_b) + \frac{m_0}{\rho A}\beta^4 \cos(\beta l_b) - \frac{m_0}{\rho A}\beta^4 \cosh(\beta l_b)\end{aligned}$$

Then, the exact form of the determinant, denoted by \mathcal{D} , is given by

$$\begin{aligned}\mathcal{D} &\triangleq (I_0 m_0 - M_d^2)\beta^4 (1 - \cos(\beta l_b) \cosh(\beta l_b) - (A\rho I_0)\beta^3 (\sin(\beta l_b) \cosh(\beta l_b) + \cos(\beta l_b) \sinh(\beta l_b)) \\ &\quad - 2A\rho M_d \beta^2 \sin(\beta l_b) \sinh(\beta l_b) - (A\rho)m_0 \beta (\sin(\beta l_b) \cosh(\beta l_b) - \cos(\beta l_b) \sinh(\beta l_b)) \\ &\quad + A^2 \rho^2 (1 + \cos(\beta l_b) + \cosh(\beta l_b)) = 0\end{aligned}$$

If we put $M_d = 0$, then we can obtain the exactly same characteristic equation in [51] as

$$\begin{aligned}&\beta^4 (1 - \cos(\beta l_b) \cosh(\beta l_b) - (A\rho)I_0 \beta^3 (\sin(\beta l_b) \cosh(\beta l_b) + \cos(\beta l_b) \sinh(\beta l_b)) \\ &\quad - (A\rho)m_0 \beta (\sin(\beta l_b) \cosh(\beta l_b) - \cos(\beta l_b) \sinh(\beta l_b)) + A^2 \rho^2 (1 + \cos(\beta l_b) + \cosh(\beta l_b)) = 0\end{aligned}$$

Let us calculate the natural frequencies with a fixed M_d which is not zero. Particularly, I choose the maximum value of M_d that is the case of zero configuration. Since the determinant \mathcal{D} is transcendental function, we used `vpasolve` command in Matlab which is a numerical solver to get the specific β . When we calculate the solutions of the determinant, we applied physical parameters of our system (See, Sec. 4.4.1). The shape of the equation seem a unstable oscillation which is shown in Fig. 4-3. Numerical solutions of the determinant are

$$\beta_1 = 0.871166815557852, \quad \beta_2 = 5.050078226293192, \quad \beta_3 = 8.577533537496846 \quad (4.16)$$

To obtain the natural frequencies ω_i , we use the relation between the β and ω which is given by $\beta^4 = \omega^2 \rho A / (EI)$ for each β_i . Then the natural frequencies of the boom are

$$\omega_1 = 8.860223458999329 \text{ rad/s.} \rightarrow f_1 = 1.410148360398514 \text{ Hz}$$

$$\omega_2 = 297.7407226680140 \text{ rad/s.} \rightarrow f_2 = 47.386907772367557 \text{ Hz}$$

$$\omega_3 = 858.9480079850540 \text{ rad/s.} \rightarrow f_3 = 136.7058213297581e \text{ Hz}$$

Here, we found that the reason of quite small number of the first mode in the previous calculation was miscalculation of moment of inertia of motors. More specifically, I made a mistake during conversion of units. Please see the plots which compares the shape of determinants under two different inertia parameters.

we re-calculated natural frequencies with non-zero M_d at zero configuration, i.e. $\theta_s = \theta_1 = \theta_2 = \theta_3 = 0$. The first natural frequency is slightly faster than the real experimental result. The reason of the slower behavior of the real system seems the imperfect clamping at the end of the aluminium bar in our system. The base and clamping vice part are currently being modified.

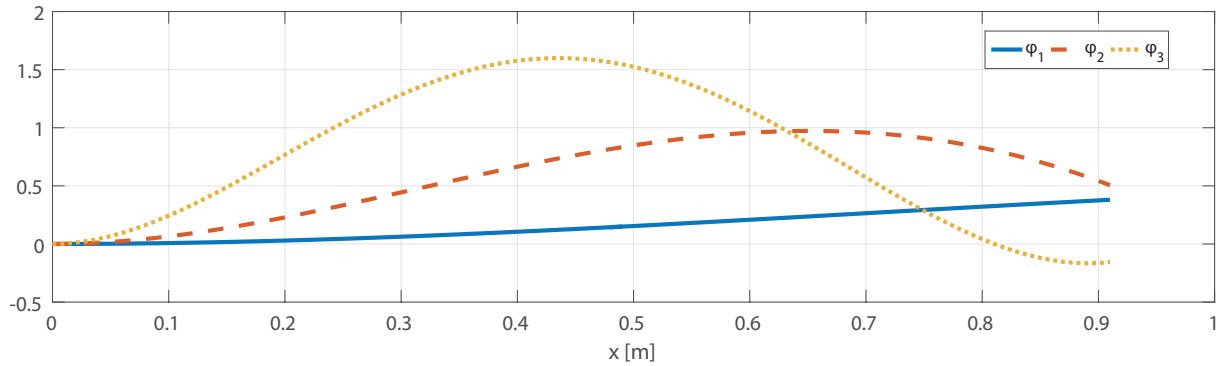


Figure 4-4: Three mode shapes

4.1.4 Euler-Lagrangian Equation

In order to use Euler-Lagrange equation, we need to define kinetic and potential energy of the system. First of all, total kinetic energy of the system is

$$T = T_\delta + T_s + \sum_{i=1}^{l_3} T_i$$

where T_δ , T_s , and T_i are the kinetic energy of the beam, stage, and the motor/link, respectively. Each kinetic energy is specifically defined by

$$\begin{aligned} T_\delta &= \frac{\rho A}{2} \int_0^{l_b} \dot{p}_{ob}(x)^T \dot{p}_{ob}(x) dx = \frac{\rho A}{2} \int_0^{l_b} \dot{w}(x, t)^2 dx \\ &= \frac{\rho A}{2} \sum_{i=1}^3 \sum_{j=1}^3 \dot{\delta}_i(t) \dot{\delta}_j(t) \underbrace{\int_0^{l_b} \phi_i(x) \phi_j(x) dx}_{:=a_{ij}} \\ T_s &= \frac{1}{2} m_s \dot{p}_{os}^T \dot{p}_{os} + \frac{1}{2} J_s \dot{\theta}_b^2 \\ &= \frac{1}{2} m_s \dot{p}_{os}^T \dot{p}_{os} + \frac{1}{2} J_s \left(\sum_{i=1}^3 \sum_{j=1}^3 \underbrace{\phi'_i(l_b) \phi'_j(l_b)}_{:=b_{ij}} \dot{\delta}_i \dot{\delta}_j \right) \\ T_i &= \frac{1}{2} m_i \dot{p}_{oi}^o{}^T \dot{p}_{oi}^o + \frac{1}{2} J_i \omega_{oi}^2, \end{aligned}$$

where ω_{oi} is angular velocity of i -th frame expressed in $\{\mathcal{O}\}$ and $\phi'_i(l_b) = d\phi_i(x)/dx$ evaluated at $x = l_b$. In addition, we can calculate a_{ij} and b_{ij} from the mode shapes determined in Sec. 4.1.3.

In addition, potential energy can be similarly defined as follow

$$U = \underbrace{U_{\delta_e} + U_{\delta_g}}_{:=U_\delta} + U_s + \sum_{i=1}^{l_3} U_i$$

where U_{δ_e} and U_{δ_g} are elastic and gravitational energy of the beam, respectively. The other terms follow the same subscripts in the kinetic energy in the above equation.

Then, we can express each potential energy term as

$$\begin{aligned}
U_{\delta_e} &= \frac{EI}{2} \int_0^{l_b} \left(\frac{d^2 w(x)}{dx^2} \right)^2 dx = \frac{EI}{2} \sum_{i=1}^3 \sum_{j=1}^3 c_{ij} \delta_i(t) \delta_j(t) \\
U_{\delta_g} &= \rho A \mathbf{g}^T \int_0^{l_b} p_{ob}^o(x) dx = -(\rho A l_b) g \left(\frac{1}{2} l_b \right) \\
U_s &= m_s \mathbf{g}^T p_{os}, \quad U_i = m_i \mathbf{g}^T p_{oi}
\end{aligned}$$

where $\mathbf{g} = [-g; 0] \in \mathfrak{R}^2$ is gravitational acceleration and, we have the following equations from the orthogonality property.

$$c_{ij} = \int_0^{l_b} \phi_i'' \phi_j'' dx = \begin{cases} 0 & i \neq j \\ \omega_i^2 / EI & i = j \end{cases} \quad (4.17)$$

Now we define generalized coordinate as $q := [q_r; q_f] \in \mathfrak{R}^7$ where $q_r = [q_3; q_2; q_1]$ and $q_f = [q_s; \delta_1; \delta_2; \delta_3]$. With the definition of the generalized coordinate and the Lagrangian $L = T - U$ of the system, we can obtain the dynamics as following

$$\begin{bmatrix} M_r & M_{rf} \\ M_{fr} & M_f \end{bmatrix} \begin{bmatrix} \ddot{q}_r \\ \ddot{q}_f \end{bmatrix} + \begin{bmatrix} C_r & C_{rf} \\ C_{fr} & C_f \end{bmatrix} \begin{bmatrix} \dot{q}_r \\ \dot{q}_f \end{bmatrix} + \begin{bmatrix} g_r \\ g_f \end{bmatrix} + \begin{bmatrix} 0 & 0 \\ 0 & K \end{bmatrix} \begin{bmatrix} q_r \\ q_f \end{bmatrix} = \begin{bmatrix} \tau_r \\ \tau_f \end{bmatrix} \quad (4.18)$$

where $K = \text{diag}([0; c_{11}; c_{22}; c_{33}]) \in \mathfrak{R}^{4 \times 4}$ is structural spring which can be simplified by the orthogonal property, $\tau_r = [\tau_3; \tau_2; \tau_1] \in \mathfrak{R}^3$, and $\tau_f = [\tau_s; 0; 0; 0] \in \mathfrak{R}^4$.

4.2 LQR-based Control Design

In this section, we design two control laws: 1) vibration-suppression control in the stage-vibration dynamics and 2) joint tracking control in its orthogonal complement. To achieve two different control objectives separately, we first deploy passive decomposition [11] to decompose the dynamics into the stage-vibration dynamics and its orthogonal complement. Due to the dynamically decomposed stage-beam dynamics, we can independently design the vibration suppression control by only using the stage

motion. For the vibration suppression control, we use the LQR control based on the controllability analysis of the linearized stage-beam dynamics. Finally, we design the joint tracking control and show the tracking error convergence if the vibration is sufficiently suppressed.

4.2.1 Passive Decomposition

In this thesis, what we want is to suppress the vibration of the flexible beam by using the stage motion while the manipulator follows the desired trajectory. However, due to the coupling terms in the inertia matrix, i.e. dynamic coupling, it is hard to separately design each control. To address this problem, we utilize passive decomposition [11] to decompose the dynamics (4.18) into stage-vibration dynamics and its orthogonal complement. We also show that if the vibration is suppressed, then the orthogonal complement dynamics is equivalent to the pure manipulator dynamics.

Following [11], let us first define the coordination map $h(q) = q_f$ which is the generalized coordinate of the stage and the beam. From the definition of each distribution, we can write the velocity of the system

$$\dot{q} = \begin{bmatrix} \Delta_{\top} & \Delta_{\perp} \end{bmatrix} \begin{bmatrix} v_{L_1} \\ v_{E_1} \end{bmatrix} = \underbrace{\begin{bmatrix} I_3 & S_{E_1} \\ 0_{4 \times 3} & I_4 \end{bmatrix}}_{:=S_1(q)} \underbrace{\begin{bmatrix} v_{L_1} \\ v_{E_1} \end{bmatrix}}_{:=\nu_1}$$

where $\Delta_{\top} = [I_3; 0_{4 \times 3}] \in \mathfrak{R}^{7 \times 3}$ and $\Delta_{\perp} = [S_{E_1}; I_4] \in \mathfrak{R}^{7 \times 4}$ are matrices identifying Δ^{\top} and Δ_{\perp} , respectively. $v_{L_1} \in \mathfrak{R}^3$ is the locked system motion and $v_{E_1} \in \mathfrak{R}^4$ is the shape system motion which is same as the motion of the stage-beam, i.e. \dot{q}_f . We can find $S_{E_1}(q) = -M_r^{-1}M_{rf} \in \mathfrak{R}^{3 \times 4}$ from the relation $\Delta_{\top}M(q)\Delta_{\perp} = 0$.

By multiplying S_1^T to equation (4.18) with the relations $\dot{q} = S_1\nu_1$ and $\ddot{q} = \dot{S}_1\nu_1 + S_1\dot{\nu}_1$, we can obtain the decomposed dynamics given by

$$\begin{bmatrix} M_{L_1} & 0 \\ 0 & M_{E_1} \end{bmatrix} \begin{bmatrix} \dot{v}_{L_1} \\ \dot{v}_{E_1} \end{bmatrix} + \begin{bmatrix} C_{L_1} & C_{L_1 E_1} \\ C_{E_1 L_1} & C_{E_1} \end{bmatrix} \begin{bmatrix} v_{L_1} \\ v_{E_1} \end{bmatrix} + \begin{bmatrix} g_{L_1} \\ g_{E_1} \end{bmatrix} + \begin{bmatrix} 0 \\ Kq_f \end{bmatrix} = \begin{bmatrix} \tau_{L_1} \\ \tau_{E_1} \end{bmatrix} \quad (4.19)$$

where $M_{L_1} = M_r$, $M_{E_1} = S_{E_1}^T M_{rf} + M_f$,

$$\begin{bmatrix} g_{L_1} \\ g_{E_1} \end{bmatrix} = \begin{bmatrix} g_r \\ S_{E_1}^T g_r + g_f \end{bmatrix}, \text{ and } \begin{bmatrix} \tau_{L_1} \\ \tau_{E_1} \end{bmatrix} = \begin{bmatrix} \tau_r \\ S_{E_1}^T \tau_r + \tau_f \end{bmatrix}$$

The Coriolis terms is calculated by $S_1^T (M(q)\dot{S}_1 + C(q, \dot{q})S_1)$ where $C(q, \dot{q})$ is the Coriolis matrix in (4.18).

The shape system still describes the dynamics of the stage and vibrational motion which we can express as

$$M_{E_1} \ddot{q}_f + C_{E_1} \dot{q}_f + K q_f + g_f = \tau_f + f_n \quad (4.20)$$

where $f_n := -C_{E_1 L_1} v_{L_1} + S_{E_1}^T (\tau_r - g_r)$ is the coupling force, and thus, we could interpret dynamics above by the mass-spring-damping system of q_f with the gravity g_f excited by the stage motion and the coupling force.

If the shape system is stabilized, i.e. $\dot{q}_f \rightarrow 0$, then the locked system converges to the pure manipulator dynamics as follows

$$M_r(q_r) \ddot{q}_r + C_r(q_r, \dot{q}_r) \dot{q}_r + g_r(q_r) = \tau_r$$

Thus, one possible approach to achieve two different control objectives, vibration suppression and tracking control, is to use the stage motion to subdue the vibration in the shape system and to design the tracking control in the locked system.

4.2.2 Vibration Suppression Control Design

We aim to stabilize the stage-beam dynamics with only the stage control input $\tau_s \in \mathfrak{R}$ regardless of the motion of the manipulator. However, since the stage-beam system is underactuated, i.e. one DOF stage actuation and four DOF stage-beam states, we cannot easily stabilize the stage-beam system through τ_s , and should examine the controllability of the system.

For the controllability analysis, let us define the state $x = [x_1; x_2] \in \mathfrak{R}^8$ where

$x_1 = q_f$ and $x_2 = \dot{q}_f$, and suppose that the manipulator is moving slowly enough to enable linearization of the shape system (4.20) around the equilibrium point with a fixed manipulator configuration. From the shape system dynamics, the equilibrium points can be found as

$$x_2^* = 0 \quad (4.21)$$

$$g_{E_1}(x_1^*, \bar{q}_r) + \bar{K}x_1^* = S_{E_1}^T \bar{\tau}_r \quad (4.22)$$

where $\bar{K} = \text{diag}([k_s; c_{11}; c_{22}; c_{33}])$ is the augmented stiffness with k_s . We assume that the manipulator motion is fixed at \bar{q}_r under the steady-state control input $\bar{\tau}_r$. This augmented stiffness comes from the design of the stage input expressed by

$$\tau_s = -k_s q_s - b_s \dot{q}_s + u_s \quad (4.23)$$

where the first two terms are for stabilization of the stage since the stage must be stable with the vibration suppressed. The last term u_s is the auxiliary control input for the vibration suppression. The second equilibrium equation (4.22) presents some offset deformation induced by gravity force and manipulator torque at a certain configuration of the manipulator.

Linearization of (4.20) at the equilibrium point gives the blocked matrices system

$$\dot{\tilde{x}} = F\tilde{x} + Gu_s = \begin{bmatrix} 0_{4 \times 4} & I_4 \\ F_1 & 0_{4 \times 4} \end{bmatrix} \begin{bmatrix} \tilde{x}_1 \\ \tilde{x}_2 \end{bmatrix} + \begin{bmatrix} 0_{4 \times 1} \\ G_1 \end{bmatrix} u_s \quad (4.24)$$

where $\tilde{x}_i = x_i - x_i^*$. The system matrices F_1 and $F_2 \in \Re^{4 \times 4}$ and input distribution matrix $G_1 \in \Re^4$ can be clearly expressed by

$$F_1 = -M_{E_1}^{-1} \left(\frac{\partial g_{E_1}}{\partial q_f} + \bar{K} - \frac{\partial S_{E_1}}{\partial q_f} \bar{\tau}_r \right), \quad G_1 = M_{E_1}^{-1} e_1$$

where $e_1 = [1; 0; 0; 0]$. All matrices and vectors are evaluated at the equilibrium point obtained from (4.21) and (4.22).

We then numerically analyze the controllability of the linearized stage-beam system for all manipulator's configuration, and find that the linearized system in which the control input is the only stage motion is controllable for every possible configuration of the manipulator. The fact that the configurations of robotic system is not able to affect the controllability seems reasonable because configurations mostly influence on the change of the gravity vector g_{E_1} . When the manipulator is stretched out, the gravity term is equal to zero (See (a) in Fig. 4-6). Even in this case, the linearized system is controllable due to $-M_{E_1}^{-1}\bar{K}$ term in F_1 .

Based on the controllability analysis, the LQR control can be used for the stage input to suppress the vibration

$$u_s = -K_{\text{LQR}}\tilde{x} \quad (4.25)$$

where $K_{\text{LQR}} \in \mathfrak{R}^{1 \times 8}$ is the LQR gain and $\tilde{x} = [\tilde{x}_1; \tilde{x}_2]$. Therefore, by combining (4.23) and (4.25), total input of the stage is given by

$$\tau_s = -k_s\theta_s - b_s\dot{\theta}_s - K_{\text{LQR}}\tilde{x} \quad (4.26)$$

The controllability analysis and LQR control design are based on slower operator behavior assumptions, i.e., $\dot{q}_r \approx 0$, but our approach has been shown to work properly as observed in the experiments in Sec. 3.4.

4.2.3 Joint Tracking Control Design

To attain the joint tracking control, consider the locked system:

$$M_{L_1}\dot{v}_{L_1} + C_{L_1}v_{L_1} + C_{L_1E_1}\dot{q}_f + g_{L_1} = \tau_{L_1} \quad (4.27)$$

where again $v_L = \dot{q}_r - S_{E_1}\dot{q}_f \in \mathfrak{R}^3$. Since the locked system is fully-actuated, we can easily design the tracking control s.t.,

$$\tau_{L_1} = f_L^n + M_{L_1}\ddot{q}_r^d - B_L\dot{e}_L - K_L e_L \quad (4.28)$$

where $f_L^n = M_L\dot{S}_{E_1}\dot{q}_f + C_{L_1}(\dot{q}_r^d - S_{E_1}\dot{q}_f) + C_{L_1E_1}\dot{q}_f + g_{L_1}$ is the cancel out terms, $e_L = q_r - q_r^d$ is the tracking error, and q_r^d is the desired joint trajectory. Here, for the control design, we use the passivity property of the dynamics, i.e. skew symmetric property of $\dot{M}_{L_1} - 2C_{L_1}$. Then, it is possible to obtain the closed-loop dynamics by

$$M_{L_1}\ddot{e}_L + (C_{L_1} + B_L)\dot{e}_L + K_L e_L = -M_{rf}\ddot{q}_f \quad (4.29)$$

which converges to

$$M_{L_1}\ddot{e}_L + (C_{L_1} + B_L)\dot{e}_L + K_L e_L = 0 \quad (4.30)$$

as the vibration is suppressed as obtained in Sec. 4.2.2.

Theorem 1 *Consider the linearized shape system (4.24) with the vibration suppression control (4.26) and the locked system (4.27) with the controls (4.23) and (4.28). Then the following are true:*

1. *vibration is suppressed, i.e. $\dot{q}_f \rightarrow 0$*
2. *manipulator follows the desired trajectory, i.e. $(q_r - q_r^d) \rightarrow 0$*

Proof: Let us first consider the shape system dynamics (4.20) and the stage input (4.23). Then, as explained in Sec. 4.2.2, the linearized system of the shape system dynamics becomes

$$\dot{x} = F\tilde{x} + Gu_s$$

Based on the controllability analysis in Sec. 4.2.2, we can design the stage motion controller u_s as defined in (4.25) such that the closed-loop system $\dot{x} = (F - GK_{\text{LQR}})\tilde{x}$

is stable, i.e. $\tilde{x} \rightarrow 0$. Thus, we can conclude that $q_f \rightarrow q_f^*$ and $\dot{q}_f \rightarrow 0$, i.e. the vibration is suppressed.

Next, let us define the Lyapunov function candidate as

$$W = \frac{1}{2}\dot{e}_L^T M_{L_1} \dot{e}_L + \frac{1}{2}e_L^T K_L e_L$$

where again $e_L = q_r - q_r^d$, M_L is the inertia matrix of the locked system, and K_L is the position feedback gain matrix in (4.28). Then we obtain the time derivative of W

$$\begin{aligned} \dot{W} &= \dot{e}_L^T M_{L_1} \ddot{e}_L + \frac{1}{2}\dot{e}_L^T \dot{M}_{L_1} \dot{e}_L + \dot{e}_L^T K_L e_L \\ &= -\dot{e}_L^T B_L \dot{e}_L + \dot{e}_L^T M_{L_1} (-M_{rf} \ddot{q}_f) \end{aligned}$$

For the second line, we use the passivity property, that is, $\dot{M}_{L_1} - 2C_{L_1}$ is skew symmetric. Furthermore, if the vibration is suppressed and the stage is stabilized so that $\dot{q}_f = \ddot{q}_f \approx 0$, then we obtain $\dot{W} = -\dot{e}_L^T B_L \dot{e}_L$. Then, according to Barbalat's lemma with the closed-loop dynamics (4.30), we can conclude that the equilibrium $\dot{e}_L = e_L = 0$ is globally asymptotically stable. \blacksquare

4.3 Lyapunov-based Control Design

In the previous section, we decompose the original system into the stage-vibration system and its orthogonal complement. The drawback of the approach is the linearization for the vibration suppression, which means that the stabilization is *locally* valid around the equilibrium point. However, when the manipulator motion is aggressive or external disturbance is large, the LQR control could not stabilize the flexible part. For this reason, in this section, we improved the control of vibration suppression in both the theoretical and practical sense by using the control design based on Lyapunov functions. To show the relation between the stage input and the vibration dynamics, we first start with the decomposition with the different coordination map.

4.3.1 Twice Passive Decomposition for Input Coupling

Here, we define the coordination map $h_2(q) = q_r$ which is the generalized coordinate of the manipulator. From the above definition of each distribution, we can write the velocity of the system

$$\dot{q} = \underbrace{\begin{bmatrix} I_3 & 0_{3 \times 4} \\ S_{E_2} & I_4 \end{bmatrix}}_{:=S_2(q)} \underbrace{\begin{bmatrix} v_{E_2} \\ v_{L_2} \end{bmatrix}}_{:=\nu_2}$$

where $S_{E_2} = -M_f^{-1}M_{fr} \in \mathfrak{R}^{4 \times 3}$, the shape system motion, in this case, is same as the motion of the manipulator, i.e. $v_{E_2} = \dot{q}_r \in \mathfrak{R}^3$, and the locked system motion is defined by $v_{L_2} = \dot{q}_f - S_{E_2}v_{E_2} = \dot{q}_f - S_{E_2}\dot{q}_r \in \mathfrak{R}^4$.

The decomposed dynamics is given by

$$\begin{bmatrix} M_{E_2} & 0 \\ 0 & M_{L_2} \end{bmatrix} \begin{bmatrix} \dot{v}_{E_2} \\ \dot{v}_{L_2} \end{bmatrix} + \begin{bmatrix} C_{E_2} & C_{E_2 L_2} \\ C_{L_2 E_2} & C_{L_2} \end{bmatrix} \begin{bmatrix} v_{E_2} \\ v_{L_2} \end{bmatrix} + \begin{bmatrix} g_{E_2} \\ g_{L_2} \end{bmatrix} + \begin{bmatrix} S_{E_2}^T K q_f \\ K q_f \end{bmatrix} = \begin{bmatrix} \tau_{E_2} \\ \tau_{L_2} \end{bmatrix} \quad (4.31)$$

where $M_{E_2} = M_r + S_{E_2}^T M_{fr}$, $M_{L_2} = M_f$,

$$\begin{bmatrix} g_{E_2} \\ g_{L_2} \end{bmatrix} = \begin{bmatrix} g_r + S_{E_2}^T g_f \\ g_f \end{bmatrix}, \text{ and } \begin{bmatrix} \tau_{E_2} \\ \tau_{L_2} \end{bmatrix} = \begin{bmatrix} \tau_r + S_{E_2}^T \tau_f \\ \tau_f \end{bmatrix}.$$

The shape system is the dynamics of the manipulator in which the dynamics of the stage-vibration part is included. Then, the tracking of the manipulator can be easily achieved without the assumption of the suppression of the vibration because there is no acceleration term of the stage-vibration term as (4.29).

On the other hand, the locked system is the nonlinear system that consists of the motion not only of the stage-vibration but also of the manipulator. The challenge for the control design of the locked system is the under-actuated property. To address this problem, we design the nonlinear control based on Lyapunov function analysis, which guarantees exponential stability for the nominal (pure) flexible dynamics. We

also show the boundedness of the vibration with the boundedness of disturbance (in this case, dynamic coupling force) under the tracking control of the manipulator.

To see the relation between the stage input and the dynamics of the vibration, we further decompose only the *locked system* as follows

$$\begin{bmatrix} v_{L_2}^1 \\ v_{L_2}^2 \end{bmatrix} = \begin{bmatrix} 1 & S_\delta \\ 0_{3 \times 1} & I_3 \end{bmatrix} \begin{bmatrix} v_s \\ v_\delta \end{bmatrix}$$

where $S_\delta = -M_s^{-1}M_{s\delta} \in \mathfrak{R}^{1 \times 3}$ with the locked system dynamics in (4.31)

$$\begin{bmatrix} M_s & M_{s\delta} \\ M_{\delta s} & M_\delta \end{bmatrix} \begin{bmatrix} \dot{v}_{L_2}^1 \\ \dot{v}_{L_2}^2 \end{bmatrix} + \begin{bmatrix} h_{L_2}^1 \\ h_{L_2}^2 \end{bmatrix} + \begin{bmatrix} 0 \\ K_\delta q_\delta \end{bmatrix} = \begin{bmatrix} \tau_s \\ 0_{3 \times 1} \end{bmatrix}$$

If we assume the manipulator motion is fixed, for intuition, we can consider $v_{L_2}^1 \in \mathfrak{R}$ as the velocity of the stage and $v_{L_2}^2 \in \mathfrak{R}^3$ as the velocity of the deflection. Also, $q_\delta = [\delta_1; \delta_2; \delta_3]$, $K_\delta = \text{diag}[c_{11}; c_{22}; c_{33}]$ in (4.17), and the nonlinear term $h_{L_2} = [h_{L_2}^1; h_{L_2}^2]$ includes the Coriolis and gravity term.

The secondary decomposed system is given by

$$\begin{bmatrix} M_s & 0_{1 \times 3} \\ 0_{3 \times 1} & M_\delta + S_\delta^T M_{s\delta} \end{bmatrix} \begin{bmatrix} \dot{v}_s \\ \dot{v}_\delta \end{bmatrix} + \begin{bmatrix} h_s \\ h_\delta \end{bmatrix} + \begin{bmatrix} 0 \\ K_\delta q_\delta \end{bmatrix} = \begin{bmatrix} \tau_s \\ S_\delta^T \tau_s \end{bmatrix}$$

Even if the lower part of the previous dynamic is a nonlinear dynamics, we can simply express the system as mechanically flat (i.e., whose inertial matrix is constant) by using the interconnected representation as described in the next subsection.

4.3.2 Interconnected System Description

If we consider the whole system as the interconnected system between the rigid part (i.e., the manipulator and the stage) and the flexible part and define the internal

wrench as f_{int} , then the dynamics of the flexible part can be expressed as

$$\frac{d}{dt} \left(\frac{\partial L_\delta}{\partial \dot{q}_\delta} \right) - \frac{\partial L_\delta}{\partial q_\delta} = \bar{M}_\delta \ddot{q}_\delta + K_\delta q_\delta = J_\delta^T (-f_{\text{int}}) \quad (4.32)$$

where the Lagrangian of the flexible part is $L_\delta = T_\delta - U_\delta$. The inertia matrix $\bar{M}_\delta \in \mathfrak{R}^{3 \times 3}$ and structural spring $K_\delta \in \mathfrak{R}^{3 \times 3}$ are constant, and Jacobian matrix J_δ is defined as follow

$$\begin{bmatrix} \dot{\theta}_b \\ \dot{p}_{ob}^y \end{bmatrix} = J_\delta \dot{q}_\delta = \begin{bmatrix} \phi'_1(l_b) & \phi'_2(l_b) & \phi'_3(l_b) \\ \phi_1(l_b) & \phi_2(l_b) & \phi_3(l_b) \end{bmatrix} \dot{q}_\delta \quad (4.33)$$

Remark 1 *From the lower part of the secondary decomposed dynamics, we can rewrite the driving force as*

$$J_\delta^T (-f_{\text{int}}) = S_\delta^T \tau_s + h(\ddot{q}, \dot{q}, q) \quad (4.34)$$

where $h(\ddot{q}, \dot{q}, q)$ is the dynamics coupling force.

Proof: The proof is straightforward. Let us first consider the dynamics of the flexible part in (4.18). The last three rows are

$$\begin{aligned} & \frac{d}{dt} \left(\frac{\partial L}{\partial \dot{q}_\delta} \right) - \frac{\partial L}{\partial q_\delta} = 0 \\ \Rightarrow & \frac{d}{dt} \left[\frac{\partial}{\partial \dot{q}_\delta} (L_r + L_\delta) \right] - \frac{\partial}{\partial q_\delta} (L_r + L_\delta) = 0 \end{aligned} \quad (4.35)$$

Then, one can see that the inertia matrix corresponding to the flexible part M_δ consists of \bar{M}_δ and $M_\delta^r(q)$.

$$M_\delta \triangleq \bar{M}_\delta + M_\delta^r(q)$$

Note that $M_\delta^r(q)$ is time-varying term different from the constant \bar{M}_δ .

Now call the low part of the secondary decomposed dynamics with M_δ which is given by

$$\begin{aligned} (\bar{M}_\delta + M_\delta^r(q) + S_\delta^T M_{s\delta}) \frac{d}{dt} (\dot{q}_\delta + S_{E_2}^{2:4} \dot{q}_r) + h_\delta(\dot{q}, q) \\ + K_\delta q_\delta = S_\delta^T \tau_s \end{aligned}$$

One can rewrite the above equation as

$$\bar{M} \ddot{q}_\delta + K_\delta q_\delta = S_\delta^T \tau_s + h(\ddot{q}, \dot{q}, q)$$

■

Therefore, the exact representation of S_δ is necessary for the design of the control, and we model the system as interconnected systems to reveal the term of S_δ . The connection between the rigid system and the flexible system is the internal wrench f_{ext} . What we want to do is to stabilize the flexible system by using the stage input τ_s . Since the internal wrench appears only in the dynamics of θ_b and p_{ob}^y , we should use the coupling force. However, using the dynamics coupling could be complicated and not intuitive, so we use the passive decomposition to explicitly indicate how τ_s affects the dynamics of θ_b and p_{ob}^y .

Let us define the coordination map as $h_1(q) := q_m$ and following [11], we get

$$\begin{bmatrix} \dot{q}_m \\ \dot{q}_t \end{bmatrix} = \begin{bmatrix} I_3 & 0 \\ S_E & I_3 \end{bmatrix} \begin{bmatrix} v_E \\ v_L \end{bmatrix} \quad (4.36)$$

where $S_E = -M_t^{-1} M_{tm} \in \Re^{3 \times 3}$ and the decomposed dynamics

$$\begin{bmatrix} M_E & 0 \\ 0 & M_L \end{bmatrix} \begin{bmatrix} \dot{v}_E \\ \dot{v}_L \end{bmatrix} + \begin{bmatrix} C_E & C_{EL} \\ C_{LE} & C_L \end{bmatrix} \begin{bmatrix} v_E \\ v_L \end{bmatrix} + \begin{bmatrix} g_m + S_E^T g_t \\ g_t \end{bmatrix} = \begin{bmatrix} \tau_m + S_E^T \tau_t \\ \tau_t \end{bmatrix} + \begin{bmatrix} 0 \\ F_{\text{int}} \end{bmatrix} \quad (4.37)$$

where $M_E = M_m - M_{mt}M_t^{-1}M_{tm}$, $M_L = M_t$, and $F_{\text{int}} = [0; f_{\text{int}}] = [0; f_{\text{int}}^r; f_{\text{int}}^y] \in \mathfrak{R}^3$. One can see that the gravitational force the control input of the dynamics of q_t remains intact. Thus,

$$M_L \dot{v}_L + C_{LE} v_E + C_L v_L + g_t = \begin{bmatrix} \tau_s \\ 0 \end{bmatrix} + \begin{bmatrix} 0 \\ f_{\text{int}} \end{bmatrix}$$

and $v_L = \dot{q}_t - S_E \dot{q}_m$ from (4.36).

We decompose the dynamics further to see the direct affection of τ_s on f_{int} by defining

$$\begin{bmatrix} v_L^s \\ v_L^b \end{bmatrix} = \begin{bmatrix} 1 & S_L \\ 0 & I_2 \end{bmatrix} \begin{bmatrix} v_{L'} \\ v_{E'} \end{bmatrix}$$

where $S_L = -M_{L^1}^{-1}M_{L^{12}} \in \mathfrak{R}^{1 \times 2}$, M_{L^1} is the (1,1) element of M_L , and $M_{L^{12}} \in \mathfrak{R}^{1 \times 2}$ is the (1,2:3) part of M_L . Then, the twice decomposed dynamics is

$$\begin{bmatrix} M_{L'} & 0 \\ 0 & M_{E'} \end{bmatrix} \begin{bmatrix} \dot{v}_{L'} \\ \dot{v}_{E'} \end{bmatrix} + \begin{bmatrix} C_{L'} & C_{L'E'} \\ C_{E'L'} & C_{E'} \end{bmatrix} \begin{bmatrix} v_{L'} \\ v_{E'} \end{bmatrix} + \begin{bmatrix} g_t^1 \\ g_t^{23} + S_L^T g_t^1 \end{bmatrix} = \begin{bmatrix} \tau_s \\ S_L^T \tau_s \end{bmatrix} + \begin{bmatrix} 0 \\ f_{\text{int}} \end{bmatrix} \quad (4.38)$$

The second row of the doubly decomposed dynamics (4.38) can be written by

$$\underbrace{M_{E'} \dot{v}_{E'} + C_{E'L'} v_{L'} + C_{E'} v_{E'} + g_t^{23} + S_L^T g_t^1}_{:=h_{E'}} - S_L^T \tau_s = f_{\text{int}}$$

We can interpret the above equation to mean that the internal wrench consists of the dynamics effect, $h_{E'}$, and the stage input $S_L^T \tau_s$.

$$f_{\text{int}} = h_{E'} - S_L^T \tau_s \quad (4.39)$$

Here, $S_L = S_\delta$ in (4.34). Thus, we find $S_\delta = S_L = -M_{L^1}^{-1}M_{L^{12}} \in \mathfrak{R}^{1 \times 2}$.

4.3.3 Passivity-based Manipulator Motion Control

The shape system of the first decomposed system (4.31) is given by

$$M_E \dot{v}_E + C_E v_E + \underbrace{C_{EL} v_L + g_m + S_E^T g_t}_{:=h_E} = \tau_m + S_E^T \tau_t \quad (4.40)$$

where $v_E = \dot{q}_m$.

Let us define the control τ_m for the trajectory tracking as follows

$$\tau_m = M_E \ddot{q}_m^d + C_E \dot{q}_m^d + h_E - S_E^T \tau_t - B_E \dot{e}_E - K_E e_E$$

where $e_E = q_m - q_m^d$ and q_m^d is the desired trajectory of the manipulator. Then the closed-loop equation is

$$M_E \ddot{e}_E + (C_E + B_E) \dot{e}_E + K_E e_E = 0$$

which implies asymptotic stability of the closed-loop system.

4.3.4 Dissipative Control for Vibration Suppression

From (4.35) and (4.34), one observes that the flexible system is mass-spring system with a single input and external disturbance. Although we do not rigorously develop the mathematical model of the structural damping which physically exists, from now on, we consider the structural damping in the dynamics of the flexible part.

$$M_\delta \ddot{q}_\delta + B_\delta \dot{q}_\delta + K_\delta q_\delta = S_\delta^T \tau_s + h(\ddot{q}, \dot{q}, q) \quad (4.41)$$

where $B_\delta \in \mathfrak{R}^{3 \times 3}$ is the structural damping matrix and diagonal.

We can consider the dynamics coupling $h(\ddot{q}, \dot{q}, q)$ as the disturbance, then the

nominal system is

$$M_\delta \ddot{q}_\delta + B_\delta \dot{q}_\delta + K_\delta q_\delta = S_\delta^T \tau_s \quad (4.42)$$

Even if M_δ , B_δ , and K_δ are constant, the nominal system is nonlinear system because of $S_\delta(q) = -M_s^{-1}M_{s\delta}$. Therefore, the well-developed analysis and control framework for linear system cannot be applicable. Furthermore, since S_δ includes the coordinate of the manipulator, the system is nonlinear nonautonomous system. In fact, due to S_δ , it is also difficult to make the system in triangular cascade form. Thus, we design the control for the stabilize the flexible system by using Lyapunov function analysis.

Now our task is to design the control for the suppression of the vibration in (4.42). We suppose that the control input τ_s has first-order dynamics such as

$$\dot{\tau}_s = -\lambda \tau_s + u_s \quad (4.43)$$

where $\lambda \in \Re$ is a positive constant. Let us define the PD-like control for the auxiliary control input u_s as

$$u_s = -S_\delta (B_d \dot{q}_\delta + K_d q_\delta) \quad (4.44)$$

where B_d and K_d are constant gain.

Proposition 1 *Consider the nominal system of the flexible part in (4.42) and assume that the control input τ_s is chosen as its dynamics is (4.43) with the auxiliary input u_s in (4.44). Then, the configuration and velocity of the flexible system q_δ, \dot{q}_δ converges exponentially to zero.*

Proof: Let us construct the Lyapunov candidate as

$$V = \frac{1}{2} \begin{bmatrix} q_\delta \\ \dot{q}_\delta \end{bmatrix}^T \begin{bmatrix} B_d K_f + K_d B_f & K_d M_\delta \\ (K_d M_\delta)^T & B_d M_\delta \end{bmatrix} \begin{bmatrix} q_\delta \\ \dot{q}_\delta \end{bmatrix} + \frac{1}{2\gamma} \tau_s^T \tau_s$$

Since $M_\delta \succeq 0$ and structural damping/spring are diagonal with positive constant

elements, it is straightforward to verify that $V > 0$.

Differentiating V , one obtains

$$\begin{aligned}
\dot{V} &= \begin{bmatrix} q_\delta \\ \dot{q}_\delta \end{bmatrix}^T \begin{bmatrix} B_d K_\delta + K_d B_\delta & K_d M_\delta \\ (K_d M_\delta)^T & B_d M_\delta \end{bmatrix} \begin{bmatrix} \dot{q}_\delta \\ \ddot{q}_\delta \end{bmatrix} + \frac{1}{\gamma} \tau_s^T \dot{\tau}_s \\
&= \begin{bmatrix} q_\delta^T (B_d K_\delta + K_d B_\delta) + \dot{q}_\delta^T (K_d M_\delta)^T \\ q_\delta^T (K_d M_\delta) + \dot{q}_\delta^T B_d M_\delta \end{bmatrix}^T \begin{bmatrix} \dot{q}_\delta \\ \ddot{q}_\delta \end{bmatrix} + \frac{1}{\gamma} \tau_s^T \dot{\tau}_s \\
&= q_\delta^T (B_d K_\delta + K_d B_\delta) \dot{q}_\delta + \dot{q}_\delta^T (K_d M_\delta)^T \dot{q}_\delta + q_\delta^T (K_d M_\delta) \ddot{q}_\delta + \dot{q}_\delta^T B_d M_\delta \ddot{q}_\delta + \frac{1}{\gamma} \tau_s^T \dot{\tau}_s \\
&= q_\delta^T (B_d K_\delta + K_d B_\delta) \dot{q}_\delta + \dot{q}_\delta^T (K_d M_\delta)^T \dot{q}_\delta + q_\delta^T K_d (-B_\delta \dot{q}_\delta - K_\delta q_\delta + S_\delta^T \tau_s) \\
&\quad + \dot{q}_\delta^T B_d (-B_\delta \dot{q}_\delta - K_\delta q_\delta + S_\delta^T \tau_s) + \frac{1}{\gamma} \tau_s^T \dot{\tau}_s \\
&= -\dot{q}_\delta^T (B_d B_\delta - K_d M_\delta) \dot{q}_\delta - q_\delta^T K_d K_\delta q_\delta + \tau_s^T \left[S_\delta (B_d \dot{q}_\delta + K_d q_\delta) + \frac{1}{\gamma} \dot{\tau}_s \right] \\
&= - \begin{bmatrix} q_\delta \\ \dot{q}_\delta \end{bmatrix}^T \begin{bmatrix} K_d K_\delta & 0 \\ 0 & B_d B_\delta - K_d M_\delta \end{bmatrix} \begin{bmatrix} q_\delta \\ \dot{q}_\delta \end{bmatrix} - \frac{\lambda}{\gamma} \tau_s^T \tau_s
\end{aligned}$$

If K_d is small enough, then the equilibrium $q_\delta = \dot{q}_\delta = \tau_s = 0$ is exponentially stable. ■

We should see the stability of the perturbed system (4.41). For this, we assume that the manipulator converges to the desired trajectory which is given by bounded-continuous function $(\ddot{q}_r^d(t), \dot{q}_r^d(t), q_r^d(t))$ with the control (4.40). This means that the human arbitrary command is smooth. Then, we can assume that the disturbance $h(\ddot{q}, \dot{q}, q) = h(\dot{q}_\delta, q_\delta, t)$ is bounded.

Theorem 2 *Let us first denote $x(t) = [q_\delta(t); \dot{q}_\delta(t); \tau_s(t)] \in \mathfrak{R}^7$. Consider the nominal system of the flexible part in (4.41) and assume that the control input τ_s is chosen as its dynamics is (4.43) with the auxiliary input u_s in (4.44). Suppose that the motion of the manipulator converges to the desired trajectory $q_r^d(t) \in \mathcal{C}^2$ and \mathcal{L}_2 . Suppose further that the perturbation term $h(\ddot{q}, \dot{q}, q)$ satisfies*

$$h(\ddot{q}, \dot{q}, q) \approx h(\dot{q}_\delta, q_\delta, t) \leq \bar{\kappa}$$

for all $t \geq 0$, all q_δ and \dot{q}_δ . Then, $x(t)$ of the perturbed system (4.41) satisfies

$$\begin{aligned}\|x(t)\| &\leq \sqrt{\frac{\lambda_{\max}(P)}{\lambda_{\min}(P)}} \|x(t_0)\|, \quad \forall t_0 \leq t \leq t_0 + T \\ \|x(t)\| &\leq \frac{c_1 \bar{\kappa}}{\theta \lambda_{\min}(Q_\delta)} \sqrt{\frac{\lambda_{\max}(P)}{\lambda_{\min}(P)}}, \quad \forall t \geq t_0 + T\end{aligned}$$

Proof: We use the same V in Cor. 1 as a Lyapunov function candidate for the perturbed system (4.41). The derivative of V along the trajectories of (4.41) satisfies

$$\begin{aligned}\dot{V} &= - \begin{bmatrix} q_\delta \\ \dot{q}_\delta \end{bmatrix}^T \underbrace{\begin{bmatrix} K_d K_\delta & 0 \\ 0 & B_d B_\delta - K_d M_\delta \end{bmatrix}}_{:=Q_\delta} \underbrace{\begin{bmatrix} q_\delta \\ \dot{q}_\delta \end{bmatrix}}_{:=x_\delta} - \frac{\lambda}{\gamma} \tau_s^T \tau_s - h^T \begin{bmatrix} K_d & B_d \end{bmatrix} \begin{bmatrix} q_\delta \\ \dot{q}_\delta \end{bmatrix} \\ &\leq -\lambda_{\min}(Q_\delta) \|x_\delta\|^2 - \frac{\lambda}{\gamma} \|\tau_s\|^2 - \|h\| \underbrace{\max(K_d, B_d)}_{:=c_1} \|x_\delta\| \\ &\leq -(1-\theta) \lambda_{\min}(Q_\delta) \|x_\delta\|^2 - \theta \lambda_{\min} \|x_\delta\|^2 - c_1 \|h\| \|x_\delta\| - \frac{\lambda}{\gamma} \|\tau_s\|^2, \quad 0 \leq \theta \leq 1 \\ &\leq -(1-\theta) \lambda_{\min}(Q_\delta) \|x_\delta\|^2 - \frac{\lambda}{\gamma} \|\tau_s\|^2, \quad \forall \|x_\delta\| \geq \frac{c_1 \bar{\kappa}}{\theta \lambda_{\min}(Q_\delta)}\end{aligned}$$

To use the ultimate bound theorem in [53], we have to find the lower and upper bound of the Lyapunov function. In our case, from the definition of V , we have

$$\lambda_{\min}(P) \|x\|_2^2 \leq V = \frac{1}{2} \begin{bmatrix} q_\delta \\ \dot{q}_\delta \\ \tau_s \end{bmatrix}^T \begin{bmatrix} B_d K_f + K_d B_f & K_d M_\delta & 0 \\ (K_d M_\delta)^T & B_d M_\delta & 0 \\ 0 & 0 & 1/\gamma \end{bmatrix} \begin{bmatrix} q_\delta \\ \dot{q}_\delta \\ \tau_s \end{bmatrix} := \frac{1}{2} x^T P x \leq \lambda_{\max}(P) \|x\|_2^2$$

Then, the ultimate bound by using theorem 4.18 in [53] is given by

$$\|x(t)\| \leq \frac{c_1 \bar{\kappa}}{\theta \lambda_{\min}(Q_\delta)} \sqrt{\frac{\lambda_{\max}(P)}{\lambda_{\min}(P)}}, \quad \forall t \geq t_0 + T$$

■

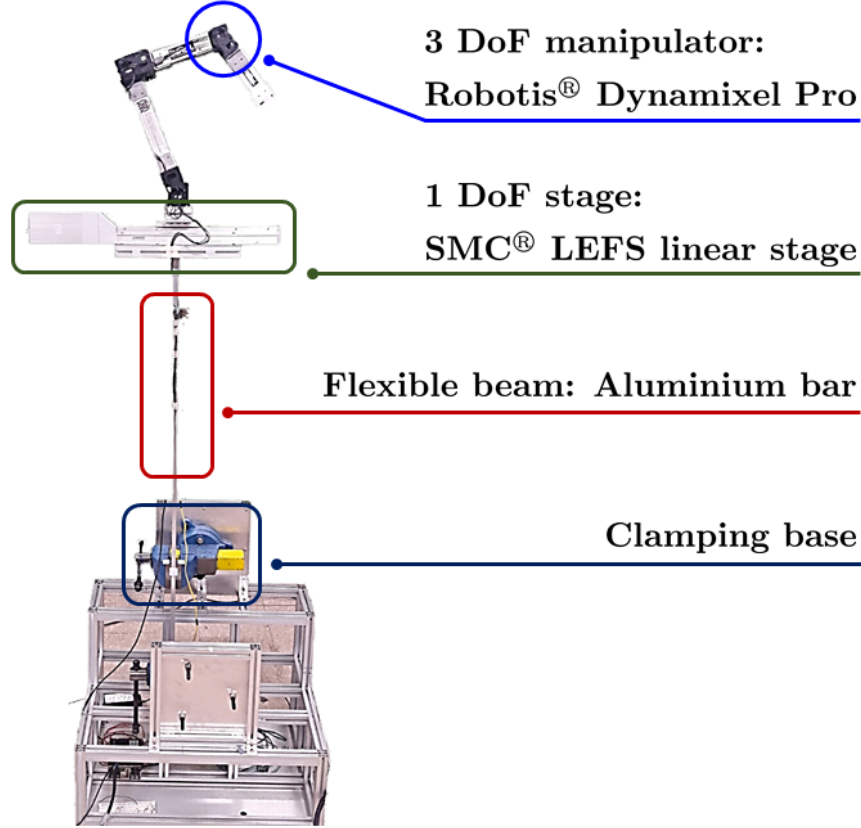


Figure 4-5: Experiment setup consists of three DOF manipulator, one DOF linear stage, and the flexible beam. Each actuator is torque-controllable

4.4 Experiments

We conduct experiments to verify the performance of the proposed controllers designed in Sec. 4.2.2 and 4.2.3. The performances of the trajectory tracking and vibration suppression are provided. During the tracking, we excite the system to show the robustness of the proposed controllers.

4.4.1 Test Setup

The system consists of three DOF manipulator, one DOF linear stage, and a vertical flexible beam. See Fig. 4-5. First of all, we have chosen the Dynamixel Pro of Robotics for the motors of the manipulator because of its compact size, acceptable torque level, and torque-controllability. The resolution of encoders is 501,900 or 304,000 p/rev according to the model of the motors. The Dynamixel Pro supports torque control

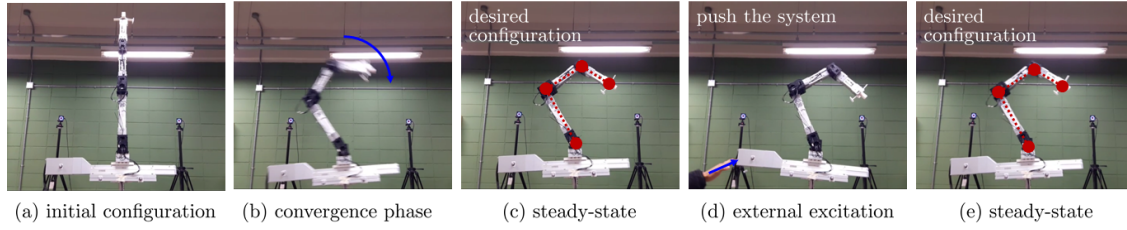


Figure 4-6: The snapshots of the joint tracking experiment: (a) the manipulator starts with the large initial error; (b) the manipulator converges to the desired configuration; (c) the system is stabilized due to the vibration suppression control or the structural damping (in the case of without the vibration suppression control); (d) the external disturbance (human force) is applied; and (e) again, the system is stabilized.

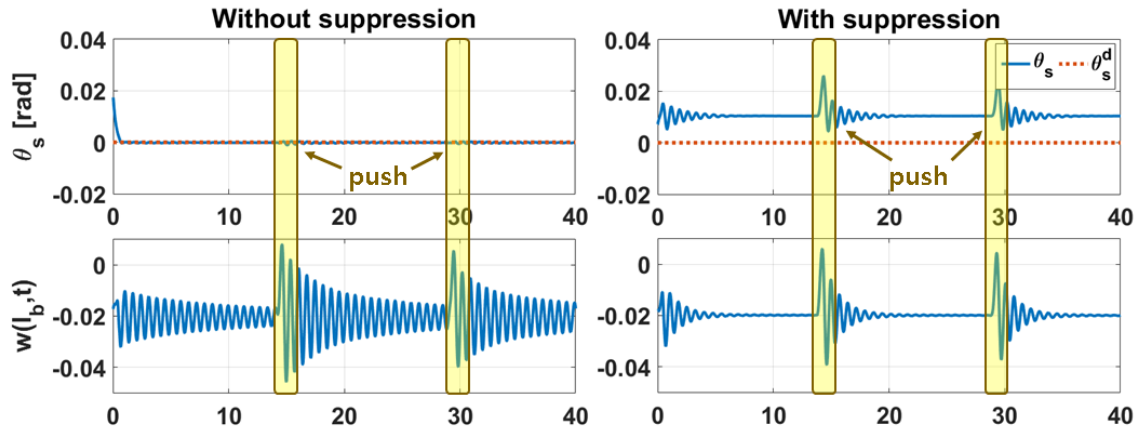


Figure 4-7: The linear stage and the deflection of the flexible beam: the beam deflection is measured at the tip of the beam. At 15 sec. and 30 sec., we push the system to show the performance of the suppression control against the unmodeled external disturbance.

mode and the update rate is around 400Hz with three motors. For accurate actuate, we calibrate the command-output force relation by using force sensor. Moreover, since the motors has high gear-ratio (for instance, the H54-200 model used for the θ_1 has 500:1 ratio), we compensates the motor (static) friction for better performance.

Next, for the linear stage, we use SMC-LEFS series which is ball-screw type linear actuator driven by 200W AC servo motor. The lead of the stage is chosen as 24mm which is the longest option of the model for the fast motion. The resolution of the stage encoder is 18 bit, i.e. 262,144 p/rev. We also calibrate by using force sensor to find the relation between the analog input and the output linear force. The update rate of the stage is around 1KHz.

Aluminium bars are used for the flexible beam. The length l_b is 0.907m, thickness is 0.012m, and the width is 0.05m. For the calculation of the natural frequencies described in Sec. 4.1.3. We use the encoders to measure the motions of the manipulator and stage system. And Optitrack, which is a motion capture system, is applied to measure the beam deflections.

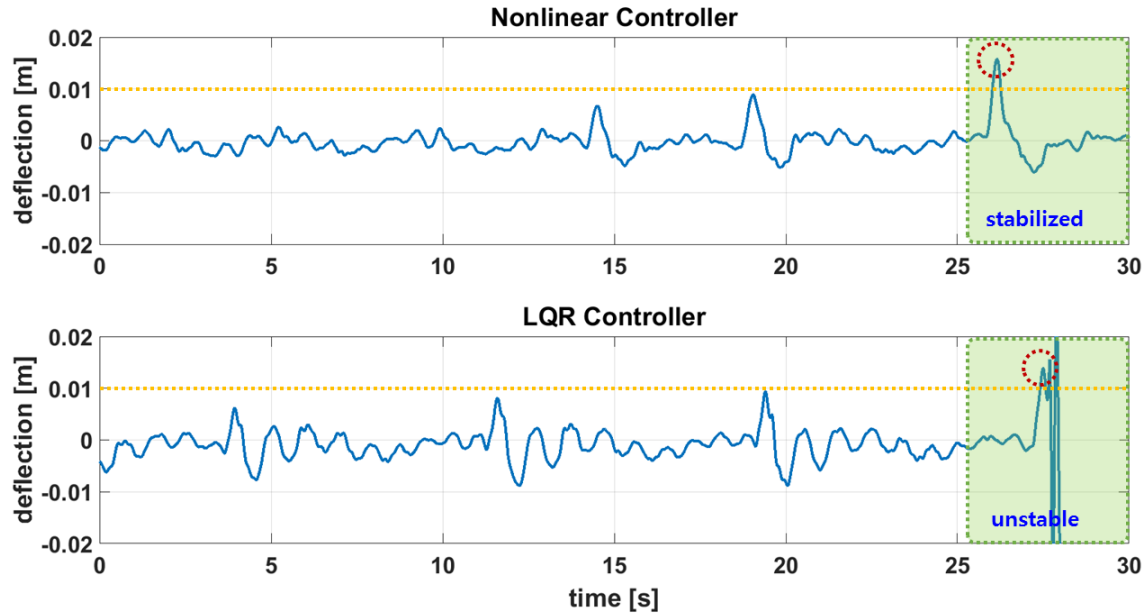


Figure 4-8: Performance comparison between the LQR controller in Sec. 4.2 and nonlinear control in Sec. 4.3 against external disturbance

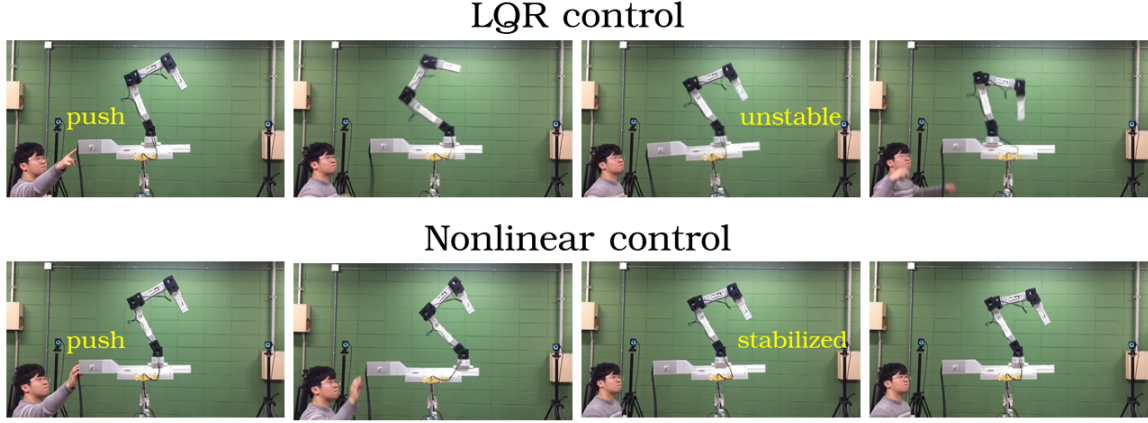


Figure 4-9: Snapshots of the comparison experiment: the upper row is the experiment with the LQR control where the large deflection due to the external disturbance cause the the system instability. On the other hands, in the second row, the deflection of the system with nonlinear control is still bounded.

4.4.2 Joint Tracking and Vibration Suppression Experiment

To verify the performance of the proposed controllers (4.26) and (4.28), we perform joint tracking control experiments with large enough initial joint error to see the performance of the vibration suppression control against dynamics coupling effect. At the beginning, the manipulator starts with large enough configuration error and then converges to the desired configuration as shown in (a) and (b) in Fig. 4-6. The convergence motion of the manipulator causes the system oscillation due to the dynamics effect. If we apply the vibration suppression control, then the system quickly becomes stable. Otherwise, it takes much longer time to be stabilized. Furthermore, around 15 sec. and 30 sec. we push the system to see the robustness and the performance against the unmodeled external disturbance. See (d) in Fig. 4-6.

Fig.6 clearly presents the performance of the vibration suppression control. If we do not apply the vibration suppression control, then the the vibration caused by both manipulator motion, i.e. dynamics effect, or the external force is attenuated by the structural damping which is not modeled in this thesis. Since the unmodeled structural damping is small, it takes long time (more than 30 sec.) to stabilize the system. On contrary to this, if we apply the vibration suppression control, the vibration is actively subdued in 5 sec.

4.4.3 Comparison Experiment between the LQR and the Non-linear Control

In this subsection, we conduct the experiment for the performance comparison between the LQR control in Sec. 4.2 and nonlinear control in Sec. 4.3. Since Both controllers can stabilize the vibration under the steady state motion of the manipulator, we push the system (force the large disturbance) to compare the margin of the stability of both controllers. For small deflection in which the linearization might be valid, LQR controller can stabilize the vibration. See. Fig. 4-8. However, if we excite the system with large external force, then the LQR controller cannot stabilize the system, and the system goes unstable. This might be the effect of the linearization so that if the system is far away from the equilibrium point, then the stability of the linear system is not valid any more. On the other hands, the nonlinear system can sustain the stability against the large deflection.

Chapter 5

Conclusion

5.1 Summary

Since, for complex robotic systems which has large DoFs or under-actuated property, the standard teleoperation framework is not sufficient for successful task in real-world environment, In this thesis, we develop decomposition-based semi-autonomous teleoperation framework for robotic systems which have distributed communication and under-actuation property. The proposed framework consists of three steps: 1) decomposition step, 2) control design of the slave robot, and 3) feedback interface design, which facilitates achievement of two different control objectives (i.e., follow the human command and the coordination/stabilization of the internal movement) of the slave robots simultaneously. We develop the framework for each case and perform the experiments to show the efficacy of the framework under harsh scenario or in real-world environment.

5.2 Future Works

For distributed WMRs, some possible future research topics include: 1) development of teleoperation strategy for platoon reconfiguration by using the leader WMR (e.g., backward escape from dead-end); 2) extension of the proposed framework to other types of distributed mobile robots (e.g., quadrotors [15, 54]); and 3) extension to

dynamic environments and robustification against various system failures.

For stage-manipulator on vertical flexible beam, future works include: 1) rigorous controllability analysis of the flexible part with only one stage input; and 2) extension to the larger DoFs system including advanced modeling approach such as finite element method or elastic kinematic chain for the flexible part to deal with large deformation.

Appendix A

Appendix

A.1 Internal Wrench Representation

Let us only consider rigid part systems. Then our generalized coordination would be $\bar{q}_r = [\theta_3; \theta_2; \theta_1; \theta_s; \theta_b; p_{ob}^y] = [q_r; \theta_b; p_{ob}^y] \in \mathfrak{R}^6$ where p_{ob}^y is the y -directional component of the vector p_{ob} . The Lagrangian of the system is defined by kinetic and potential energy as follows

$$L_r = T_r - V_r$$

Then, we obtain the dynamics of the rigid part system

$$\begin{aligned} \frac{d}{dt} \left(\frac{\partial L_r}{\partial \dot{\bar{q}}_r} \right) - \frac{\partial L_r}{\partial \bar{q}_r} &= M_r(\bar{q}_r) \ddot{\bar{q}}_r + C_r(\bar{q}_r, \dot{\bar{q}}_r) \dot{\bar{q}}_r + g_r(\bar{q}_r) \\ &= \tau_r + J_{rb}^T f_{\text{int}} + J_{re}^T f_{\text{ext}} \end{aligned}$$

where $\tau_r = [\tau_3; \tau_2; \tau_1; \tau_s; 0; 0]$ is control input, $f_{\text{ext}} = [f_{\text{ext}}^x; f_{\text{ext}}^y; f_{\text{ext}}^r] \in \mathfrak{R}^3$ is external force applied to the end-effector in $\{\mathcal{O}\}$, $f_{\text{int}} = [f_{\text{int}}^r; f_{\text{int}}^y] \in \mathfrak{R}^2$ is internal force between the boom and the rigid part system in $\{\mathcal{O}\}$, which is applied to the stage. Since we assume that the vertical deflection can be negligible, internal force along the vertical direction, i.e., f_{int}^x , does not appear in the above equation. In addition, Jacobian J_{rb}

and J_{re} are defined by

$$\begin{bmatrix} \dot{\theta}_b \\ \dot{p}_{ob}^y \end{bmatrix} \triangleq V_{ob} = J_{rb} \dot{q}_r \quad \text{and} \quad \begin{bmatrix} \dot{p}_{oe}^o \\ \dot{\theta}_{oe} \end{bmatrix} \triangleq V_{oe} = J_{re} \dot{q}_r$$

The dimensions of the Jacobian are both 2×7 . The Jacobian J_{rb} is given by

$$J_{rb} = \begin{bmatrix} 0 & 0 & 0 & 0 & 1 & 0 \\ 0 & 0 & 0 & 0 & 0 & 1 \end{bmatrix}$$

The control input of the rigid system is $\tau_r = [\tau_3; \tau_2; \tau_1; \tau_s; 0; 0] \in \mathfrak{R}^6$. To verify the control input, let us start with the virtual work of forces acting on a single rigid body. We define f_1, f_2, \dots, f_n as the forces acting on the points p_1, p_2, \dots, p_n in a rigid body. Then the velocity of the point p_i are given by

$$v_i = \omega_o \times (p_i - p_o) + v_o \tag{A.1}$$

where p_o is a reference point in the rigid body and v_o is the time derivative of p_o , i.e. $d/dt(p_o)$. ω_o is the angular velocity of the body.

The virtual work is computed from

$$\begin{aligned} \delta W &= \sum_{i=1}^n f_i^T \delta p_i = \sum_{i=1}^n f_i^T \left(\sum_{j=1}^m \frac{\partial p_i}{\partial q_j} \delta q_j \right) = \sum_{i=1}^n f_i^T \left(\sum_{j=1}^m \frac{\partial v_i}{\partial \dot{q}_j} \delta q_j \right) \\ &= \left(\sum_{i=1}^n f_i^T \frac{\partial v_i}{\partial \dot{q}_1} \right) \delta q_1 + \dots + \left(\sum_{i=1}^n f_i^T \frac{\partial v_i}{\partial \dot{q}_m} \right) \delta q_m \end{aligned}$$

To simplify the equation, consider only the first term with eq. (A.1) (i.e., consider

the rigid body can be specified by a single generalized coordinate q_1)

$$\begin{aligned}
\left(\sum_{i=1}^n f_i^T \frac{\partial v_i}{\partial \dot{q}_1} \right) \delta q_1 &= \left(\sum_{i=1}^n f_i^T \frac{\partial (\omega_o \times (p_i - p_o) + v_o)}{\partial \dot{q}_1} \right) \delta q_1 \\
&= \left(\sum_{i=1}^n f_i^T \frac{\partial v_o}{\partial \dot{q}_1} + \sum_{i=1}^n \underbrace{((p_i - p_o) \times f_i)^T}_{:=m_i^T} \frac{\partial \omega_o}{\partial \dot{q}_1} \right) \delta q_1 \\
&= \left(\sum_{i=1}^n f_i^T \frac{\partial v_o}{\partial \dot{q}_1} + \sum_{i=1}^n m_i^T \frac{\partial \omega_o}{\partial \dot{q}_1} \right) \delta q_1 \triangleq Q_1 \delta q_1
\end{aligned}$$

Next, let us consider a mechanical system which is constructed from n rigid bodies and let the resultant applied forces and torques F_i and T_i . Notice that these applied forces do not include the reaction forces where the bodies are connected. If the mechanical system is defined by m generalized coordinates, i.e. m -DoF, then the virtual work is given by

$$\delta W = \sum_{j=1}^m Q_j \delta q_j = \sum_{j=1}^m \left(\sum_{i=1}^n F_i^T \frac{\partial v_i}{\partial \dot{q}_j} + \sum_{i=1}^n M_i^T \frac{\partial \omega_i}{\partial \dot{q}_j} \right) \delta q_j$$

In our rigid system, $n = 5$ and $m = 6$ because the rigid system consists of the floating base, the linear stage, and the three links. Furthermore, as mentioned before, the generalized coordinate of the rigid body is 6 DoF. Recall $\bar{q}_r = [\theta_3; \theta_2; \theta_1; \theta_s; \theta_b; p_{ob}^y]$. Each resultant force-torque pair ($F_i \in \mathfrak{R}^2, M_i \in \mathfrak{R}$) can be expressed by

$$\begin{aligned}
[F_b, M_b] &= [(f_{\text{int}}^x + \tau_s \sin \theta_b, f_{\text{int}}^y - \tau_s \cos \theta_b), f_{\text{int}}^r - l_{bs} \tau_s], \\
[F_s, M_s] &= [(-\tau_s \sin \theta_b, \tau_s \cos \theta_b), -\tau_1], \\
[F_1, M_1] &= [(0, 0), \tau_1 - \tau_2], \\
[F_2, M_2] &= [(0, 0), \tau_2 - \tau_3], \\
[F_3, M_3] &= [(0, 0), \tau_3]
\end{aligned}$$

From the definition of the generalized force, we can calculate

$$\begin{aligned}
Q_1 &= M_3 \frac{\partial \omega_{o3}}{\partial \dot{\theta}_3} = \tau_3 \\
Q_2 &= M_2 \frac{\partial \omega_{o2}}{\partial \dot{\theta}_2} + M_3 \frac{\partial \omega_{o3}}{\partial \dot{\theta}_2} = (\tau_2 - \tau_3) + \tau_3 = \tau_2 \\
Q_3 &= M_1 \frac{\partial \omega_{o1}}{\partial \dot{\theta}_1} + M_2 \frac{\partial \omega_{o2}}{\partial \dot{\theta}_1} + M_3 \frac{\partial \omega_{o3}}{\partial \dot{\theta}_1} = \tau_1 \\
Q_s &= F_s^T \frac{\partial \dot{p}_{os}}{\partial \dot{\theta}_s} = F_s^T [-\sin \theta_b; \cos \theta_b] = \tau_s \\
Q_{\theta_b} &= \tau_3 + (\tau_2 - \tau_3) + (\tau_1 - \tau_2) - \tau_1 + f_{\text{int}}^r + l_{bs}\tau_s - l_{bs}\tau_s = f_{\text{int}}^r \\
Q_y &= f_{\text{int}}^y - \tau_s \cos \theta_b + \tau_s \cos \theta_b = f_{\text{int}}^y
\end{aligned}$$

The dynamics of the rigid part can be expressed

$$\begin{bmatrix} M_m & M_{mt} \\ M_{tm} & M_t \end{bmatrix} \begin{bmatrix} \ddot{q}_m \\ \ddot{q}_t \end{bmatrix} + \begin{bmatrix} C_m & C_{mt} \\ C_{tm} & C_t \end{bmatrix} \begin{bmatrix} \dot{q}_m \\ \dot{q}_t \end{bmatrix} + \begin{bmatrix} g_m \\ g_t \end{bmatrix} = \begin{bmatrix} \tau_m \\ \tau_t \end{bmatrix} + J_{rb} f_{\text{int}} \quad (\text{A.2})$$

where $q_m = [\theta_3; \theta_2; \theta_1] \in \mathfrak{R}^3$, $q_t = [\theta_s; \theta_b; p_{ob}^y] \in \mathfrak{R}^3$, $\tau_m = [\tau_3; \tau_2; \tau_1]$, and $\tau_t = [\tau_s; 0; 0]$.

Bibliography

- [1] Peter F Hokayem and Mark W Spong. Bilateral teleoperation: An historical survey. *Automatica*, 42(12):2035–2057, 2006.
- [2] Günter Niemeyer, Carsten Preusche, and Gerd Hirzinger. Telerobotics. In *Springer handbook of robotics*, pages 741–757. Springer, 2008.
- [3] R. Anderson and M. W. Spong. Bilateral control of teleoperators with time delay. *IEEE Transactions on Automatic Control*, 34(5):494–501, 1989.
- [4] D. A. Lawrence. Stability and transparency in bilateral teleoperation. *IEEE Transactions on Robotics and Automation*, 9(5):624–637, 1993.
- [5] Ryu Jee-Hwan, Kwon Dong-Soo, and B. Hannaford. Stable teleoperation with time-domain passivity control. *IEEE Transactions on Robotics and Automation*, 20(2):365–373, 2004.
- [6] Dongjun Lee and Perry Y Li. Passive bilateral control and tool dynamics rendering for nonlinear mechanical teleoperators. *IEEE Transactions on Robotics*, 21(5):936–951, 2005.
- [7] Lee Dongjun and M. W. Spong. Passive bilateral teleoperation with constant time delay. *IEEE Transactions on Robotics*, 22(2):269–281, 2006.
- [8] Nikhil Chopra, Mark W Spong, and Rogelio Lozano. Synchronization of bilateral teleoperators with time delay. *Automatica*, 44(8):2142–2148, 2008.
- [9] Emmanuel Nuno, Romeo Ortega, Nikita Barabanov, and Luis Basañez. A globally stable pd controller for bilateral teleoperators. *IEEE Transactions on Robotics*, 24(3):753–758, 2008.
- [10] D. J. Lee and K. Huang. Passive-set-position-modulation framework for interactive robotic systems. *IEEE Transactions on Robotics*, 26(2):354–369, 2010.
- [11] Dongjun Lee. Passive Decomposition and Control of Nonholonomic Mechanical Systems. *IEEE Transactions on Robotics*, 26(6):978–992, December 2010.
- [12] DJ Lee. Semi-autonomous teleoperation of multiple wheeled mobile robots over the internet. In *Proc. ASME Dynamic Systems & Control Conference*, pages 147–154, 2008.

- [13] Antonio Franchi, Cristian Secchi, Markus Ryll, Heinrich H Bulthoff, and Paolo Robuffo Giordano. Shared control: Balancing autonomy and human assistance with a group of quadrotor uavs. *IEEE Robotics & Automation Magazine*, 19(3):57–68, 2012.
- [14] Antonio Franchi, Cristian Secchi, Hyoung Il Son, Heinrich H Bulthoff, and Paolo Robuffo Giordano. Bilateral teleoperation of groups of mobile robots with time-varying topology. *IEEE Transactions on Robotics*, 28(5):1019–1033, 2012.
- [15] Dongjun Lee, Antonio Franchi, Hyoung Il Son, ChangSu Ha, Heinrich H Bülthoff, and Paolo Robuffo Giordano. Semi-autonomous haptic teleoperation control architecture of multiple unmanned aerial vehicles. *IEEE/ASME Transactions on Mechatronics*, 18(4):1334–1345, 2013.
- [16] Susumu Tachi, Kazuo Tanie, Kiyoshi Komoriya, and Makoto Kaneko. Tele-existence (i): Design and evaluation of a visual display with sensation of presence. In *Theory and Practice of Robots and Manipulators*, pages 245–254. 1985.
- [17] Charith Lasantha Fernando, Masahiro Furukawa, Tadatoshi Kurogi, Sho Kamuro, Katsunari Sato, Kouta Minamizawa, and Susumu Tachi. Design of TELE-SAR V for transferring bodily consciousness in telexistence. In *Proc. IEEE/RSJ International Conference on Intelligent Robots and Systems*, pages 5112–5118, 2012.
- [18] Martin Buss, Angelika Peer, Thomas Schauß, Nikolay Stefanov, Ulrich Unterhinninghofen, Stephan Behrendt, Jan Leupold, M Durkovic, and Michel Sarkis. Development of a multi-modal multi-user telepresence and teleaction system. *The International Journal of Robotics Research*, 29(10):1298–1316, 2010.
- [19] T. Hulin, K. Hertkorn, P. Kremer, S. Schatzle, Jordi Artigas, M. Sagardia, F. Zacharias, and C. Preusche. The dlr bimanual haptic device with optimized workspace. In *Proc. IEEE International Conference on Robotics and Automation*, pages 3441–3442, 2011.
- [20] Jaydev P Desai, James P Ostrowski, and Vijay Kumar. Modeling and control of formations of nonholonomic mobile robots. *IEEE Transactions on Robotics and Automation*, 17(6):905–908, 2001.
- [21] Aveek K Das, Rafael Fierro, Vijay Kumar, James P Ostrowski, John Spletzer, and Camillo J Taylor. A vision-based formation control framework. *IEEE Trans. on Robotics and Automation*, 18(5):813–825, 2002.
- [22] Joshua A Marshall, Terence Fung, Mireille E Broucke, Gabriele MT D’Eleuterio, and Bruce A Francis. Experiments in multirobot coordination. *Robotics and Autonomous Systems*, 54(3):265–275, 2006.
- [23] Gian Luca Mariottini, Fabio Morbidi, Domenico Prattichizzo, Nicholas Vander Valk, Nathan Michael, George Pappas, and Kostas Daniilidis. Vision-based

- localization for leader–follower formation control. *IEEE Trans. on Robotics*, 25(6):1431–1438, 2009.
- [24] Dongjun Lee and Mark W Spong. Bilateral teleoperation of multiple cooperative robots over delayed communication networks: Theory. In *Proc. IEEE International Conference on Robotics and Automation*, pages 360–365. IEEE, 2005.
 - [25] Erick J Rodriguez-Seda, James J Troy, Charles A Erignac, Paul Murray, Dušan M Stipanovic, and Mark W Spong. Bilateral teleoperation of multiple mobile agents: Coordinated motion and collision avoidance. *IEEE Transactions on Control Systems Technology*, 18(4):984–992, 2010.
 - [26] Won S Kim and Antal K Bejczy. Demonstration of a high-fidelity predictive/pre-view display technique for telerobotic servicing in space. *IEEE Transactions on Robotics and Automation*, 9(5):698–702, 1993.
 - [27] Nak Young Chong, Shun’ichi Kawabata, Kohtaro Ohba, Tetsuo Kotoku, Kiyoshi Komoriya, Kunikatsu Takase, and Kazuo Tanie. Multioperator teleoperation of multirobot systems with time delay: part i—aids for collision-free control. *Presence*, 11(3):277–291, 2002.
 - [28] Probal Mitra and Günter Niemeyer. Model-mediated telemanipulation. *The International Journal of Robotics Research*, 27(2):253–262, 2008.
 - [29] Alonzo Kelly, Nicholas Chan, Herman Herman, Daniel Huber, Robert Meyers, Pete Rander, Randy Warner, Jason Zigar, and Erin Capstick. Real-time photo-realistic virtualized reality interface for remote mobile robot control. *The International Journal of Robotics Research*, 30(3):384–404, 2011.
 - [30] Dongjun Lee and Perry Y Li. Passive decomposition approach to formation and maneuver control of multiple rigid bodies. *Journal of Dynamic Systems, Measurement, and Control*, 129(5):662–677, 2007.
 - [31] Dongjun Lee. Distributed backstepping control of multiple thrust-propelled vehicles on a balanced graph. *Automatica*, 48(11):2971–2977, 2012.
 - [32] I. Sharf. Active damping of a large flexible manipulator with a short-reach robot. In *Proc. American Control Conference*, volume 5, pages 3329–3333, June 1995.
 - [33] D. W. Cannon, D. P. Magee, W. J. Book, and J. Y. Lew. Experimental study on micro/macro manipulator vibration control. In *Proc. IEEE International Conference on Robotics and Automation*, volume 3, pages 2549–2554 vol.3, April 1996.
 - [34] J. Y. Lew. Contact control of flexible micro/macro-manipulators. In *Proc. IEEE International Conference on Robotics and Automation*, volume 4, pages 2850–2855 vol.4, April 1997.

- [35] J. Y. Lew and S. M. Moon. A simple active damping control for compliant base manipulators. *IEEE/ASME Trans. on Mechatronics*, 6(3):305–310, September 2001.
- [36] J. Lin, Z. Z. Huang, and P. H. Huang. An active damping control of robot manipulators with oscillatory bases by singular perturbation approach. *Journal of Sound and Vibration*, 304(1–2):345–360, July 2007.
- [37] De Z Li and Wilson Wang. An intelligent sliding mode controller for vibration suppression in flexible structures. *Journal of Vibration and Control*, 17(14):2187–2198, December 2011.
- [38] D. N. Nenchev, K. Yoshida, P. Vichitkulsawat, and M. Uchiyama. Reaction null-space control of flexible structure mounted manipulator systems. *IEEE Trans. on Robotics and Automation*, 15(6):1011–1023, December 1999.
- [39] D. Lee and P. Y. Li. Passive Decomposition of Mechanical Systems With Coordination Requirement. *IEEE Transactions on Automatic Control*, 58(1):230–235, January 2013.
- [40] Dongjun Lee and Kent Yee Lui. Passive configuration decomposition and passivity-based control of nonholonomic mechanical systems. *IEEE Transactions on Robotics*, 33(2):281–297, 2017.
- [41] Richard M Murray, Zexiang Li, S Shankar Sastry, and S Shankara Sastry. *A mathematical introduction to robotic manipulation*. CRC press, 1994.
- [42] Kent Yee Lui, Hyunjun Cho, ChangSu Ha, and Dongjun Lee. First-person view semi-autonomous teleoperation of cooperative wheeled mobile robots with visuo-haptic feedback. *The International Journal of Robotics Research*, 36(5–7):305–310, 2017.
- [43] Wei Ren and Randal W Beard. *Distributed consensus in multi-vehicle cooperative control*. Springer, 2008.
- [44] Dongjun Lee. Robust consensus of linear systems on directed graph with non-uniform delay. *IET Control Theory & Applications*, 10(18):2574–2579, 2016.
- [45] Giorgio Grisetti, Cyrill Stachniss, and Wolfram Burgard. Improving grid-based slam with rao-blackwellized particle filters by adaptive proposals and selective resampling. In *Proc. IEEE International Conference on Robotics and Automation*, pages 2432–2437. IEEE, 2005.
- [46] Giorgio Grisetti, Cyrill Stachniss, and Wolfram Burgard. Improved techniques for grid mapping with rao-blackwellized particle filters. *IEEE transactions on Robotics*, 23(1):34–46, 2007.

- [47] Joel A Hesch, Dimitrios G Kottas, Sean L Bowman, and Stergios I Roumeliotis. Camera-imu-based localization: Observability analysis and consistency improvement. *The International Journal of Robotics Research*, 33(1):182–201, 2014.
- [48] Yongseok Lee, Jaemin Yoon, Hyunsoo Yang, Changu Kim, and Dongjun Lee. Camera-gps-imu sensor fusion for autonomous flying. In *International Conference on Ubiquitous and Future Networks*, pages 85–88. IEEE, 2016.
- [49] Edwin Olson. Apriltag: A robust and flexible visual fiducial system. In *Proc. IEEE International Conference on Robotics and Automation*, pages 3400–3407. IEEE, 2011.
- [50] Leonard Meirovitch. *Fundamentals of vibrations*. Waveland Press, 2010.
- [51] A. De Luca and B. Siciliano. Closed-form dynamic model of planar multilink lightweight robots. *IEEE Trans. on Systems, Man and Cybernetics*, 21(4):826–839.
- [52] M. Abu-Hilal. Forced vibration of euler–bernoulli beams by means of dynamic green functions. 267(2):191–207.
- [53] Hassan K Khalil. Nonlinear systems. *Prentice-Hall, New Jersey*, 2(5):5–1, 1996.
- [54] ChangSu Ha, Zhiyuan Zuo, Francis B Choi, and Dongjun Lee. Passivity-based adaptive backstepping control of quadrotor-type uavs. *Robotics and Autonomous Systems*, 62(9):1305–1315, 2014.

요지

본 논문에서는 분산형 통신조건 또는 구동부족 특성을 가진 로봇 시스템을 위한 분할기법 기반의 반자율 원격제어 프레임워크를 개발한다. 제안된 프레임워크는 다음과 같은 3단계로 구분된다: 1) 사용자의 명령을 정의하고 이에 대해 기하적으로 수직인 공간 (즉, 내부움직임)으로 구분하는 분할단계; 2) 분할된 각 공간에서 명령 추종 및 내부움직임을 정합 혹은 안정화시키는 각각의 제어기를 설계하는 제어기 설계 단계; 3) 마지막으로 사용자에게 작업 및 로봇시스템의 특성을 고려하여 다중 감각 피드백을 제공해주기 위한 인터페이스 디자인 단계이다. 다양한 종류의 로봇시스템 중 본 학위논문에서는 분산통신을 따르는 다중 논홀로노믹 모바일로봇 시스템과 유연한 빔 위에 장착된 매니퓰레이터-스테이지 시스템을 고려하여 상기 프레임워크를 적용한다. 또한 각 시스템에 대해서 실험 및 사용자 테스트를 통하여 제안된 프레임워크의 성능을 검증한다.

Keywords: Semi-autonomous teleoperation, distributed systems, underactuated systems, decomposition-based control